

# **Improving the Gopinath-style Flux Observer for a Deadbeat Direct Torque and Flux Control Drive**

By

Gerardo A. Pantoja



Submitted to the Department of Electrical Engineering, Electronics, Computers and Systems

In partial fulfillment of the requirements for the degree of  
Master in Electrical Energy Conversion and Power Systems  
at the

**UNIVERSIDAD DE OVIEDO**

July 2020

© Universidad de Oviedo 2020. All rights reserved.

Author:.....

Gerardo Andrés Pantoja R.

Certified by: .....

Michael Saur

Dr. -Ing

Thesis Supervisor

Certified by: .....

Pablo García Fernandez

Associate Professor

Thesis Supervisor



# **Improving the Gopinath-style Flux Observer for a Deadbeat Direct Torque and Flux Control Drive**

By  
Gerardo A. Pantoja

Submitted to the Department of Electrical Engineering, Electronics, Computers and Systems

On July 23, 2020, in partial fulfillment of the requirements for the degree of Master of Science in Electrical Energy Conversion and Power Systems

## **Abstract**

The focus of this thesis is to study how to implement a high accuracy Gopinath-Style flux observer for the IPMSM of a DBDTFC drive for traction applications at Audi AG.

The current implementation had a steady state error of and was known to be suffering of model transition distortion between the CM and the VM. Therefore, resulting in an undesired SS overshooting the torque estimation. The SOA average error is of 4.2%.

This thesis proposes improvements for the model transition by means of the implementation of a Frequency Response Correction factor for the Observer. A more complex machine model for the IPMSM including Iron Losses. For which the Iron Loss resistances for no load tests as well as for a full torque speed plane were mapped. Moreover, the effects are evaluated via a steady state model of the machine. And finally, a decoupling through a new magnetics model is proposed and tested.

Open loop experimental tests show that the implementation of the FRC observer as well as the introduction of an Iron Losses Model for the current, enhance the overall performance of the Flux-Observer. The asymmetry in the flux observer estimation between motoring and generating conditions is reduced. And a closer match for the torque estimation is produced with a maximum error of around 1.3% at the maximum speed. The new average estimation error is of 1.9%

Thesis Supervisor: Michael Saur  
Title: Dr. -Ing at Audi AG

Thesis Supervisor: Pablo García Fernández  
Title: Associate Professor



## Acknowledgements

First, I just want express that I am thankful for the opportunity I have been given. Many people never have the chance to work in a topic of their interest. I had the chance to work in a fascinating topic, and most importantly along the way it that made me happy.

I am greatly thankful to Audi AG. For the chance of developing the Master thesis with them. I personally believe that investing time in helping with the education of the future workforce can enhance the conditions and productivity of the European people. By doing so they provide valuable experience to young minds.

Along the development of this work, long struggles against different technical issues were sustained. My mentors Ing. Hadi EL Khatib and Dr.-Ing. Michael Saur deserve a big thank you four their patience and support provided during this process.

I also want to use the opportunity to thank all the students of the EECPS and STEPS master's degree programs. They kindly supported me and always proposed educated discussions that lead to a great learning.

Finally, I want to thank my family who supported me through the entire process of my studies. Their support and comfort that allowed me to keep on fighting trough this hard process I stated two years ago at U. Oviedo.

# Table of Contents

Abstract.....	3
Acknowledgements.....	5
List of Figures.....	9
List of Tables.....	16
Acronyms, Abbreviations and Symbols .....	17
Chapter One.....	18
1.    Introduction .....	18
1.1    Background and Motivation.....	18
1.2    Objectives.....	18
1.3    Thesis Structure.....	18
Chapter Two .....	20
2    Literature Review.....	20
2.1    The Interior Permanent Magnet Synchronous Machine IPMSM.....	20
2.2    IPMSM Control Methods.....	24
2.3    Dead Beat Direct Torque and Flux Control (DB-DTFC) for IPMSM .....	26
2.3.1    DB-DTFC algorithm .....	26
2.3.2    DB_DTFC graphical Interpretation.....	29
2.3.3    DB_DTFC System Block Diagram:.....	30
2.4    The Luenberger-style current observer. ....	31
2.5    Flux linkage estimation with a Gopinath Style flux observer .....	32
2.5.1    Flux observer controller tuning.....	34
2.5.2    Gopinath-style flux observer PI controller role.....	35
2.5.3    Angle for the reference frame transforms. ....	36
2.6    Latest advancements literature review: .....	37
2.6.1    Implementation Issues of DB_DTFC.....	38
2.6.2    Disturbance Input Decoupling with Luenberger current observer .....	39
2.6.3    Design of Flux Observer Robust to Parameter Variation of Interior Permanent Magnet Synchronous Motor .....	41
2.6.4    Torque Error Compensation Algorithm for IPMSM.....	42
2.6.5    Modified Integrator for the Voltage Model of the Flux observer .....	43
2.6.6    The center Point Correction method for the flux linkage Voltage Model.....	44

2.6.7	IDRIS AND YATIM “An improved stator flux linkage estimation” .....	46
2.6.8	The Observer Characteristic Function Method .....	47
2.7	Conclusions: .....	49
	Chapter Three .....	51
3	Implementing the Observer Characteristic Function Method for IPMSM Gopinath-Style Observer	51
3.1.1	Theoretical development for IPMSM observer:.....	51
3.1.2	Solution Implementation:.....	54
3.1.3	Simulation results and Models Benchmarking:.....	55
3.1.4	Parameter Sensitivity Analysis.....	60
3.1.5	Torque Step Response Benchmarking .....	67
3.1.6	Conclusions: .....	72
	Chapter Four .....	75
4	Iron Losses and their effect on the flux linkage estimator .....	75
4.1	Models for the Iron Losses, definitions and benchmark .....	75
4.1.1	Introduction .....	75
4.1.2	Iron Loss Modeling .....	76
4.2	Iron Loss model Implementation. ....	77
4.3	Effect of Iron Losses in the drive control system.....	81
4.3.1	Iron loss steady state model for IPMSM .....	81
4.3.2	Effects of Iron loss model for IPMSM in SS. ....	82
4.3.3	Increasing d-axis current effect with no q-axis current: .....	84
4.3.4	Positive v/s Negative q-axis current effect with no d-axis current:.....	85
4.3.5	Increasing q-axis current effect with no d-axis current: .....	86
	IPMSM Iron Losses Model Speed Ramp Test .....	86
4.3.6	Effect of Iron losses on the voltage vector .....	88
4.3.7	Zero torque production current compensation .....	92
4.4	Improving the Gopinath style observer to be resilient to iron losses. ....	93
4.4.1	Conclusions: .....	97
	Chapter Five .....	100
5	Open Loop Tests and Implementation .....	100
5.1	Observers implementation.....	100
5.2	Conclusions .....	107

Chapter Six .....	108
6     Conclusions and Outlook .....	108
4.1.     Conclusions .....	108
4.2.     Future Work .....	110
APPENDIX .....	116
Frequency Response Correction Factor Demonstration .....	116

# List of Figures

Figure 1 IPMSM basic rotor structure. Cross sectional view of the rotor. [3] .....	20
Figure 2 IPMSM Maximum torque per ampere. [6] At the left the torque vs rotor speed on the top and the current and voltages, at the right the maximum torque per ampere and maximum torque per flux trajectories are displayed. ....	23
Figure 3 CVC block diagram [4]. The block diagram of a typical CVC control system is displayed. ....	24
Figure 4 DTC control Block Diagram [7]. A DTC system with hysteresis control is described. The control variables are the speed and flux of the machine. ....	26
In the block diagram of Figure 5, the DTC system uses a flux and torque observer from where the flux and torque loops are closed. The speed control loop is cascaded over the torque loop.....	26
Figure 6 DB-DTFC Graphical Solution [8]. (Red) the torque equation line for the k+1 instant, (Black circle) the dqs flux linkage limits, (Black Hexagon) inverter voltage limit.....	30
Figure 7 Deadbeat Direct torque control typical application block diagram by [9]. (Yellow) DB-DTFC required blocks for the Control Law. Note the presence of a Full Order current and flux linkage observer.....	30
Figure 8 Event timing on DBDTFC control in one sampling period. [9]. The timing for each process signal is displayed on the left. It is important to note the in advance (k+1) instant input requirements for the system computation. ....	31
Figure 9 Discrete Luenberger-style Current Observer [2]. The observer is based on the IPMSM voltage equation. It seeks to predict the current in the next sampling instant (k+1). ....	31
Figure 10 Gopinath Style Flux Observer. [4]. At the left side the current model, after the stator reference frame transform the PI controller and then the voltage model. ....	33
Figure 11 Flux Linkage estimator Control Tuning Path [4]. The VM is operated so that $\lambda dqs$ path is the only output.....	34
We could define the tuning pad of the controller in a simplified way as in Figure 12. Considering for instance the transfer functions of this system, it is possible to see that a relationship between the fluxes can be established as: .....	35
Figure 13 Bode diagram of A and B. The equivalent poles of this system are located at 314 and 31 rad/s respectively. A line is placed at the controller tuning frequency. The transition between the voltage and current model dominance can be therefore explained trough the frequency response of the system.....	35
Figure 14 Stator Flux Linkage Observer Voltage Model signal types. [10]. Shows the observer topologies and the signal types for the different paths. (Red) Latch Type, (Green) Ramp type.....	36
Figure 15 Discrete Gopinath-style flux observer angle time instant adjustment. This angle adjustment is applied at the entrance of the reference frame transform in order to match the delay to the signal type.....	37
Figure 16 Block diagram of the DID implementation in the d axis flux linkage observer [11]. In the figure q-axis Luenberger current Observer in red, d-axis Gopinath-style Flux linkage observer in blue and DID forward term in green. ....	40
Figure 17 Discrete Gopinath-style flux observer Yoo and Soul modification. (Red) The path where the Flux Linkage Difference is applied. ....	42

Figure 18 Torque Error Compensation Control Scheme from [13] shows the introduction of a compensation factor in the current command; This correction seeks to enhance the torque equation accuracy under parameter deviation.....	43
Figure 19 Modified Integrator Voltage Model based Open loop Flux linkage Observer for IM. This solution avoids the integrator drift-problem by the implementation of a DC filter without phase distortion. ....	44
Figure 20 Center Point Correction Method by [16]. Presents a Modified Integrator Voltage Model based Open loop Flux linkage Observer for IM based on a LPF and a Frequency Response Correction. ....	45
Figure 21 Center Point Method Adaptive Filter Implementation by [16]. Presents a Modified Integrator Voltage Model based Open loop Flux linkage Observer for IM based on an adaptive LPF and a Frequency Response Correction. ....	46
Figure 22 Open Loop VM modification by Idris and Yatim [17]. Presents an additional path that cancels the Filter Distortion at SS. ....	47
Figure 23 Trajectory of the transition between the VM and CM in a Gopinath-style flux linkage estimator for induction machines [18] .....	48
Figure 24 Gopinath-style flux observer tuning path in Laplace domain with correction according to The Observer Characteristic Function Method by [18].....	49
Figure 25 Flux Linkage estimator Control Tuning Path [4]. The VM is operated so that $\lambda_{dqs}$ path is the only output.....	51
Figure 26 Gopinath-style flux observer tuning path in Laplace domain with correction according to The Observer Characteristic Function Method. (Red) Both correction Terms introduced in the observer.....	53
Figure 27 Simulink Implementation of A' and B' correction factors. In blue the angle correction for B' correction factor. (In darker gray) B' correction factor and (in light gray) the A' correction factor. ....	54
Figure 28 A' Correction Factor Subsystem. (Inputs) the frequency, and the controller gains that multiply the Flux linkage of the voltage model entering at (1).....	54
Figure 29 B' Correction Factor Subsystem. (Inputs) the frequency, and the controller gains that multiply the Flux linkage of the current model entering at (1). ....	55
Figure 30 Offset angle for B' correction factor. Shows the required Angle Offset for the CM flux linkage in order to calculate the correction factor.....	55
Figure 31 Simulation results of the Estimated Flux with the SOA and FRC Observers in CL implementation. The torque command is 450 Nm the MTPA Flux command is based on a LUT and the speed is increasing with time at a constant rate.....	56
Figure 32 Machine flux vs estimation Zoom into the constant torque region. (Blue) Machine SOA Flux, (Orange) Estimated flux with SOA Observer. (Green) Machine FRC Flux, (Purple) Estimated flux with FRC Observer.....	56
In Figure 33, the overshoot in the machine flux at the beginning is smaller in the FRC. Also, the flux production of the machine is better under the FRC observer. Least estimation error is therefore expected in this region for the FRC observer.....	56

Figure 34 Machine flux vs estimation Zoom into the model transition area. (Blue) Machine SOA Flux, (Orange) Estimated flux with SOA Observer. (Green) Machine FRC Flux, (Purple) Estimated flux with FRC Observer.....	57
Figure 35 Machine flux vs estimation Zoom Difference at current limits. (Blue) Machine SOA Flux, (Orange) Estimated flux with SOA Observer. (Green) Machine FRC Flux, (Purple) Estimated flux with FRC Observer. ....	57
Figure 36 Machine flux vs estimation Zoom at 6000 RPM. (Blue) Machine SOA Flux, (Orange) Estimated flux with SOA Observer. (Green) Machine FRC Flux, (Purple) Estimated flux with FRC Observer.....	58
Figure 37 Machine flux vs estimation Zoom at high speed range 15 000 RPM to 17 000 RPM. (Blue) Machine SOA Flux, (Orange) Estimated flux with SOA Observer. (Green) Machine FRC Flux, (Purple) Estimated flux with FRC Observer.....	58
Figure 38 Flux Magnitude Estimation Error. (Blue) absolute flux magnitude error form the SOA Observer. (Orange) absolute flux magnitude error form the FRC Observer.....	59
Figure 39 Absolute Flux Angle Estimation Error. (Blue) absolute flux angle error form the SOA Observer. (Orange) absolute flux angle error form the FRC Observer.....	59
Figure 40 Torque Estimation Error for SOA and FRC Observers. (Blue) absolute torque error form the SOA Observer. (Orange) absolute torque error form the FRC Observer.....	60
Figure 41 Flux Magnitude Deviation SOA and FRC observers under a 10% deviation of $L_d$ . (Blue) absolute flux magnitude error form the SOA Observer. (Orange) absolute flux magnitude error form the FRC Observer.....	61
Figure 42 Flux Angle Deviation SOA and FRC observers under a 10% deviation of $L_d$ . (Blue) absolute flux angle error form the SOA Observer. (Orange) absolute flux angle error form the FRC Observer.....	61
Figure 43 Torque Magnitude Deviation SOA and FRC observers under a 10% deviation of $L_d$ . (Blue) absolute torque error form the SOA Observer. (Orange) absolute torque error form the FRC Observer.....	61
Figure 44 Flux Magnitude Deviation SOA and FRC observers under a 10% deviation of $L_q$ . (Blue) absolute flux magnitude error form the SOA Observer. (Orange) absolute flux magnitude error form the FRC Observer.....	62
Figure 45 Flux Angle Deviation SOA and FRC observers under a 10% deviation of $L_q$ . (Blue) absolute flux angle error form the SOA Observer. (Orange) absolute flux angle error form the FRC Observer.....	63
Figure 46 Torque deviation SOA and FRC observers under a 10% deviation of $L_q$ . (Blue) absolute torque error form the SOA Observer. (Orange) absolute torque error form the FRC Observer. ....	63
Figure 47 Flux Magnitude Deviation SOA and FRC observers under a 10% deviation of $\lambda_{pm}$ . (Blue) absolute flux magnitude error form the SOA Observer. (Orange) absolute flux magnitude error form the FRC Observer.....	64
Figure 48 Flux Angle Deviation SOA and FRC observers under a 10% deviation of $\lambda_{pm}$ . (Blue) absolute flux angle error form the SOA Observer. (Orange) absolute flux angle error form the FRC Observer.....	64

Figure 49 Torque Magnitude Deviation SOA and FRC observers under a 10% deviation of $\lambda_{pm}$ . (Blue) absolute torque error form the SOA Observer. (Orange) absolute torque error form the FRC Observer.....	65
Figure 50 Flux Magnitude deviation SOA and FRC observers under a 10% deviation of $R_s$ . (Blue) absolute flux magnitude error form the SOA Observer. (Orange) absolute flux magnitude error form the FRC Observer.....	65
Figure 51 Flux Angle deviation SOA and FRC observers under a 10% deviation of $R_s$ . (Blue) absolute flux angle error form the SOA Observer. (Orange) absolute flux angle error form the FRC Observer.....	66
Figure 52 Torque Deviation SOA and FRC observers under a 10% deviation of $R_s$ . (Blue) absolute torque error form the SOA Observer. (Orange) absolute torque error form the FRC Observer.....	66
Figure 53 Machine States with SOA (left) and FRC (right) Flux linkage Observers under Torque Test at low speeds. (Top) torque command in yellow and machine torque in blue. (Top middle) $i_d$ in yellow, $i_q$ in blue and $i_{dq}$ in orange. (Bottom middle) $U_d$ in yellow, $U_q$ in blue and $U_{dq}$ in orange. (Bottom) flux command in yellow and estimated flux in blue.....	68
Figure 54 Flux magnitude deviation, torque step response at 2000 rpm. (Blue) absolute flux magnitude error form the SOA Observer. (Orange) absolute flux magnitude error form the FRC Observer.....	68
Figure 55 Flux angle deviation, torque step response at 2000 rpm. (Blue) absolute flux angle error form the SOA Observer. (Orange) absolute flux angle error form the FRC Observer.....	69
Figure 56 Torque deviation, torque step response at 2000 rpm. (Blue) absolute torque error form the SOA Observer. (Orange) absolute torque error form the FRC Observer.....	69
Figure 57 Reference tracking, torque step response at 2000 rpm. (Blue) Commanded Torque. (Orange) torque obtained by implementation of the SOA Observer. (Green) torque obtained by implementation of the FRC Observer.....	69
Figure 58 Torque step test simulation at 12000 RPM for FRC Machine Status are displayed. (Top) torque command in yellow and machine torque in blue. (Top middle) $i_d$ in yellow, $i_q$ in blue and $i_{dq}$ in orange. (Bottom middle) $U_d$ in yellow, $U_q$ in blue and $U_{dq}$ in orange. (Bottom) flux command in yellow and estimated flux in blue.....	71
Figure 59 Flux magnitude deviation, torque step response at 12000 rpm. (Blue) absolute flux magnitude error form the SOA Observer. (Orange) absolute flux magnitude error form the FRC Observer.....	71
Figure 60 Flux angle deviation, torque step response at 12000 rpm. (Blue) absolute flux angle error form the SOA Observer. (Orange) absolute flux angle error form the FRC Observer.....	71
Figure 61 Torque deviation, torque step response at 12000 rpm. (Blue) absolute torque error form the SOA Observer. (Orange) absolute torque error form the FRC Observer.....	72
Figure 62 SOA VS FRC Torque Step Response Reference tracking to 100, 150, and 50 N/m Benchmarking. (Blue) Commanded Torque. (Orange) torque obtained by implementation of the SOA Observer. (Green) torque obtained by implementation of the FRC Observer.....	72
Figure 63 shows the data analysis of the values obtained from simulation at $t = 0.7$ Sec. Where a torque step is applied. Both responses reduce the error quite significantly and are stable in Steady State.....	72

Figure 64 Collection of Iron Losses equivalent circuits proposed in the literature. (A) Parallel Iron loss resistance to magnetizing branch by [21], (B) First Harmonic circuit [22], (C) Variable asymmetrical iron loss resistances by [23], (D) Eddy Currents and Hysteresis Iron loss by [24], (E) Iron Loss Model Considering asymmetric iron loss resistances and cross saturation by [25], (F) Finite Elements Model by [26], (G) Series Resistance model.....	76
From the conclusions of the previous sections it a circuit like the one on Figure 65 (C), is chosen. If the KVL and KCL are used to describe the circuit, a set of equations that describe this system in the rotor reference frame is obtained as: .....	77
Figure 66 Simulink model of the IPMSM considering Iron Losses. In these system equations, (98) to (105) are represented as (1) to (8) respectively in Simulink blocks.....	78
Figure 67 Experimental Iron Loss Power for 100- and 200-mm machines. (Blue) Iron loss power from the no load tests for 100 mm machine. (Orange) Iron loss power from the no load tests for 200 mm machine.....	79
Figure 68 Iron Loss Resistance from Experimental NL losses for 100- and 200-mm machines. (Blue) Iron loss resistance from the no load tests for 100 mm machine. (Orange) Iron loss resistance from the no load tests for 200 mm machine.....	79
Figure 69 Iron Loss Resistance map from FEM iron loss power data for IPM 210 600V Machine. (Contours) Iron loss resistance in Ohms for the 200 mm Machine.....	80
Figure 70 Impact of Iron Losses in the machine with pure id current currents at high speed. (Left) Impact of the iron losses resistance in the magnetizing current. Deviation results are displayed in the figure. (Right) Impact of the iron losses resistance in the machine flux.....	82
Figure 71 3 Phasor Diagram of Positive v/s Negative d-axis current with no q-axis current for $id=+-100A$ $iq=0$ . (Left) Impact of the iron losses resistance in the magnetizing current. Deviation results are displayed in the figure. (Right) Impact of the iron losses resistance in the machine flux.....	83
Figure 72 Phasor Diagram of increasing d-axis current effect with no q-axis current. (Left) Impact of the iron losses resistance in the magnetizing current. (Right) Impact of the iron losses resistance in the machine flux.....	84
Figure 73 3 Phasor Diagram of Positive v/s Negative q-axis current with no d-axis current for $iq=+-100A$ $id =0$ (Left) Impact of the iron losses resistance in the magnetizing current. Deviation results are displayed in the figure. (Right) Impact of the iron losses resistance in the machine flux.....	85
Figure 74 Phasor Diagram of increasing q-axis current effect with no d-axis current. (Left) Impact of the iron losses resistance in the magnetizing current. Deviation results are displayed in the figure. (Right) Impact of the iron losses resistance in the machine flux.....	86
Figure 75 Angle deviation, Torque and flux production under a speed ramp with 100 [A] pure d axis current. (Top Left) Flux angle distortion for pure d axis current. Deviation results are displayed in the figure. (Top Right) Undesired torque production. (Bottom Left) $Idq$ current and magnetizing current. (Bottom Right) Impact of the iron losses resistance in the machine flux.....	87
Figure 76 $Vdqs$ Angle at zero $Idqs$ vs speed range for $id=0$ . (Blue) voltage vector angle obtained with $Idqs=0$ at different speeds.....	88
From Figure 77, the iron losses introduce an angle deviation in the voltage. In performance drives automatic angle tuning routines use such a measurement to align the system angle. An error is introduced in the algorithm by the iron losses.....	88

Figure 78 Voltage vector angle of the ideal Model of the IPMSM in SS. (All colors) voltage vector angle obtained with different Idqs inputs at different speeds.....	89
Figure 79 Voltage vector Angle Vs Speed using the SS model of the IPM Considering Iron Losses. (All colors) voltage vector angle obtained with different Idqs inputs at different speeds.....	90
Figure 80 Reduced Stator Resistance Voltage Vector angle vs speed in steady state without Iron Losses. (All colors) voltage vector angle obtained with different Idqs inputs at different speeds....	91
Figure 81 Reduced Stator Resistance Voltage Vector angle vs speed in steady state considering Iron Losses. (All colors) voltage vector angle obtained with different Idqs inputs at different speeds....	91
Figure 82 Results for Rfe=240-ohm machine parameters at 17 000 rpm. (Blue) Idqs angle for different magnitudes at 17000 rpm. (Orange) Idqs angle for different magnitudes at 10000 rpm. (Green) Idqs angle for different magnitudes at 2000 rpm. ....	92
Figure 83 Results for Rfe=[240,319,70] ohm machine parameters at 17 000 rpm. (Blue) Idqs angle for different magnitudes at 17000 rpm. (Orange) Idqs angle for different magnitudes at 10000 rpm. (Green) Idqs angle for different magnitudes at 2000 rpm. ....	93
Figure 84 Magnetizing current estimation scheme, transfers the information of id and iq from the machine measured quantities into the magnetizing components. The LUT implements the NL tests iron loss resistance for a 200mm Long Machine .....	93
Figure 85 Machine Flux v/s Estimation along the speed ramp for all 4 observers. ( Blue) machine flux, (Orange and green) Estimated flux with SOA and FRC observers respectively. (Purple and Magenta) Estimated flux with SOA and FRC with 1D Iron Losses LUT observers respectively....	94
Figure 86 Absolute Flux Magnitude estimation error. (Blue) flux magnitude estimation error with SOA obs. (Orange) flux magnitude estimation error with FRC obs. (Green) flux magnitude estimation error with SOA obs. with iron loss LUT. (Purple) flux magnitude estimation error with FRC obs. with iron loss LUT. ....	94
Figure 87 Flux Angle Estimation Error. (Blue) flux angle estimation error with SOA obs. (Orange) flux angle estimation error with FRC obs. (Green) flux angle estimation error with SOA obs. with iron loss LUT. (Purple) flux angle estimation error with FRC obs. with iron loss LUT. ....	95
Figure 88 Absolute Torque Estimation Error. (Blue) Torque estimation error with SOA obs. (Orange) Torque estimation error with FRC obs. (Green) Torque estimation error with SOA obs. with iron loss LUT. (Purple) Torque estimation error with FRC obs. with iron loss LUT. ....	95
Figure 89 Torque Estimation Error Based on the flux, Shows the abs(Torque-Torque Est.) where the torque estimation is calculated based only on the $\lambda_d$ and $\lambda_q$ quantities, without the current. (Blue) Torque estimation error with SOA obs. (Orange) Torque estimation error with FRC obs. (Green) Torque estimation error with SOA Obs. with iron loss LUT. (Purple) Torque estimation error with FRC Obs. with iron loss LUT. ....	95
Figure 90 Measured Speed and Torque for Long machine. (Top) Commanded Speed. (Bottom) Commanded Torque.....	100
Figure 91 Comparison between SOA and AUDI Observer. (Blue) Estimated torque with the Audi observer. (Dot orange) Estimated torque with the SOA observer. (Green) Measured torque with torque sensor. ....	100
Figure 92 Difference between Gopinath-Obs and CM-Obs. (Blue) Estimated torque with the Audi observer. (Dot orange) Estimated torque with the Audi observer CM-Obs. (Green) Measured torque with torque sensor. ....	101

Figure 93 Open Loop response to the speed/ torque profile from the FRC Observer. (Blue) Estimated torque with the FRC observer. (Orange) Measured torque with torque sensor.....	102
Figure 94 Torque Error Benchmarking for AUDI, SOA, FRC Observers. (Blue) Estimated torque error with the Audi observer. (Orange) Estimated torque error with the SOA observer. (Green) Estimated torque error with the FRC observer.....	102
Figure 95 Open Loop response to the speed/ torque profile from the AUDI/SOA Observer with Iron Loss LUT. (Blue) Estimated torque with the Audi observer with Iron losses 1D LUT. (Orange) Measured torque with torque sensor. ....	103
Figure 96 Open Loop response to the speed/ torque profile from the FRC Observer with Iron Loss LUT. (Blue) Estimated torque with the Audi observer with Iron losses 1D LUT. (Orange) Measured torque with torque sensor. ....	103
Figure 97 Open Loop Observers benchmarking considering Iron Losses 1D LUT. (Blue) Estimated torque error with the Audi observer. (Orange) Estimated torque error with the SOA observer. (Green) Estimated torque error with the FRC observer.....	104
Figure 98 Open Loop response to the speed/ torque profile from the AUDI/ SOA Observer with 2D Iron Loss LUT. (Blue) Estimated torque with the Audi observer with Iron losses 2D LUT. (Orange) Measured torque with torque sensor. ....	104
Figure 99 Open Loop response to the speed/ torque profile from the FRC with 2D Iron Loss LUT. (Blue) Estimated torque with the FRC observer with Iron losses 2D LUT. (Orange) Measured torque with torque sensor. ....	104
Figure 100 Open Loop response to the speed/ torque profile from the AUDI/SOA Observer with / Without Iron Loss LUT. (Blue) Estimated torque with original Audi obs. (Orange). Estimated torque with the Audi observer with Iron losses 1D LUT. (Green) Estimated torque with the Audi observer with Iron losses 2D LUT. (Purple) Measured torque with torque sensor. ....	105
Figure 101 Average Error Per speed / Torque sector. In this figure the different models are compared respect to the sensed torque for each operation point of the OL test profile. The SOA observer labeled AUDI is shown in dashed lines. ....	106
Figure 102 Average Error Per speed sector. In this figure the different models are compared respect to the sensed torque for each speed operation point of the OL test profile. The SOA observer labeled AUDI is shown in dashed lines. ....	106

## List of Tables

Table 1 DTC Vectors Switching Table [7] .....	25
Table 2 Parameter Sensitivity Simulation Results Summary. At the left side the SOA observer's response and at the right side the FRC Observer response. In each group the flux magnitude error, angle deviation and torque error under the variation of the par .....	67
Table 3 Results of Positive v/s Negative d-axis current with no q-axis current for id=+100A .....	84
Table 4 Results of increasing d-axis current effect with no q-axis current .....	85
Table 5 Results of Positive v/s Negative d-axis current with no d-axis current for iq=+100A .....	85
Table 6 Results of increasing d-axis current effect with no q-axis current .....	86
Table 7 Speed Ramp output variables.....	88
Table 8 Average differences between CM and VM. Table values are presented in [%] respect to the Current Model and the angle difference is displayed on the right after the “ ” in degrees.....	101
Table 9 Average torque estimation error with AUDI with 2D LUT and FRC with 2D LUT. Table values are presented in [%] respect to the commanded value. The AUDI observer results are displayed on the left and the FRC results are displayed on the right .....	105
Table 10 Average torque estimation error Considering Iron Losses Model in Torque Equation AUDI with 2D LUT and FRC with 2D LUT. Table values are presented in [%] respect to the commanded value. The AUDI observer results are displayed on the left and the FRC results are displayed on the right. ....	105

## Acronyms, Abbreviations and Symbols

Symbol	Description
$V_{ds}^r$	d-Axis Stator Voltage in rotor reference frame
$V_{qs}^r$	q-Axis Stator Voltage in rotor reference frame
$I_{ds}^r$	d-Axis Stator Current in rotor reference frame
$I_{qs}^r$	q-Axis Stator Current in rotor reference frame
$\lambda_{ds}^r$	d-Axis Stator Flux Linkage in rotor reference frame
$\lambda_{qs}^r$	q-Axis Stator Flux Linkage in rotor reference frame
$w_e, W_r, W_s$	Electrical Frequency , Electrical frequency at the Rotor or Stator
$R_s$	Stator Resistance
$\lambda_{pm}, Y_{pm}$	Permanent Magnet Flux
$L_d, L_q$	d-axis and q-axis Stator Inductances
$T_{em}, T_e$	Electromechanical Torque
$P$	Machine Poles
$\delta$	Saliency Ratio
$I_{sc}$	Short Circuit Current
$V_{smax}$	Voltage Limit
$I_{smax}$	Current Limit
$\lambda_{dqs}^s$	Estimated Flux Linkage in the stator reference frame
$\lambda_{dqs}^s(\text{CM})$	Estimated Flux Linkage from the current model
$\lambda_{dqs}^s(\text{VM})$	Estimated Flux Linkage from the voltage model
$i_{md}, i_{mq}$	d-axis and q-axis Stator Magnetizing Currents
$i_{fed}, i_{feg}$	d-axis and q-axis Machine Iron Currents
$R_{fe}$	Iron Loss Resistance
IPMSM	Inner Permanent Magnet Synchronous Machine
MTPA	Maximum Torque per Ampere
CVC	Current Vector Control
DTC	Direct Torque Control
DB-DTFC	DeadBeat Direct Torque and Field Control
$(K + 1)$	Unit at the next sampling instant
$(K)$	Unit at the current sampling instant
Obs.	Observer
CM	Current Model
VM	Voltage Model
A	Flux Linkage VM to estimated flux linkage transfer function
B	Flux Linkage CM to estimated flux linkage transfer function
SOA	State of the Art Flux Linkage Observer
FRC	Frequency Response Corrected Flux Linkage Observer
LUT	Look Up Table
OL	Open Loop

# Chapter One

## 1. Introduction

### 1.1 Background and Motivation

Deadbeat Direct Torque and Field Control (DB DTFC) uses flux linkage estimation to control the torque of a drive without the need of a LUT. An increased interest in IPMSM as traction machines has been occurring in the last decade due to its superior reluctance and magnet torque capabilities. Car manufacturers like Audi AG are implementing nowadays DB-DTFC for IPMSM drives.

As explained by [1], a DB-DTFC drive requires the torque to be estimated in advance at the instant (K+1). A typical implementation utilizes a full order flux linkage and current observer.

This thesis addresses the problem of improving a full order Gopinath-style flux linkage estimator for a DB-DTFC IPMSM drive that has a smooth transition between current and voltage models and is resilient to distortions caused by the iron losses

In [2], the robustness of DB\_DTFC is compared to traditional Current Vector Control (CVC) for IPMSM and shows that a slight enhancement in the Flux Linkage and Current Observers implies a big advantage in the control of the DB-DTFC drive.

### 1.2 Objectives

The central theme of this thesis is the enhancement of the Gopinath-style flux linkage observer for DB\_DTFC applications. The fundamental objectives for the process are:

- Analyze the state of the art of the DB\_DTFC Gopinath-style flux linkage estimator.
- Simulate the behavior of the flux linkage observer in a DB\_DTFC drive.
- Implement a correction factor for the model transition of the flux linkage observer and benchmark it with simulation and experimental data.
- Simulate the effect of the iron losses in the flux linkage observer based on experimental data.
- Simulate and implement a correction factor for the current model of the Flux Linkage observer considering the Iron Losses distortions.

### 1.3 Thesis Structure

Towards the previously mentioned objectives, the thesis work was developed, and the structure is organized as follows:

#### **Chapter1: Introduction**

This present chapter introduces the motivation for the work carried out in this thesis as well as the main objectives for this thesis.

## **Chapter 2: Literature Review**

This chapter reviews the DB-DTFC implementation issues as well as the current State of the Art Current Observer and Flux Linkage Observer. It provides the insight on how it is currently being implemented. Later, this chapter, the latest literature techniques and advancements are reviewed. Several authors' ideas are exposed and explained. The key improvement areas are detected for further development.

## **Chapter 3: Implementing the Observer Characteristic Function Method for IPMSM Gopinath-Style Flux Observer**

This chapter explores the implementation of a correction factor for the flux linkage observer. The simulation implementation and benchmarks the results. Afterwards the parameter sensitivity of the proposed system is analyzed.

## **Chapter 4: Effect of the Iron Losses in the IPMSM drive.**

This proposes the inclusion of an iron loss model into the flux linkage and current observers. It begins with the modeling of the system and the estimation of the iron losses and iron loss resistance from experimental data. Then it provides insight to the problems introduced by the iron losses. Finally, a correction factor is proposed, and its characteristics are modeled in simulation.

## **Chapter 5: Open Loop Tests and Implementation**

In this section the performance and evaluation of the proposed improvements to the Flux Observer is tested in open loop. The results are compared with the current implementation at Audi AG.

## **Chapter 6: Conclusions and Outlook**

This chapter indicates the conclusions reached out of the thesis work and outlooks a future path for research in this field.

# Chapter Two

## 2 Literature Review

Chapter structure:

First, the technical background respect the current implementation of Deadbeat Direct Torque and Flux Control and the system be enhanced is presented.

Second, the Gopinath style flux linkage observer is presented, and its construction is analyzed. The Voltage and Current models are explained, and its current state of the art is presented.

Thirdly, improvements proposed in papers and conferences are presented and analyzed.

The review is then assessed in answer to the requirements of the application under study.

### 2.1 The Interior Permanent Magnet Synchronous Machine IPMSM

An IPMSM is an electric machine whose rotor has embedded magnets as shown in Figure 1.

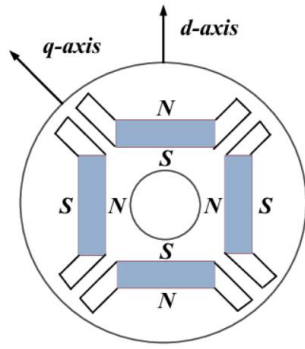


Figure 1 IPMSM basic rotor structure. Cross sectional view of the rotor. [3]

If the equations for the IPMSM in the rotor reference frame are considered, the voltages can be expressed in the stator of the machine as a function of the stator flux linkages and the stator currents as:

$$V_{ds}^r = R_s I_{ds}^r(t) + \frac{d\lambda_{ds}^r(t)}{dt} - w_e \lambda_{qs}^r(t) \quad (1)$$

$$V_{qs}^r = R_s I_{qs}^r(t) + \frac{d\lambda_{qs}^r(t)}{dt} + w_e \lambda_{ds}^r(t) \quad (2)$$

Where:

$$\lambda_{ds}^r(t) = L_d i_{ds}^r + \lambda_{pm} \quad (3)$$

$$\lambda_{qs}^r(t) = L_q i_{qs}^r \quad (4)$$

An equation for the machine torque is as well presented:

$$T_{em} = \frac{3}{2} \frac{P}{2} [(L_d - L_q) i_{ds}^r i_{qs}^r + \lambda_{pm} i_{qs}^r] \quad (5)$$

In equation 5 one of the key properties of the IPMSMS becomes apparent, this machine has both reluctance and Permanent Magnet flux-based torque components. The inductance  $L_d$  is smaller than  $L_q$  and therefore when  $i_{ds}^r$  is negative an addition to the total Tem is created. [4]

The losses in IPMSM are mainly copper losses at low speed. As the machine speeds up iron losses become more significant than the copper losses. As the machine speeds up the Electro Magnetic Force of the motor grows proportionally. [5]

While speeding up the machine below based speed, in order to minimize the copper losses Maximum Torque per Ampere strategies (MTPA) is typically implemented. Above based speed the MTPA strategy must be modified because the voltage limits are reached, this operation region is called the flux-weakening region.

The voltage constraints for the machine under a PWM inverter are so that:

$$V_d^2 + V_q^2 \leq \left( \frac{V_{dc}}{\sqrt{3}} * \cap \right)^2 \quad (6)$$

Where  $\frac{V_{dc}}{\sqrt{3}} * \cap = V_{max}$  and  $\cap$  is a factor to correct for the dead time of the inverter.

The voltage equation can be expressed by replacing the machine equations (1) and (2) in equation (6) forming:

$$\frac{\left( i_d + \frac{\lambda_{pm}}{L_d} \right)^2}{L_q^2} + \frac{(i_q)^2}{L_d^2} \leq \frac{V_{max}^2}{W_r L_d L_q} \quad (7)$$

This equation has an elliptical form if considered in the  $i_{ds}$  -  $i_{qs}$  plane.

On the other hand, the stator currents are constrained so that:

$$i_d^2 + i_q^2 \leq I_{max}^2 \quad (8)$$

This equation has a circular form if considered in the  $i_{ds}$  -  $i_{qs}$  plane.

Now if equation 5 is considered and manipulated considering the short-circuit current  $I_{sc}$  and the saliency ratio  $\delta$ , it can shape as:

$$i_{qs}^r \left( i_{ds}^r - \left( \frac{I_{sc}}{\delta - 1} \right) \right) = \frac{-T_e}{\frac{3}{2} \frac{P}{2} \lambda_{pm}} \left( \frac{I_{sc}}{\delta - 1} \right) \quad (9)$$

Where

$$I_{ds}^r = -I_{sc} = -\frac{\lambda_{pm}}{L_d} \quad (10)$$

$$\delta = \frac{L_q}{L_d} \quad (11)$$

It is important to notice that equation 9 has a hyperbolic shape, whose center is in  $-I_{sc}$ .

In the following figure (Figure 2 IPMSM Maximum torque per ampere), the trajectory of the machine for an infinite-speed drive is shown.

At the beginning, the machine has no current, and therefore the curve starts at the origin. In the section 1-2 of the curve displayed, the maximum torque as possible is reached by injecting the current in an angle in the left upper half plane. The exact slope will depend on the machine characteristics. In this way, the most outer torque line as possible can be reached. This is the constant torque region of the machine. As seen in the left upper graph of the figure.

At point 1, the voltage limit is reached and the machine critical speed. Here in order to keep increasing the speed of the machine, the maximum possible current must be used. The trajectory is now over the maximum current circle and moves towards point 2. This trajectory is the previously mentioned MTPA and it occurred in the constant power region as shown in the left lower graph.

At point 2, the back electromotive force is equal in magnitude to the voltage, and therefore, some of the current is used to fight it. As a result, the voltage ellipsis begins to shrink, and the current begins to drop. The trajectory that produces the most torque leads from 2 to 3. This operation is known as the Maximum Torque Per Flux. Once point 3 is reached, the machine has reached theoretically its maximum speed. The center of the ellipsis is as explained earlier as in equation 10.

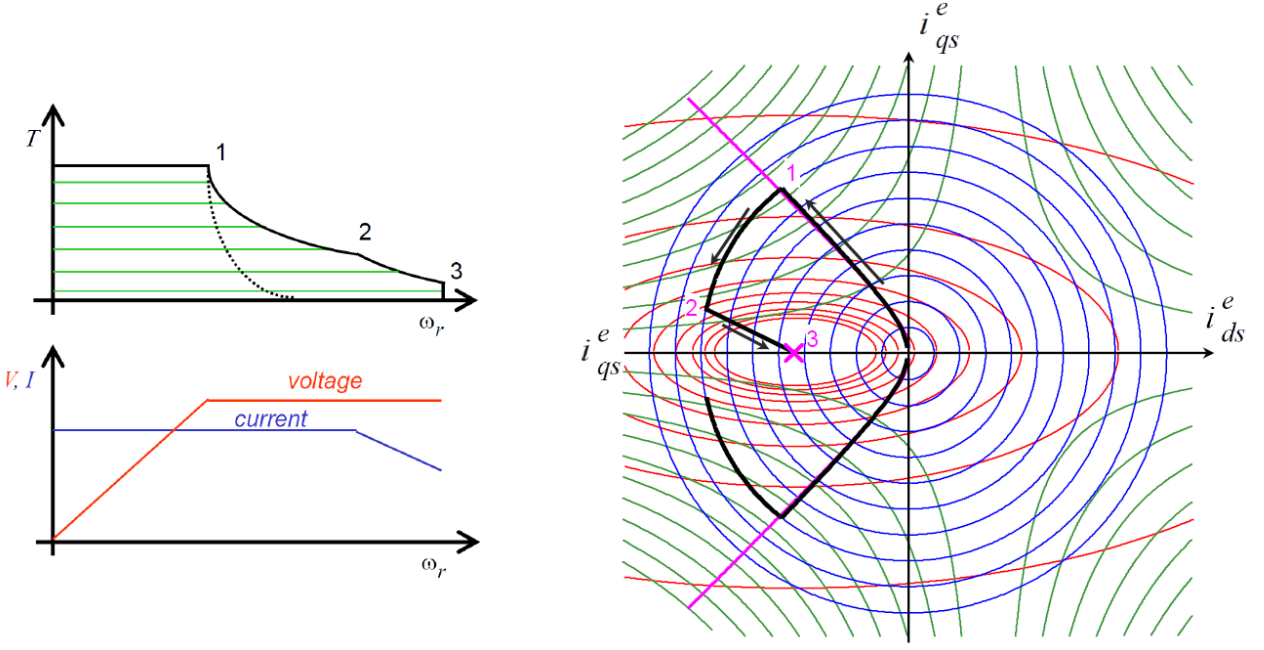


**Figure 2 IPMSM Maximum torque per ampere. [6]** At the left the torque vs rotor speed on the top and the current and voltages, at the right the maximum torque per ampere and maximum torque per flux trajectories are displayed.

According to [6], the base speed in such a machine can be calculated as:

$$w_{base} = \frac{V_{smax}}{\sqrt{(L_d i_{d1} + \lambda_{pm})^2 + (L_q i_{q1}')^2}} \quad (12)$$

$$i_{d1} = \frac{\lambda_{pm} - \sqrt{\lambda_{pm}^2 + 8(L_q - L_d)^2 I_{smax}^2}}{4(L_q - L_d)} \quad (13)$$

$$i_{q1} = \pm \sqrt{I_{smax}^2 - i_{d1}^2} \quad (14)$$

In addition, if equation (15) is solved under the MTPF assumptions, the critical speed can be obtained.

$$\frac{V_{smax}^2}{W_e} = (L_d I_d + \lambda_{pm}) + L_q^2 (I_{smax}^2 - i_d^2) \quad (15)$$

## 2.2 IPMSM Control Methods

Let's consider the torque expression in equation (5). In an electric, drive an infinite number of Idq vectors can be used to produce a certain amount of electromagnetic torque. Nevertheless, a unique minimum loss operation point exists when the currents are minimized. This optimum is valid for the region where the copper losses are dominant. This operation refactory is known as MTPA [4]

In traction drives, a control of the torque is required. Many implementations consider Lookup tables to make Current Vector Control (CVC). In this implementation, the d and q axis currents are regulated according to their reference values. A general control diagram of this implementation is displayed in the following figure (see fig 3). This implementation although very common has some clear disadvantages. It is sensitive to parameter estimation error and windup problems.

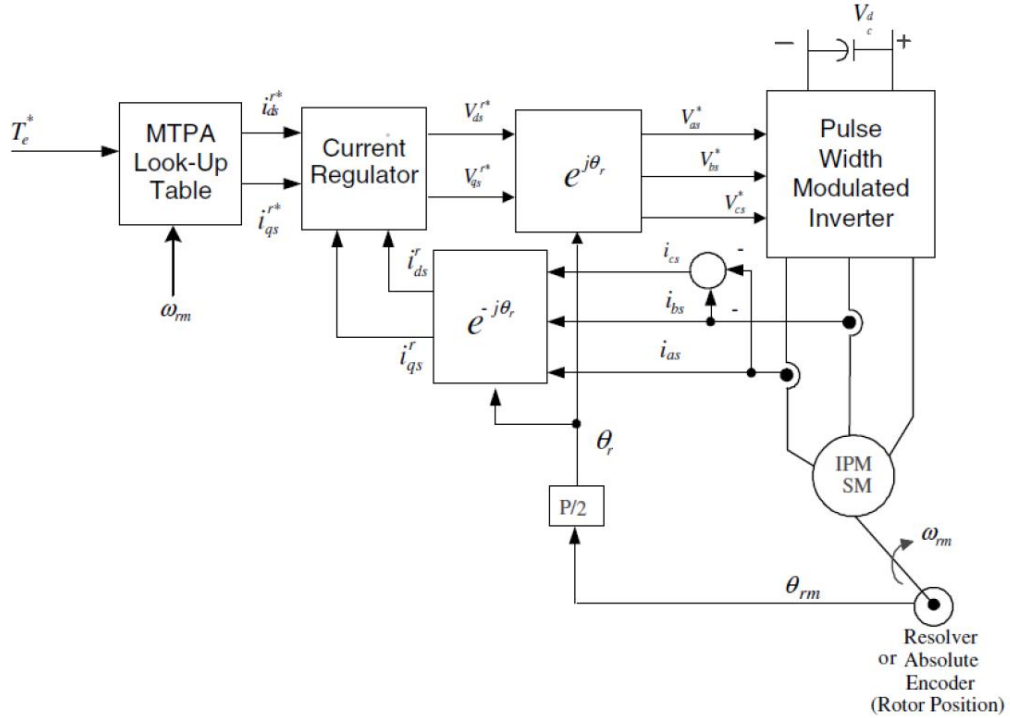


Figure 3 CVC block diagram [4]. The block diagram of a typical CVC control system is displayed.

Another very well-known control option is called Direct Torque Control or DTC [7]. This AC machine control methodology is developed in such a way that torque and flux are controlled with a hysteresis controller. While doing so, the suitable inverter voltage vector is selected. In order to use a torque and flux feedback, those two parameters must be estimated. The torque is estimated based on the following equation:

$$Te = \frac{3}{2} \frac{p}{2} [\lambda_{ds}^r i_{qs}^r - \lambda_{qs}^r i_{ds}^r] \quad (16)$$

Moreover, in order to estimate the flux, a flux observer block based on the machine equations is implemented as following.

$$V_{ds}^s = R_s I_{ds}^s + \frac{d\lambda_{ds}^s}{dt} \quad (17)$$

$$V_{qs}^s = R_s I_{qs}^s + \frac{d\lambda_{qs}^s}{dt} \quad (18)$$

Finally, in order to implement hysteresis controllers a switching table is implemented. This table (see Table 1) provides the corresponding voltage vector that matches the desired flux and torque commands. The resulting control scheme is displayed in Figure 4. This control system has two major drawbacks, an unpredictable switching frequency that causes the losses to be increased and a high steady state ripple.

$\Delta_{e\lambda}$	$\Delta_{eT}$	$\theta$					
		$\theta_1$	$\theta_2$	$\theta_3$	$\theta_4$	$\theta_5$	$\theta_6$
1	1	u2	u3	u4	u5	u6	u1
	0	u6	u1	u2	u3	u4	u5
0	1	u3	u4	u5	u6	u1	u2
	0	u5	u6	u1	u2	u3	u4

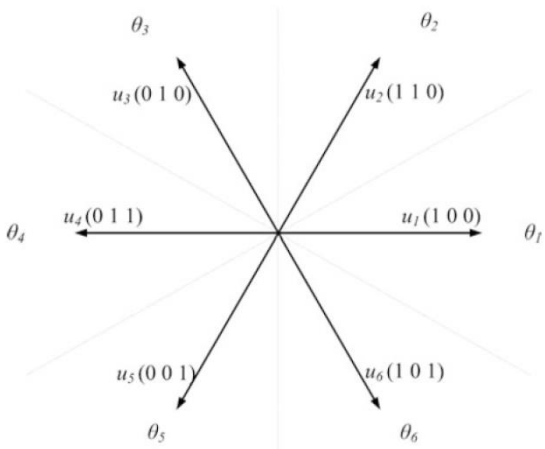
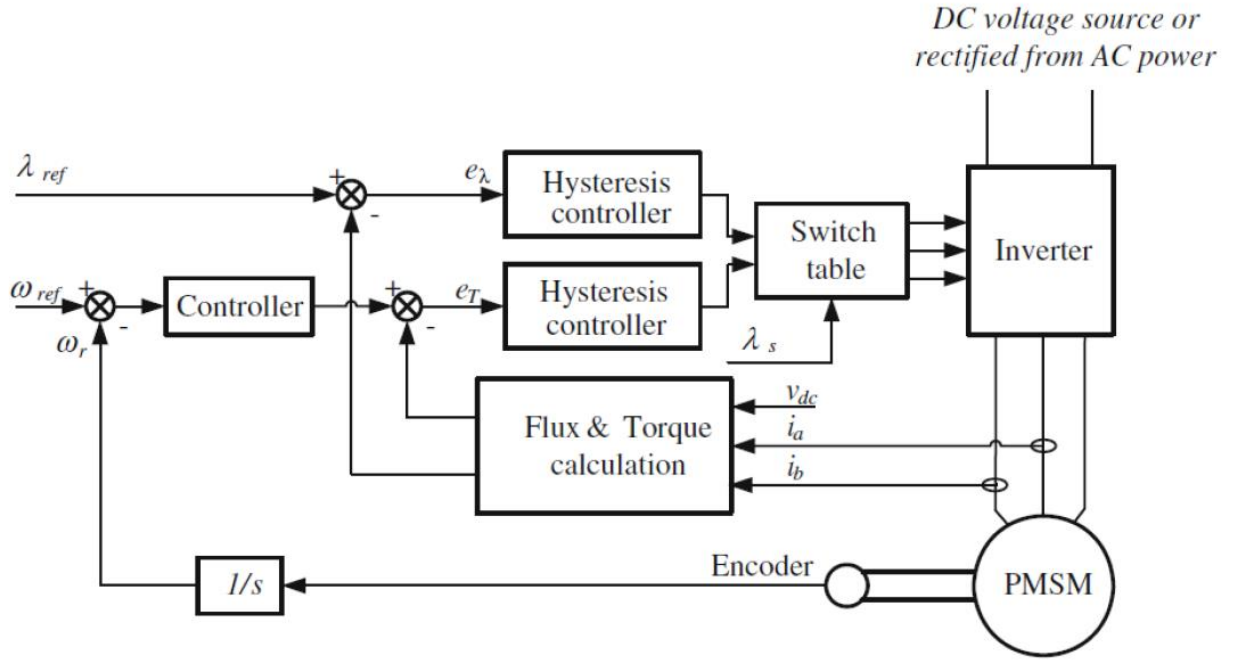


Table 1 DTC Vectors Switching Table [7]



**Figure 4 DTC control Block Diagram [7].** A DTC system with hysteresis control is described. The control variables are the speed and flux of the machine.

In the block diagram of Figure 5, the DTC system uses a flux and torque observer from where the flux and torque loops are closed. The speed control loop is cascaded over the torque loop.

## 2.3 Dead Beat Direct Torque and Flux Control (DB-DTFC) for IPMSM

DB-DTFC is a digital control method for IPMSM that uses the inverse model of the machine is solved. The desired machine voltage vector is calculated so that the change in the torque that matches the reference is obtained. As a result, the desired air gap reference and flux is achieved in one switching period. Therefore, its name “Dead in one Beat”.

In the next section, the algorithm described by [8] will be explained and its key advantages will be pointed out.

### 2.3.1 DB-DTFC algorithm.

The flux linkage derivative terms of the IPMSM machine equations in rotor reference frame, can be expressed as:

$$\frac{d\lambda_{ds}^r}{dt} = V_{ds}^r - R_s I_{ds}^r + w_e \lambda_{qs}^r \quad (19)$$

$$\frac{d\lambda_{qs}^r}{dt} = V_{qs}^r - R_s I_{qs}^r - w_e \lambda_{ds}^r \quad (20)$$

Where

$$\lambda_{ds}^r = L_d i_{ds}^r + \lambda_{pm} \quad (21)$$

$$\lambda_{qs}^r = L_q i_{qs}^r \quad (22)$$

An alternate form of this equation reached if the stator currents are replaced by an expression in terms of the fluxes. Replacing equations (21) and ((22) into (19) and (20) the following equations are obtained:

$$\frac{d\lambda_{ds}^r}{dt} = V_{ds}^r - \frac{R_s}{L_{ds}} (\lambda_{ds}^r - \lambda_{pm}) + w_e \lambda_{qs}^r \quad (23)$$

$$\frac{d\lambda_{qs}^r}{dt} = V_{qs}^r - \frac{R_s}{L_{qs}} (\lambda_{qs}^r) - w_e \lambda_{ds}^r \quad (24)$$

The time derivatives of the stator currents can be expressed in a similar way as function of the fluxes so that:

$$i_{ds}^r = \frac{\lambda_{ds}^r}{L_{ds}} \quad (25)$$

$$i_{qs}^r = \frac{\lambda_{qs}^r}{L_{qs}} \quad (26)$$

The electromagnetic torque and its time derivative are expressed in terms of the fluxes as well

$$Te = \frac{3p}{2} \frac{2}{2} [\lambda_{ds}^r i_{qs}^r - \lambda_{qs}^r i_{ds}^r] \quad (27)$$

$$\dot{Te} = \frac{3p}{2} \frac{2}{2} [\lambda_{ds}^r \dot{i}_{qs}^r + \lambda_{qs}^r \dot{i}_{ds}^r - \lambda_{qs}^r \dot{i}_{ds}^r - \lambda_{ds}^r \dot{i}_{qs}^r] \quad (28)$$

Now if for instance a small switching period  $T_s$  is considered where the change of the factors is maintained constant, the torque equation derivative can be expressed as a difference equation if discretized using Euler's approximation as:

$$\dot{T}_e = \frac{T_e(K+1) - T_e(K)}{T_s} \quad (29)$$

By substituting equations (23),(24),(25),(26) ,(29) in equation(28) the following equation is formed:

$$\begin{aligned} & \frac{T_e(K+1) - T_e(K)}{T_s} \\ &= \frac{3}{2} \frac{p}{2} [V_{ds}^r(k) \lambda_{qs}^r(k) \left( \frac{L_d - L_q}{L_d L_q} \right) \\ &+ V_{qs}^r(k) \frac{(L_d - L_q) \lambda_{ds}^r(k) + \lambda_{pm} L_q}{L_d L_q} \\ &+ \frac{w_e(k)}{L_d L_q} ((L_d - L_q)(\lambda_{ds}^r(k)^2 - \lambda_{qs}^r(k)^2) - L_q \lambda_{ds}^r(k) \lambda_{pm}) \\ &+ \frac{R_s \lambda_{qs}^r(k)}{L_d^2 L_q^2} ((Lq^2 - L_d^2) \lambda_{ds}^r(k) - L_q^2 \lambda_{pm})] \end{aligned} \quad (30)$$

Note that equation (30) presents a linear relationship between the d and q axis stator voltages. This relationship can be represented as

$$V_{qs}^r(k) T_s = M * V_{ds}^r(k) + B \quad (31)$$

Where

$$M = \frac{(L_q - L_d) \lambda_{qs}^r(k)}{(L_d - L_q) \lambda_{ds}^r(k) + \lambda_{pm} L_q} \quad (32)$$

$$\begin{aligned} B = & \left( \frac{L_q L_d}{(L_d - L_q) \lambda_{ds}^r(k) + L_q \lambda_{pm}} \right) \left[ \frac{2 \Delta T_e}{3p} \right. \\ & - \frac{T_s W_e}{L_q L_d} ((L_q - L_d)(\lambda_{ds}^r(k)^2 - \lambda_{qs}^r(k)^2) - L_q \lambda_{ds}^r(k) \lambda_{pm}) \\ & \left. - \frac{R_s T_s \lambda_{qs}^r(k)}{Lq^2 L_d^2} ((Lq^2 - L_d^2)(\lambda_{ds}^r(k) - L_q^2 \lambda_{pm})) \right] \end{aligned} \quad (33)$$

By analyzing equation 31, it is apparent that multiple stator voltage vectors exist for a given desired change in torque in the next sampling period. All of them archiving Deadbeat torque control.

If any arbitrary vectors would be used to achieve this, the flux changes would be uncontrollable. Therefore, a flux linkage Deadbeat control is necessary. To implement such a solution equations (23) and (24) are modified until equation (34) is obtained. To do so, the cross-coupling terms are decoupled, and the stator resistance is neglected. [8]

$$\lambda_{dqs}^r(k+1) = \lambda_{dqs}^r(k) + V_{dqs}^r(k)T_s \quad (34)$$

To get a constant flux linkage magnitude, a circular trajectory like expression can be build:

$$\lambda_s^*(k)^2 = \lambda_{ds}^r(k+1)^2 + \lambda_{qs}^r(k+1)^2 \quad (35)$$

And if equation (31) is substituted in (35), the expression obtained is:

$$\lambda_s^*(k)^2 = (\lambda_{ds}^r(k) + V_{ds}^r T_s)^2 + (\lambda_{qs}^r(k) + V_{qs}^r T_s)^2 \quad (36)$$

The DB\_DTFC commands are obtained by combining (31) and (36):

$$V_{ds}^r(k+1) = \frac{-b \pm \sqrt{b^2 - 4ac}}{2a} \quad (37)$$

$$v_{qs}^r(k+1) = M V_{ds}^r(k+1) + \frac{B}{T_s} \quad (38)$$

Where

$$a = (M^2 + 1)T_s^2 \quad (39)$$

$$b = 2T_s(\lambda_{ds}^r(k) + M\lambda_{qs}^r(k) + MB) \quad (40)$$

$$c = \lambda_{ds}^r(k)^2 + \lambda_{qs}^r(k)^2 + B^2 + 2\lambda_{qs}^r(k)B - \lambda_s^*(k)^2 \quad (41)$$

### 2.3.2 DB\_DTFC graphical Interpretation

A graphical interpretation of equation (31) in (35) is presented in the following section. It has already been discussed that equation (31) is a line when represented in the dq stator voltage plane (Red curve). The Flux linkage equation presented in (35) is represented in terms of the stator voltage forming a circle of radius  $\lambda_{dqs}^r(k)$  (Black circle), the inverter voltage limits form a hexagon. At its peak the hexagon has a size of  $\frac{2}{3}V_{dc}$ . The two blue vectors show the two possible solutions to the stator voltage that can achieve the DB-DTFC. The smaller vector is the one selected.

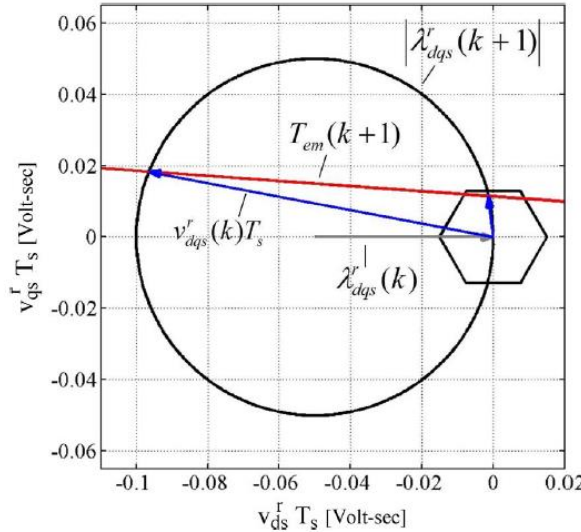


**Figure 6 DB-DTFC Graphical Solution [8]. (Red) the torque equation line for the k+1 instant, (Black circle) the dqs flux linkage limits, (Black Hexagon) inverter voltage limit.**

### 2.3.3 DB\_DTFC System Block Diagram:

As exposed by [9] (see fig. 7 ) in a DB-DTFC control scheme, the torque command comes from the Motion Controller, but the flux command comes from the loss minimization algorithm. From this input the DB-DTFC algorithm generates the voltage vectors.

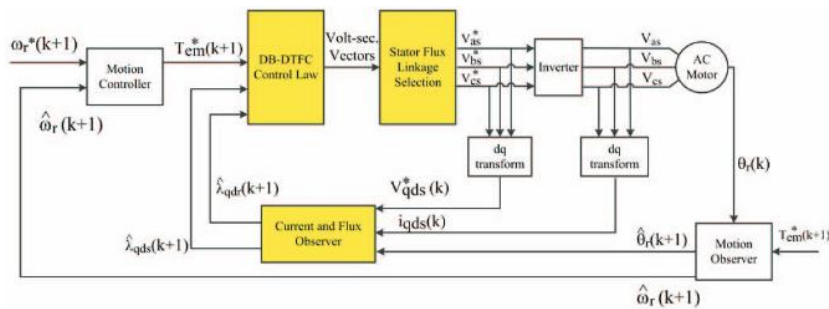


**Figure 7 Deadbeat Direct torque control typical application block diagram by [9]. (Yellow) DB-DTFC required blocks for the Control Law. Note the presence of a Full Order current and flux linkage observer.**

It is important to notice that the current and flux observer works estimating the (K+1) signals from the measured variables at a time instant (k). Differing from other control systems here the current in the next instant needs to be estimated. For this calculation proper event timing, since it is a discrete

control system, is critical for the implementation. The use of observers if implemented correctly, can overcome undesirable system dynamics, due to its prediction capability.

The events and timing are also described by [9] in a figure. (See fig. 8 )

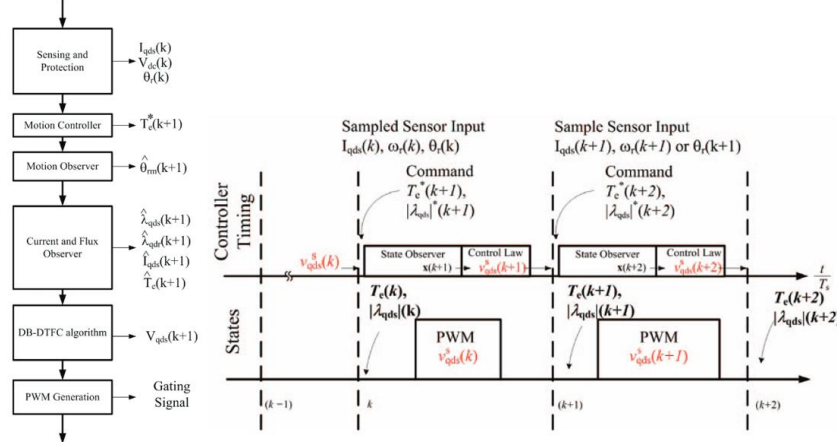


**Figure 8** Event timing on DBDTFC control in one sampling period. [9]. The timing for each process signal is displayed on the left. It is important to note the in advance ( $k+1$ ) instant input requirements for the system computation.

## 2.4 The Luenberger-style current observer.

In order to predict the current in the next sampling instant, a discrete time Luenberger-style current observer is implemented in the rotor reference frame as represented in the Figure 9.

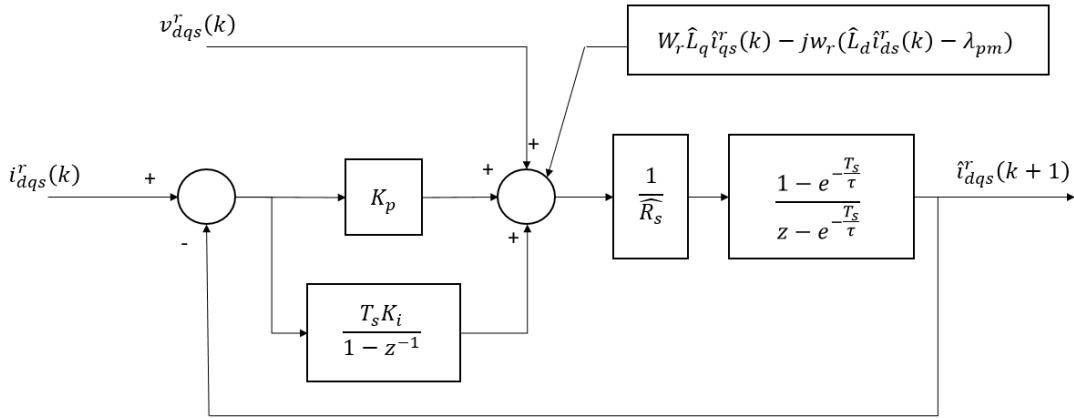


**Figure 9** Discrete Luenberger-style Current Observer [2]. The observer is based on the IPMSM voltage equation. It seeks to predict the current in the next sampling instant ( $k+1$ ).

This discrete observer uses the IPMSM model in the rotor reference frame with the estimated parameters and to predict the future state of the stator currents. The predicted currents are feedback for a PI regulator that aims to reduce the estimation error.

## 2.5 Flux linkage estimation with a Gopinath Style flux observer

For DeadBeat direct torque control, the stator flux linkage and torque in the next sampling period must be calculated. Since measuring the stator flux linkage is not practical, a Gopinath-style observer is used. This kind of observer, as described in [8], uses a current based flux linkage observer in combination with a voltage-based observer. However, the implementation described by this author is in the rotor reference frame.

However, as explained in [9], a synchronous reference frame model is dependent to speed, and therefore a PI controller is used to control the impact shared on the flux between the voltage and current model. By combining both models, the parameter insensitivity of the models can be best utilized.

The current model observer is based on the following equation:

$$\lambda_{dqs}^r(k) = i_{dqs}^r L_s + \lambda_{pm} \quad (42)$$

The current model is sensitive to permanent magnet flux linkage and stator inductance parameter variation but is speed independent. The last is only truth if no Iron-losses are considered.

In order to construct the voltage model, the IPMSM voltage equation in the stationary reference frame can be expressed as:

$$\frac{d\lambda_{dqs}^s}{dt} = V_{dqs}^s + R_s i_{dqs}^s \quad (43)$$

If then a small switching period  $T_s$  is considered so that the flux linkage derivative can be expressed as a difference equation. In such a small switching period, the voltage acts as a latched value. However, the current increases linearly like a ramp. If the nature of the different inputs is taken into consideration, the discretization methods must be different for each signal type. For the voltage, a zero-order hold approximation is used, while the first order hold or Tustin method must be used for the current. Finally, the equation can be written as:

$$\lambda_{dqs}^s(k+1) - \lambda_{dqs}^s(k) = V_{dqs}^s(k)T_s + R_s \frac{T_s}{2} (i_{dqs}^s(k) - i_{dqs}^s(k+1)) \quad (44)$$

The voltage model is very sensitive at low speeds where the voltage drop caused by the stator resistance is none negligible. Any variation in the stator resistance can produce a considerable deviation in the estimation. The accuracy of this model is speed dependent, at high speeds the estimation accuracy increases.

In order to use the best of both models, the output of the current model can be transformed into the stationary reference frame. This signal is then compared via feedback with the voltage model output of the previous sampling instant. The error is feed to a PI controller and used to correct the model.

At low speeds, the PI controller controls the observer dynamics and therefore the current model is dominant and feed forward. When the operation speed is above the controller bandwidth, the controller can no longer control the input and then the voltage model becomes dominant.

The controller bandwidth must be then set to a point of the transition between the models. A balance in parameter sensitivity between the two models must be studied. This can be done while studing the machine under regular FOC or Volts/Hz operation. While running the observer models and comparing their results. This exact tuning will be explored further on this chapter.

The system resulting from these observers displayed in block diagrams in Figure 10.

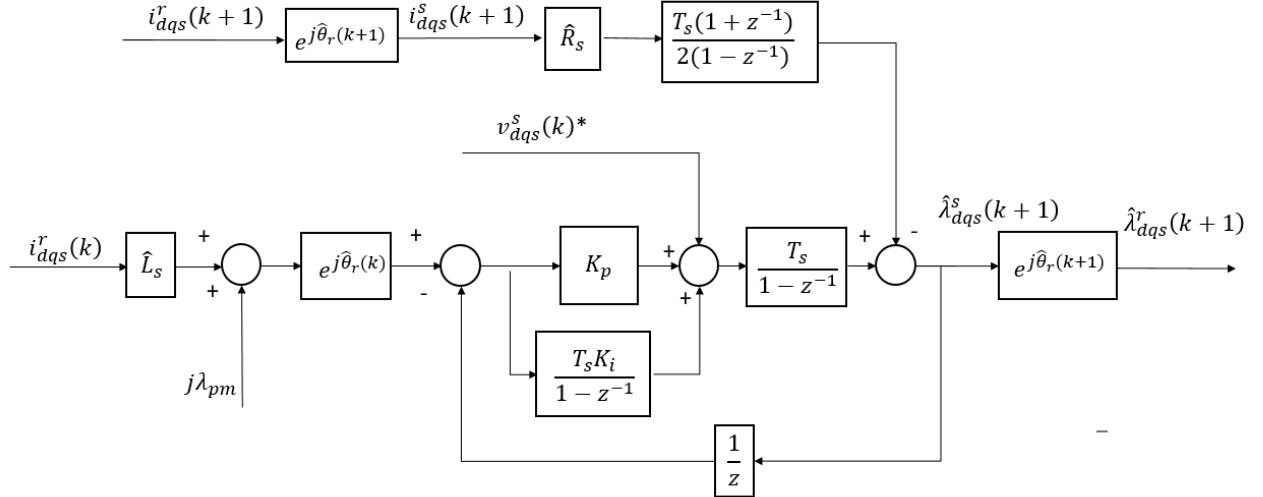


**Figure 10 Gopinath Style Flux Observer.** The concept is explained in [4] the figure is self elaborated. At the left side the current model, after the stator reference frame transform the PI controller and then the voltage model.

### 2.5.1 Flux observer controller tuning.

The observer-tuning path can be also expressed as the following simplified form:

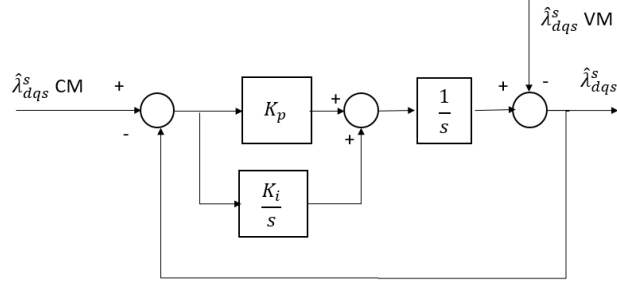


**Figure 11 Flux Linkage estimator Control Tuning Path [4]. The VM is operated so that  $\lambda_{dqs}$  path is the only output.**

If block diagram algebra is used, the equivalent z-domain transfer function is obtained:

$$\frac{\lambda_{dqs}^s(k+1)}{\lambda_{dqs}^s(k)} = \frac{z^2(K_i T_s^2 + K_p T_s) + z(-K_p T_s)}{z^2 + (K_i T_s^2 + K_p T_s - 2) + (1 - K_p T_s)} \quad (45)$$

The behavior of the system described by equation (45) can be compared with a generic second order transfer function. The form of a generic transfer function has the following characteristic denominator:

$$z^2 - (z f_1 + z f_2)z + (z f_1 z f_2) \quad (46)$$

$$z f_1 = e^{-2\pi T_s f f 1} \quad (47)$$

$$z f_2 = e^{-2\pi T_s f f 2} \quad (48)$$

Therefore, the eigenvalues or system poles can be obtained therefore by comparing the denominator of equation 45 with equation 46.

We can then express the proportional and integral gains of the controller as function of the eigenvalues.

$$K_p = \frac{1 - z f_1 z f_2}{T_s} \quad (49)$$

$$K_i = \frac{2 - K_p T_s - (zf_1 + zf_2)}{T_s^2} \quad (50)$$

The two fastest poles of this system will dominate the system dynamics, and therefore will control the bandwidth. The second pole will play a role in controlling the transition of the system.

As suggested in many different papers like [9], the typical practice is to fixed distance between poles of 1:10. So that the fastest dynamic pole dominates the transition and the other has impact in the transient.

### 2.5.2 Gopinath-style flux observer PI controller role

We could define the tuning pad of the controller in a simplified way as in Figure 12. Considering for instance the transfer functions of this system, it is possible to see that a relationship between the fluxes can be established as:

$$\hat{\lambda}_{dqs}^s = A * \hat{\lambda}_{dqs}^s VM + B * \hat{\lambda}_{dqs}^s CM \quad (51)$$

Where:

$$A = \frac{s^2}{s^2 + K_p * s + K_i} \quad (52)$$

$$B = \frac{K_p * s + K_i}{s^2 + K_p * s + K_i} \quad (53)$$

It is simple to prove that

$$A + B = 1 \quad (54)$$

We can see that the dependency of the output is a mix between the two speeds that depends on the controller gains. In the following figure a bode diagram of A and B is displayed.

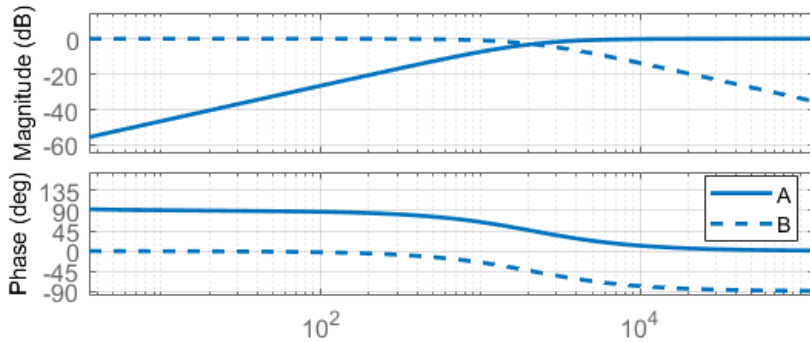


**Figure 13** Bode diagram of A and B. The equivalent poles of this system are located at 314 and 31 rad/s respectively. A line is placed at the controller tuning frequency. The transition between the voltage and current model dominance can be therefore explained through the frequency response of the system.

From Figure 13 it is possible to see that at low frequency; the gain of A is very small, and the gain of B is close to unity. At high speeds, the opposite is true as well. Nevertheless, it can be noticed that in the transition between the models, a Phase change exists and therefore a distortion is expected.

### 2.5.3 Angle for the reference frame transforms.

As mentioned in [8] the flux observer's voltage model signals are from different types and therefore different discretization methods for the integrators are used. In a sampling instant, the phase voltage is latched while the rotor angle, the stator current and the flux linkages from the Current and Voltage models are assumed to change linearly inside the machine.

The signal types can be defined as ramp type for the current measurement and latched values type for the voltage. Therefore, the ramp signals are discretized with a First Order Hold method while an Impulse invariant discretization is used for the current path. As displayed in the following figure the integrators have different discrete shapes:

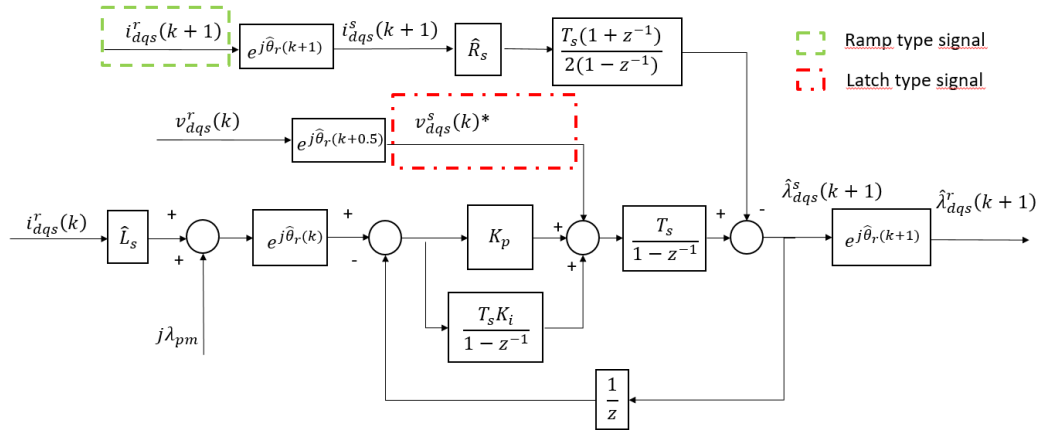


**Figure 14 Stator Flux Linkage Observer Voltage Model signal types. [10]. Shows the observer topologies and the signal types for the different paths. (Red) Latch Type, (Green) Ramp type.**

It is important to notice that the signals in the stator reference frame implementation will have to be transformed to the stator reference frame. A correct angle for the reference frame transformation is critical for the estimation.

As explained by [10] in chapter 3.1.2, the voltage model of the flux linkage estimation has a step ahead property. Therefore a (k+1) step ahead angle must be used for the voltage model flux linkage transformation. On the other hand, the PI controller input signal compares the current (k) instant values of the flux linkages, therefore a delay in the feedback must be used and a (k) reference frame transform angle for the current model flux linkage.

The stator current ( $k+1$ ) at time sampling instant is feed to a trapezoidal integrator, therefore the angle required for the reference frame transform is a  $(k+1)$  angle.

A special case occurs with the stator voltage. It results interesting to notice that the voltage applied by an inverter in a sampling instant is the average between the voltage at  $(k)$  and the voltage applied at  $(k+1)$ . Therefore, in order to minimize the error respect, the real stator voltage, the angle for the reference frame transform is a  $(k+1/2)$  angle.

Then the angle required for the reference frame transform must be adjusted so that it matches the signal instant. It can be assumed that for a small sampling period the speed is kept constant a therefore if an offset  $d$  is defined as a value between zero and one, the angle  $(k + d)$  can be calculated as in the following block diagram:

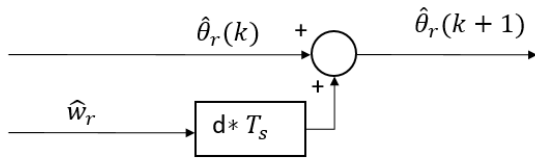


**Figure 15 Discrete Gopinath-style flux observer angle time instant adjustment.** This angle adjustment is applied at the entrance of the reference frame transform in order to match the delay to the signal type.

## 2.6 Latest advancements literature review:

The implementation issues are very well documented at [9] and the robustness of DB\_DTFc is analyzed in [2].

As shown by these authors the Gopinath-style flux linkage observer has several implementation difficulties like:

- The transition between the models produces a distortion area
- The determination of the ideal bandwidth of the controller
- The effect of the second pole on the system
- Parameter sensitivity respect the Stator Resistance, the Permanent Magnet Flux, the inductances.
- High-Speed error increase
- High computational efforts are required and is constrictive for some systems

Many papers review possible improvement methods for the flux linkage observer. It is possible to sort the new proposals following categories.

- Observers Current Model Reliability and resilience to parameter variation. [11], [12], [13], [14].
- Observers Voltage Model Accuracy and error correction at high speeds. [15], [16], [17].

- Observer Current to Voltage Model Transition enhancement. [18].
- Observer disturbance rejection capability. [19].
- Observer Computational effort optimization. [20].

In the following section, the most significant proposal of several of these authors will be analyzed.

### **2.6.1 Implementation Issues of DB\_DTFC**

According to [9] DB-DTFC presents a different implementation issue as other drive systems due to the discrete formulation of the method and its requirements of estimating currents at instances (K+1) and flux linkages at (k+1). This author suggests a logical sequence to follow for the correct implementation. This sequence will be briefly summarized and explained.

1. Understanding the time sequence of DB-DTFC in its direct form.
  - a. The author suggests taking special care respect to the observers that need to estimate signals in a (k+1) instant, variables like the angles for the reference frame transforms must be therefore considered.
  - b. The timing is described as in figure 8 of section 2.3.3.
2. The author suggests the implementation of FOC or V/Hz for the drive in parallel so that the system can be tuned. If the drive working under FOC or V/Hz is assumed to work ideally, the signals coming from the drive can be used to perform the following tasks:
  - a. Tune the current observer of the system and to check that the observer correctly predicts the current in the next instant.
  - b. Tune the required frequency response of the current observer and the dynamic stiffness.
  - c. Experimentally evaluate the torque and flux estimates.
3. Under this parallel open-loop configuration, the flux observer can be tuned. The results can be verified experimentally. A rule of thumb on how to place the poles of the resulting system is described so that one of the poles is 10 times faster than the other one.
4. Implement closed loop DB-DTFC control laws. Consider only feasible trajectories for the torque and flux commands.
5. Select the switching frequency. It is suggested to lower the switching frequency to maximize the single step torque capability of DB-DTFC. Since the Volt-sec hexagon used for the graphical solution of DB-DTFC has a size that is function of the dc link voltage and the switching period.

## 2.6.2 Disturbance Input Decoupling with Luenberger current observer

Some authors have started purposing improvements to the flux observer. In this section, some of the ideas proposed will be reviewed and later they will be considered and compared with the actual system.

A reduced parameter sensitivity observer was proposed by [11]. Since in DB\_DTC a Luenberger current estimator is used a Disturbance Input Decoupling (DID) term between the current observer and the flux linkage observer VM is proposed. Consider for instance the machine equations for the IPMSM (55) and (56).

$$V_{ds}^r = R_s i_{ds}^r(t) + L_d \frac{di_{ds}^r(t)}{dt} - w_e L_q i_{qs}^r(t) \quad (55)$$

$$V_{qs}^r = R_s i_{qs}^r(t) + L_q \frac{di_{qs}^r(t)}{dt} + w_e L_d i_{ds}^r(t) + w_e \lambda_{pm} \quad (56)$$

We can also describe the estimation at the next sampling instance done by the current observer according to. If now if the current observer tracks the measured currents well at steady state, the derivative terms are negligible. Then the output of the current regulator matches the stator voltages as in (57) and (58).

$$V_{ds}^r = \hat{R}_s \hat{i}_{ds}^r(t) + \hat{v}_{ds\_PI}^r - w_e \hat{L}_q \hat{i}_{qs}^r(t) \quad (57)$$

$$V_{qs}^r = \hat{R}_s \hat{i}_{qs}^r(t) + \hat{v}_{qs\_PI}^r - w_e \hat{L}_d \hat{i}_{ds}^r(t) + w_e \lambda_{pm} \quad (58)$$

If now equation (55) and (56) are analyzed in steady state and the voltage variables are replaced by (57) and (58). The difference between the estimated quantities and the actual measured ones is defined as (59) and (60).

$$\Delta \hat{R}_s \hat{i}_{ds}^r = \hat{v}_{ds\_PI}^r + w_e \Delta \lambda_{qs\_dist}^r \quad (59)$$

$$\Delta \hat{R}_s \hat{i}_{qs}^r = \hat{v}_{qs\_PI}^r - w_e \Delta \lambda_{qd\_dist}^r \quad (60)$$

Now the variation in resistance is neglected resulting in (61) and (62).

$$0 = \hat{v}_{ds\_PI}^r + w_e \Delta \lambda_{qs\_dist}^r \quad (61)$$

$$0 = \hat{v}_{qs\_PI}^r - w_e \Delta \lambda_{qd\_dist}^r \quad (62)$$

It is easy to explain that the PI regulator of the Luenberger current observer is active, whenever an error in the current exists. The observer's correction action is applied to the current observer through the integral action of its controller. This correction information is now forward as well into the current model-based observer part in the Gopinath-style flux linkage observer.

In order to implement such a correction, the integral flux model in the stator reference frame is used to estimate the disturbance. A high pas filter is a good option to avoid the integrator diverging to infinity due to any dc components in the signal. In addition, a low pas filter after the integrator can eliminate the problems caused by the nonlinearity of the power converter high frequency harmonics.

Considering now a block diagram of the proposed system, Figure 16 can be formed.

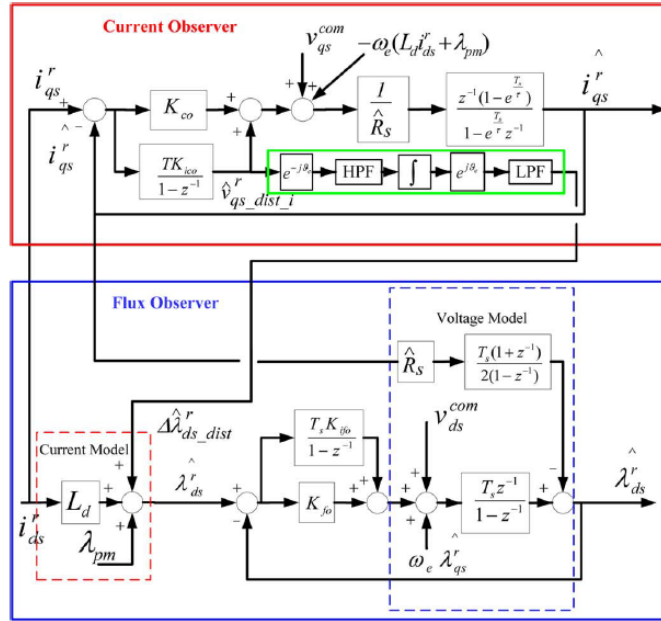


**Figure 16** Block diagram of the DID implementation in the d axis flux linkage observer [11]. In the figure q-axis Luenberger current Observer in red, d-axis Gopinath-style Flux linkage observer in blue and DID forward term in green.

The key advantages identified by the author in [11] are a dependence reduction respect to  $\lambda_{pm}$  and the inductance values at low speed.

For the implementation of this model in the described system, the park transformation back to the rotating reference frame is unnecessary.

The importance of the voltage compensation is also analyzed in [11], it is important to notice how the dead time of the switching semiconductors affects the solution. According to the author, this variable has a big impact on estimation quality.

The voltage is compensated via a linear approximation as represented in the following equation for phase a:

$$V_a^{comp} = \frac{T_d}{T_s} V_{dc} * sign(i_a) \quad (63)$$

The author shows the following results:

The author reports a clear improvement with its proposed solution, nevertheless this solution improves the current model resiliency, and some problems at high speeds might still be present.

### 2.6.3 Design of Flux Observer Robust to Parameter Variation of Interior Permanent Magnet Synchronous Motor

[12] Discusses a system in which a PI current regulator is implemented in for an IPMSM control scheme.

$$V_{CREG\ d}^* = Kp_d + \frac{Ki_d}{s} * I_d\ Err \quad (64)$$

$$V_{CREG\ q}^* = Kp_q + \frac{Ki_q}{s} * I_q\ Err \quad (65)$$

If the IPMSM equations (1) and (2) are considered. A decoupling term is used in high performance drives to decouple the back EMF term of the voltage equation.

In such a drive if the real currents track their references well in steady state, as far as the stator resistance does not change largely, the magnitude of the flux error can be calculated from the integral term of the PI controller as:

$$\Delta\lambda_{ds}^r = \frac{IA_{CREG\ d}^* - R_s I_{ds}^r}{W_r} \quad (66)$$

$$\Delta\lambda_{qs}^r = - \frac{IA_{CREG\ q}^* - R_s I_{qs}^r}{W_r} \quad (67)$$

Where  $IA_{CREG\ d}^*$  and  $IA_{CREG\ q}^*$  are the current controller integral actions of the current controller.

This modification to the Gopinath style flux observer shapes it in following way allowing.

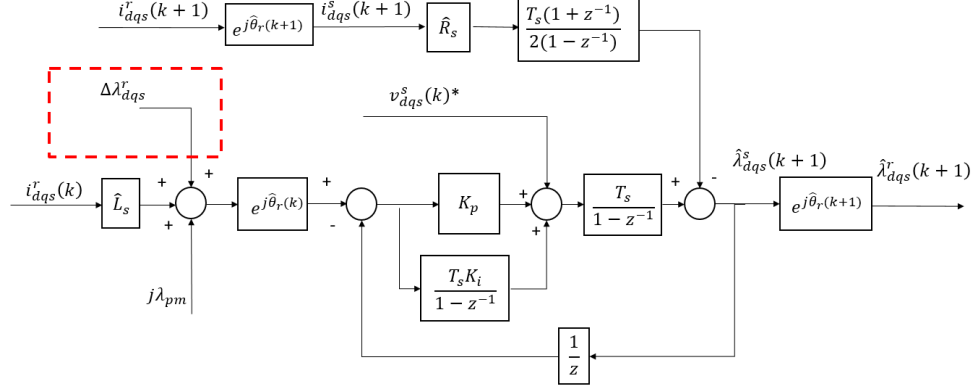


**Figure 17 Discrete Gopinath-style flux observer Yoo and Soul modification. (Red) The path where the Flux Linkage Difference is applied.**

The drive should be resilient to deviations on the Permanent magnet flux and the inductances.

In the case of Deadbeat DTFC, the current controller is nonexistent and therefore this solution is not feasible.

#### 2.6.4 Torque Error Compensation Algorithm for IPMSM

The authors of [13] propose to apply a correction to the current commands in order to reduce the torque error due to PM flux variations. The concept is based on applying two factors calculated from the amplitude difference between the flux linkages of the voltage and current models of the Gopinath-style flux linkage observer.

The correction factors are defined as:

$$K_{crd} = \frac{\lambda_q^r CM}{\lambda_q^r VM} \quad (68)$$

$$K_{crq} = \frac{\lambda_d^r CM}{\lambda_d^r VM} \quad (69)$$

The equivalent system is described as:

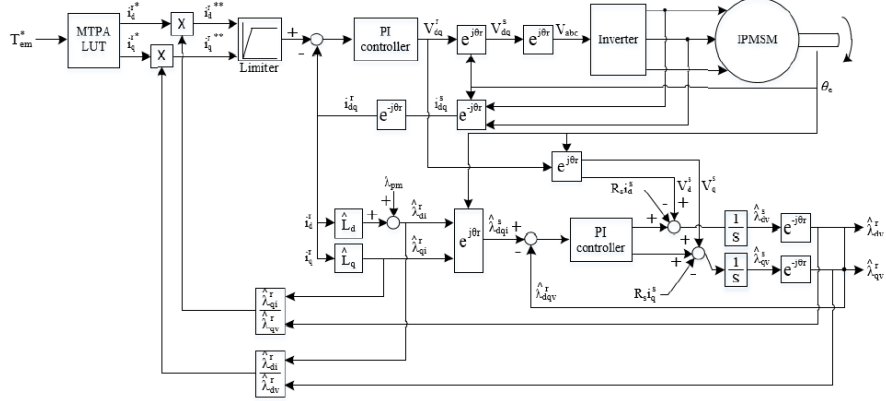


**Figure 18 Torque Error Compensation Control Scheme from [13] shows the introduction of a compensation factor in the current command; This correction seeks to enhance the torque equation accuracy under parameter deviation**

The resulting torque equation can be expressed as function of the estimated quantities and commands like:

$$Te = \frac{3}{2} \frac{p}{2} [\lambda_{ds}^r \frac{\lambda_d^r CM}{\lambda_d^r VM} i_{qs}^r - \lambda_{qs}^r * \frac{\lambda_q^r CM}{\lambda_q^r VM} * i_{ds}^r] \quad (70)$$

As apparent from the equation, if the current model parameters vary the flux linkage amplitude of the CM will be different from the one of the Voltage Model. The current command would be modified so that the amplitude is matched with the one of the voltage models. Since the accuracy of the voltage model at low speeds is poor, the correction is applied only above a certain minimum speed where the voltage model has a minimum accuracy.

## 2.6.5 Modified Integrator for the Voltage Model of the Flux observer

In [15], the author proposes a modified integrator for the voltage model of the flux observer for induction machines. As explained by him many authors, voltage model-based flux observers have an open loop pole. Integrator Drift problems occur due to low frequency and DC quantities. The author suggests adding a high pass filter in series to the pure integrator, and to compensate the steady state error produced by the integrator with multiplying the input signal of the integrator by the inverse of the high-pass filter.

This modification results on a low pass filter like solution. At the same time, the LPF is amplified by a time constant. The author expresses that if this time constant is made function of the angular frequency of the flux  $w$ .

$$\text{timeconstant} = \frac{1}{K_o(W_r)} \quad (71)$$

The LPF can be written in its derivative form as:

$$\frac{1}{K_o} \frac{d\lambda_{dqs}^s}{dt} + \lambda_{dqs}^s VM = \frac{1 - j \operatorname{sign}(w)}{K_o} (V_{dqs}^s + R_s I_{dqs}^s) \quad (72)$$

Alternatively, in its integral form as:

$$\lambda_{dqs}^s VM = \int (1 - j K_0 \operatorname{sign}(w)) * (V_{dqs}^s + R_s I_{dqs}^s) dt - \int k_o \lambda_{dqs}^s VM dt \quad (73)$$

The  $K_o$  constant can be selected in a range between 0.1 and 0.5. A value of  $K_o$  equal to zero would reduce the system to the original pure integrator.

The system open loop voltage model-based estimator results on the following system:

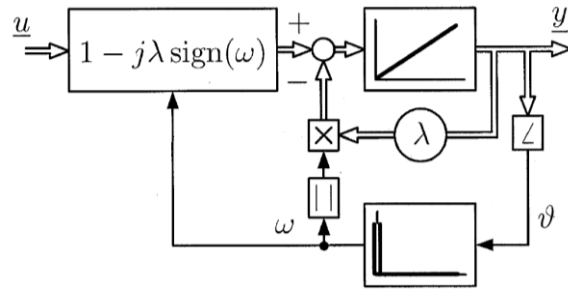


**Figure 19 Modified Integrator Voltage Model based Open loop Flux linkage Observer for IM.** This solution avoids the integrator drift-problem by the implementation of a DC filter without phase distortion.

It is important to notice the following respect this kind of solutions:

In a Gopinath-style flux observer the PI controller compensates the DC components of the voltage model.

At low speeds matching the output with the current model. Moreover, at high speeds the controller has no effect on the output. Nevertheless, the bandwidth of the controller allows it to act at low frequency. This effect removes the DC components and therefore a system with an open loop integrator is possible.

Therefore, this type of improvements does not enhance the system but add distortion to the output.

### 2.6.6 The center Point Correction method for the flux linkage Voltage Model.

[16] Focuses on the problem of the inaccuracy of the flux linkage voltage model estimation in open loop. The author proposes a stabilization method to avoid the need of the current model or an LPF that overcomes the instability of the voltage model-based estimator. The author calls his solution the center Point Correction method.

Since the flux linkage in direct torque control drives forms an almost circular path. Which allows the observation of the error on the real flux to be detected if the stator phase currents have a DC component.

If the machine saturates the phase currents become sinusoidal and the DC components are difficult to measure. Therefore, an alternative method is used based on the scalar product of the estimated flux linkage and the direction of the estimated flux linkage.

An error Signal is constructed as:

$$Err = \lambda_{dqs} * I_{dqs} - F_{LPF}(\lambda_{dqs} * I_{dqs}) \quad (74)$$

Where  $F_{LPF}()$  represents the application of an LPF to a certain component. Then the estimated flux linkage can be then corrected as:

$$\lambda_{dqs}(k + 1) = (1 + K_y Err)\lambda_{dqs}(k) = \quad (75)$$

Where  $K_y$  is the correction gain. Its implementation is shown in the following figure:

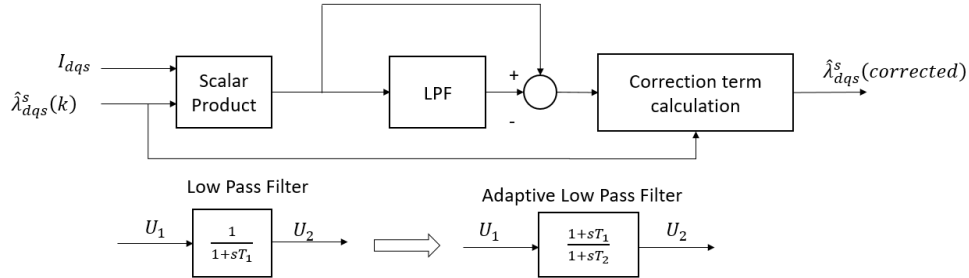


**Figure 20 Center Point Correction Method by [16]. Presents a Modified Integrator Voltage Model based Open loop Flux linkage Observer for IM based on a LPF and a Frequency Response Correction.**

Finally, the solutions dynamic response is enhanced by using an adaptive LPF. Where a short time period can be assumed, and the equation can be written in a difference equation form:

$$U_2(k + 1) = U_2(k) + \frac{\Delta t}{T_1} (U_{1(k)} - U_{2(k)}) + \frac{T_2}{T_1} (U_{1(k)} - U_{2(k)}) \quad (76)$$

Where T1 and T2 are the time constants and if kt is defined as:

$$kt = \frac{T_2}{T_1} \quad (77)$$

The implementation of the adaptive filtering can be made as:

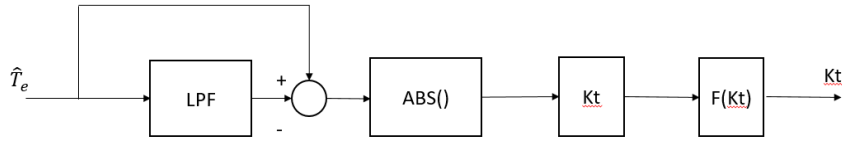


**Figure 21 Center Point Method Adaptive Filter Implementation by [16]. Presents a Modified Integrator Voltage Model based Open loop Flux linkage Observer for IM based on an adaptive LPF and a Frequency Response Correction.**

Where:

$$F(K_t) = \min \{1, k_t(T_e - F_{LPF}(T_e))\} \quad (78)$$

Finally, it is important to conclude that this paper detects the error in the flux linkage estimator based on the scalar product of the estimated stator flux linkage and the measured stator current.

#### 2.6.7 IDRIS AND YATIM “An improved stator flux linkage estimation”

The method described at [17] is proposed as an improvement of the flux linkage estimator based on the voltage model only. The improvement focuses on compensating the lag produced by the LPF modification to the voltage model open loop integrator.

The concept is based on a comparison between the frequency domain LPF equation and pure integrator equation. Operated in such a way that the system frequency  $W_e$  and the LPF corner frequency  $W_c$  are related as:

$$\frac{\lambda'}{\lambda} \angle \theta' - \theta = \frac{W_e}{\sqrt{W_e^2 + W_c^2}} \angle \phi \quad (79)$$

Where:

$$\phi = \frac{\pi}{2} - \tan^{-1}\left(\frac{W_e}{W_c}\right) \quad (80)$$

Equation (79) represents the ratio between the real and the modified response by the LPF, and its phase difference.

The d and q axis of the stator flux linkage are compensated at all frequencies but kept the same at the original frequency so that:

$$\lambda_{dqs}^s = \begin{cases} \frac{V_{dqs} - R_s I_{dqs}}{S}, & \text{for } W = W_e \\ \frac{V_{dqs} - R_s I_{dqs}}{S + W_c}, & \text{for } W \neq W_e \end{cases} \quad (81)$$

The proposed solution leads to the following flux linkage estimator diagram:

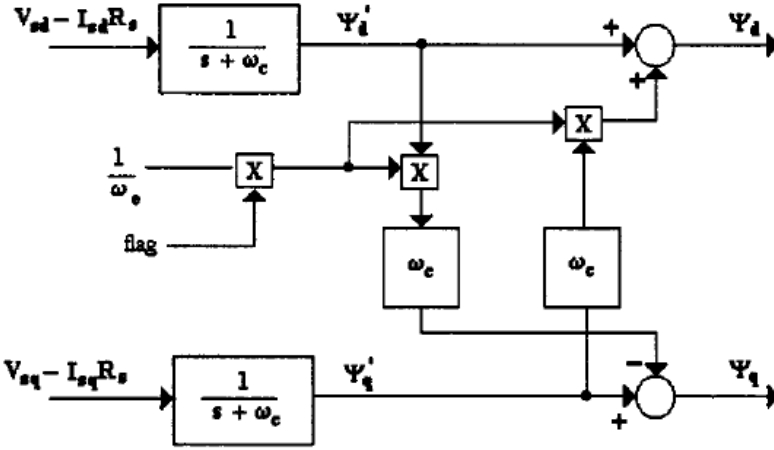


**Figure 22 Open Loop VM modification by Idris and Yatim [17].** Presents an additional path that cancels the Filter Distortion at SS.

The flag is activated either manually or by analyzing the steady state speed.

The flux linkages are then modified in the following way when the flag is active:

$$\lambda_{qs}^s = \begin{cases} \frac{\lambda_{qs}' W_c}{W_e} + \lambda_{ds}' \\ -\frac{\lambda_{ds}' W_c}{W_e} + \lambda_{qs}' \end{cases} \quad (82)$$

It is important to notice that this solution improves only the steady state of the drive.

## 2.6.8 The Observer Characteristic Function Method

On this section, the work of [18] , which focuses on how to improve the transition of the voltage model to the current model for IM Gopinath-Style flux linkage observer, is presented. In the transition

zone a phase distortion occurs as expressed previously in section 2.5 with bode diagrams and transfer functions. This distortion can also be represented in a vector form as:

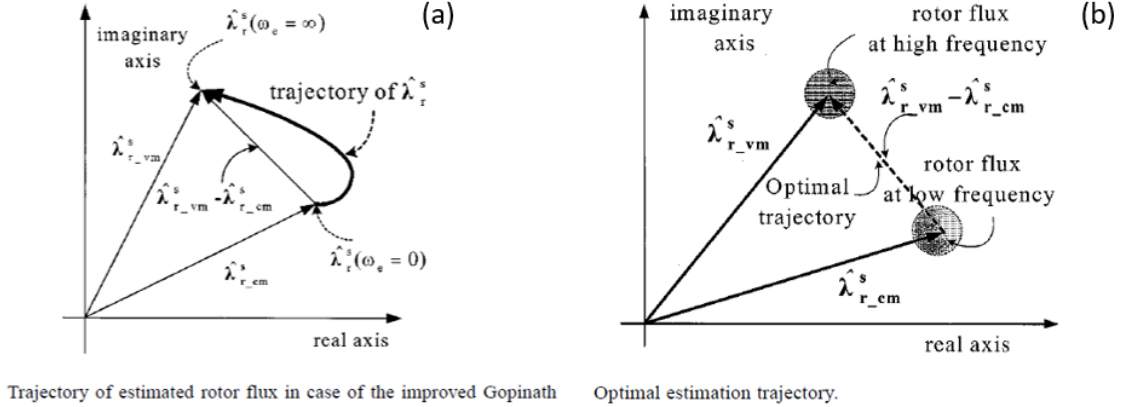


**Figure 23 Trajectory of the transition between the VM and CM in a Gopinath-style flux linkage estimator for induction machines [18]**

The analysis is based on the term A of the equivalent to equation (51) of the flux linkage observer in section 2.5.2 made for the IM Observer. It is important to note that the term is Equal in both models.

A can be written in the frequency domain as and operated by making  $s = jW_e$  to obtain:

$$A = \frac{s^2}{s^2 + K_p * s + K_i} = \frac{W_e^2}{\sqrt{(K_i - W_e^2)^2 + (K_p W_e)^2}} * e^{j\alpha} \quad (83)$$

Where:

$$\alpha = (\pi - \tan^{-1}\left(\frac{K_p W_e}{K_i - W_e^2}\right)) \quad (84)$$

The term  $\alpha$  represents the angle distortion suffered at the transition of the model.

In order to compensate this angle difference in the complex plane, a modification to the controller block diagram is purposed as following:

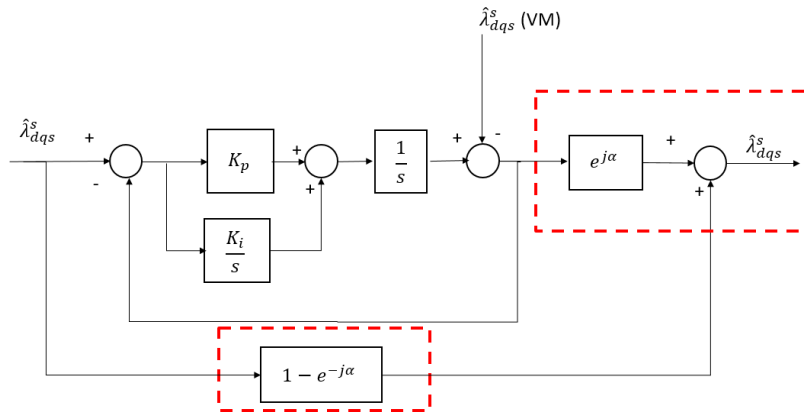


**Figure 24 Gopinath-style flux observer tuning path in Laplace domain with correction according to The Observer Characteristic Function Method by [18].**

This modification produces the term A analyzed before to be modified as:

$$A = \frac{W_e^2}{\sqrt{(K_i - W_e)^2 + (K_p W_e)^2}} * e^{j0} \quad (85)$$

Which is a pure real axis response and a response with no angle distortion.

## 2.7 Conclusions:

The State of the Art has been carefully examined from the literature it is possible to detect 2 key areas for improvements:

- The transition between the models in the State-of-the-Art observer can be improved as suggested by [18].
- The parameter dependency can be corrected by coupling the Current and Flux Observers as suggested by [11].
- An uncovered topic by the literature is the distortion caused by the iron losses. This open issue can also be addressed.
- The methods concerning the rejection of DC quantities in the voltage model do not apply to the Gopinath-Style Observer since the PI controller rejects the DC quantities and therefore a pure integrator is used.



# Chapter Three

## 3 Implementing the Observer Characteristic Function Method for IPMSM Gopinath-Style Observer

Chapter structure:

First, The Observer Characteristic Function Method proposed by [18] was used to analyze the case of the Gopinath-style flux observer for IPMSM.

Second, a Frequency Response Corrected Observer is implemented in simulation and compared with the State-of-the-Art Observer. the results are presented and analyzed.

Thirdly, the parameter sensitivity of the FRC observer is compared to the SOA observer. the torque production is analyzed and the machine dynamics.

The review is then assessed in answer to the requirements of the application under study.

As explain earlier this method seeks to enhance the transition between the models by correcting the distortion produced by the controller in the system.

### 3.1.1 Theoretical development for IPMSM observer:

We can express the Gopinath-style flux observer for IPMSM as in the following figure:

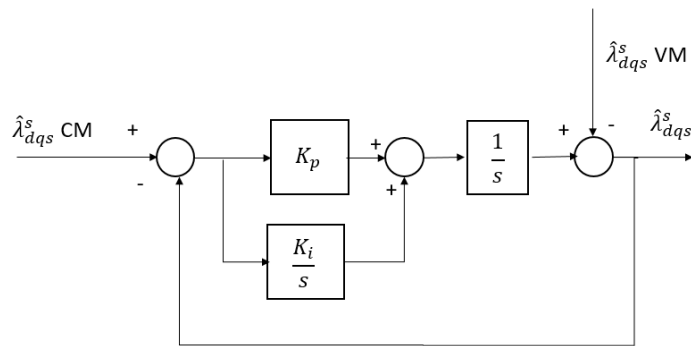


Figure 25 Flux Linkage estimator Control Tuning Path [4]. The VM is operated so that  $\lambda_{dqs}$  path is the only output.

In addition, its equivalent transfer function can be expressed as:

$$\hat{\lambda}_{dqs}^s = A * \hat{\lambda}_{dqs}^s VM + B * \hat{\lambda}_{dqs}^s CM \quad (86)$$

Where:

$$A = \frac{s^2}{s^2 + K_p * s + K_i} \quad (87)$$

$$B = \frac{K_p * s + K_i}{s^2 + K_p * s + K_i} \quad (88)$$

In addition, the following relationship exists:

$$A + B = 1 \quad (89)$$

And is used to rearrange the equation (51) as a function of the factor A:

$$\hat{\lambda}_{dqs}^s = A \hat{\lambda}_{dqs}^s VM + (1 - A) \hat{\lambda}_{dqs}^s CM \quad (90)$$

Since both the voltage model and the current model of the flux observer are dependent on this term, the distortion of this term can be analyzed and corrected. In order to understand the distortion, recalling bode diagram of Figure 13;**Error! No se encuentra el origen de la referencia.** in the previous section, at low speeds not only attenuation occurs but as the model increases its frequency, the phase of the signal changes.

From the transfer function of A, the frequency response analysis as proposed by [18].

For that, the Laplace operators are replaced  $s$  by  $j W$  so that from equation (52) the following expression can be obtained:

$$A = \frac{w^2}{\sqrt{(K_i - w^2)^2 - w^2 K_p^2}} * e^{j\alpha} \quad (91)$$

Where:

$$\alpha = \pi - \text{atan}\left(\frac{b}{a}\right) \quad (92)$$

The demonstration of this equation is performed in the Appendix section “Frequency Response Correction Factor Demonstration”

By looking at equation (91);**Error! No se encuentra el origen de la referencia.**, the response of the flux observer depends on the magnitude on the left side term and the phase depends on the angle. The response to this distortion is equal to the one found for the Gopinath-style flux linkage observer for IM found by [18].

Now the phase distortion of the PI controller can be corrected. To do so a correction is implemented as:

$$A' = \frac{w^2}{\sqrt{(K_i - w^2)^2 - w^2 K_p^2}} * e^{j\alpha} * e^{-j\alpha} = \frac{w^2}{\sqrt{(K_i - w^2)^2 - w^2 K_p^2}} \quad (93)$$

Where A' has a pure real response. In the same way, B can be corrected as:

$$B' = 1 - A' \quad (94)$$

A block diagram of the proposed system is presented in Figure 25:

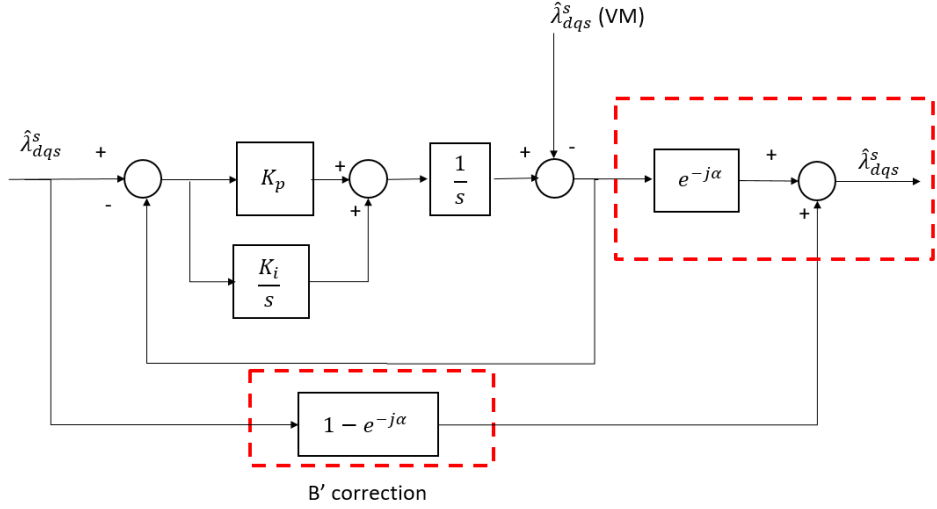


**Figure 26 Gopinath-style flux observer tuning path in Laplace domain with correction according to The Observer Characteristic Function Method. (Red) Both correction Terms introduced in the observer.**

The correction factor introduced can be further analyzed as function of A' if the equivalent transfer function of the new system is expressed as:

$$\hat{\lambda}_{dqs}^s = (A \hat{\lambda}_{dqs}^s VM + (1 - A) \hat{\lambda}_{dqs}^s CM) e^{-j\alpha} + (1 - e^{-j\alpha}) \hat{\lambda}_{dqs}^s CM \quad (95)$$

If this expression is operated:

$$\hat{\lambda}_{dqs}^s = A' \hat{\lambda}_{dqs}^s VM + e^{-j\alpha} \hat{\lambda}_{dqs}^s CM - A' \hat{\lambda}_{dqs}^s CM + \hat{\lambda}_{dqs}^s CM - e^{-j\alpha} \hat{\lambda}_{dqs}^s CM \quad (96)$$

Moreover, after canceling the equivalent terms the expression becomes:

$$\hat{\lambda}_{dqs}^s = A' \hat{\lambda}_{dqs}^s VM + (1 - A') \hat{\lambda}_{dqs}^s CM \quad (97)$$

### 3.1.2 Solution Implementation:

In order to implement this solution, it is assumed that the system frequency is equal to the one measured in the system:

Therefore, the following block diagram can be proposed for the parts A' correction and B' correction of Figure 26.

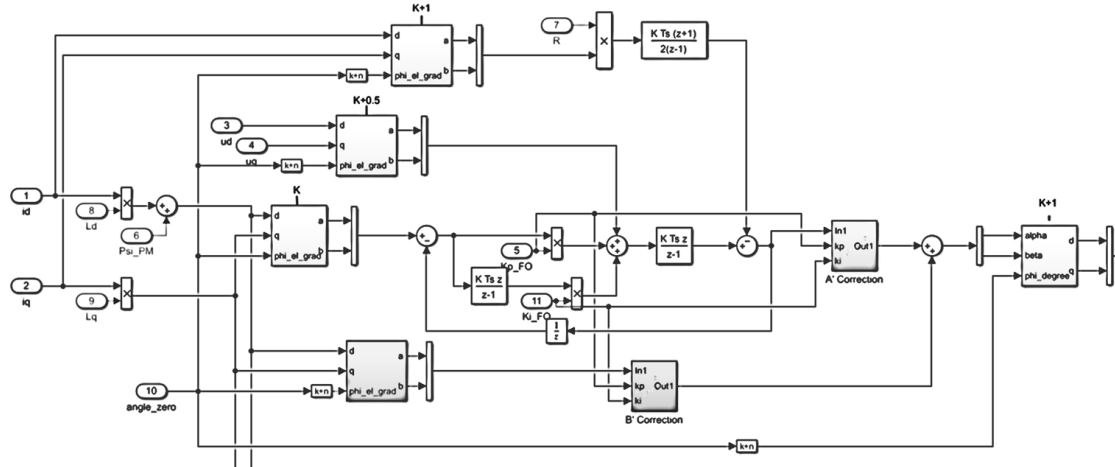


Figure 27 Simulink Implementation of A' and B' correction factors. In blue the angle correction for B' correction factor. (In darker gray) B' correction factor and (in light gray) the A' correction factor.

Where the correction factors subsystems are implemented as:

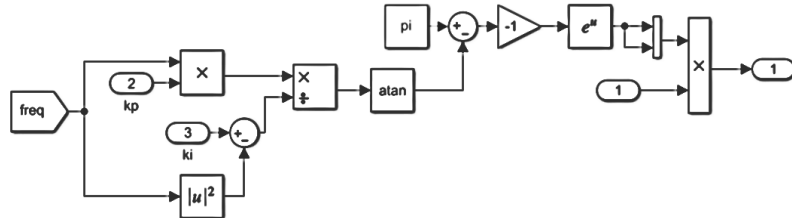
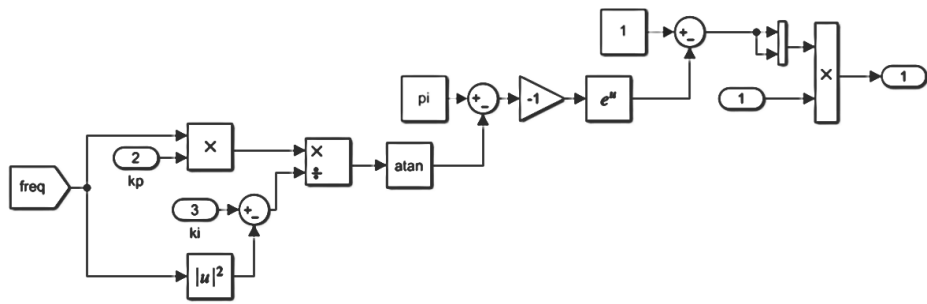
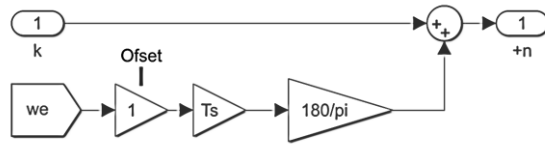


Figure 28 A' Correction Factor Subsystem. (Inputs) the frequency, and the controller gains that multiply the Flux linkage of the voltage model entering at (1).



**Figure 29 B' Correction Factor Subsystem.** (Inputs) the frequency, and the controller gains that multiply the Flux linkage of the current model entering at (1).

Note that in order to implement the B' correction factor , the signal in discrete time domain has to be in the sampling instant  $k+1$ , so it is necessary to apply an offset. To do so the speed at a sampling instant  $T_s$  is assumed constant in one switching period, and a correction factor is implemented as following:



**Figure 30 Offset angle for B' correction factor.** Shows the required Angle Offset for the CM flux linkage in order to calculate the correction factor.

### 3.1.3 Simulation results and Models Benchmarking:

In this section, the simulation results of the frequency response corrected observer are compared with the State-of-the-art observer. Both solutions were modeled in a DB-DTFC drive simulation with

In order to do so, the following acronyms are used for the figures:

- SOA for simulations using “State of the Art” Gopinath Style Flux Observer.
- FRC for simulations using the “Frequency Response Correction” proposed for the Gopinath Style Flux Observer.

The described system was tested under a speed ramp 0 to 17 000 Rpm at maximum torque (450 Nm) in the constant region. The results were the compared with the state of art observer

### 3.1.3.1 Flux linkage magnitude estimation with SOA and FRC observers

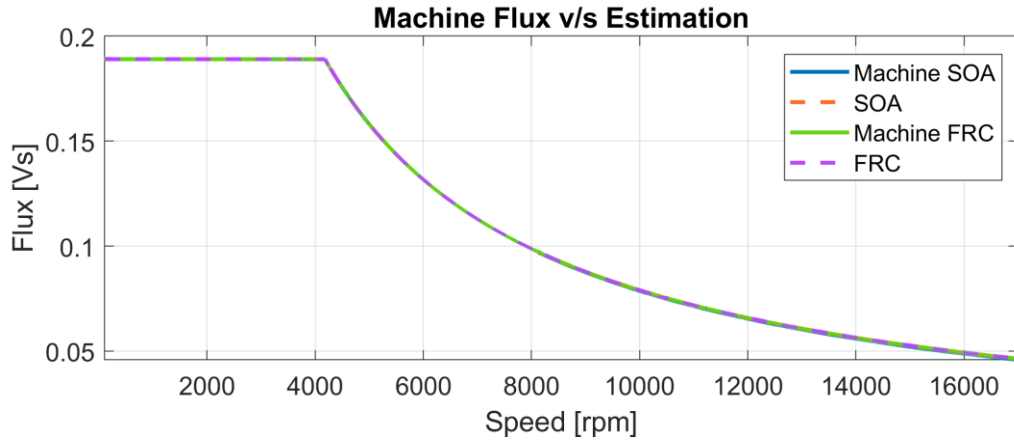


Figure 31 Simulation results of the Estimated Flux with the SOA and FRC Observers in CL implementation. The torque command is 450 Nm the MTPA Flux command is based on a LUT and the speed is increasing with time at a constant rate.

From the outside perspective, the difference between the models is not apparent. Both implementations have a high accuracy.

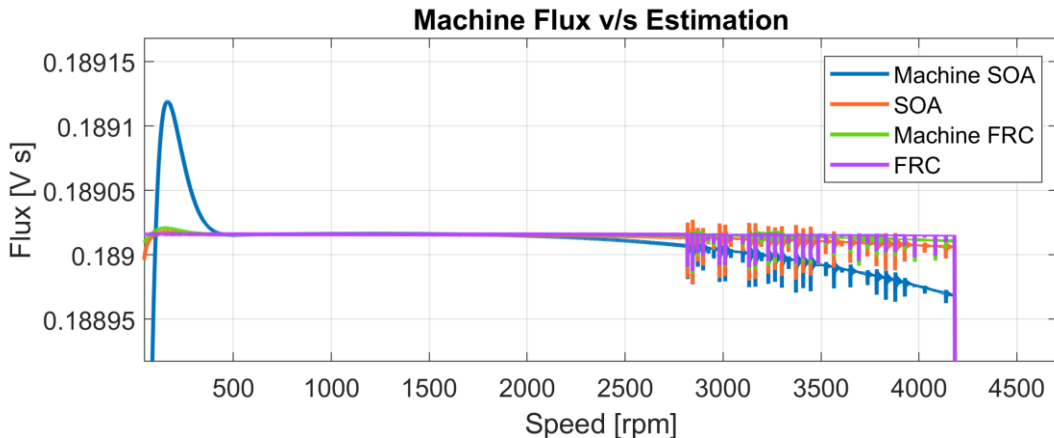
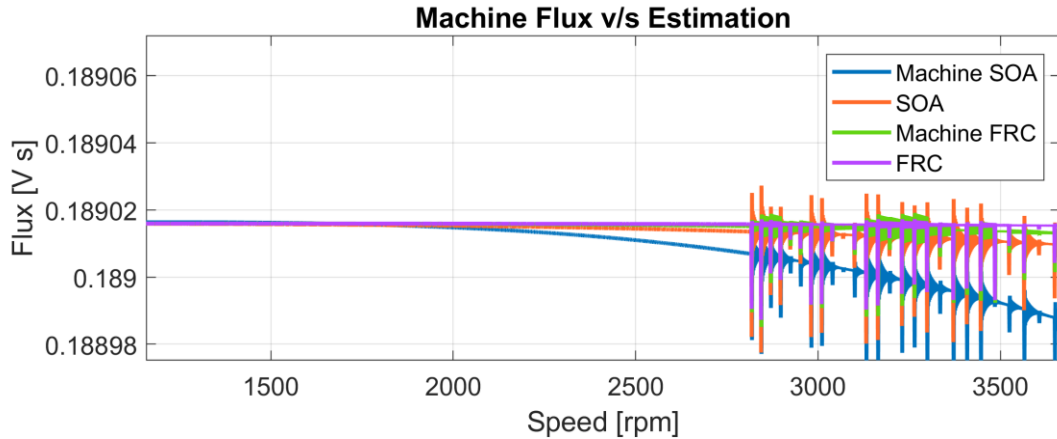


Figure 32 Machine flux vs estimation Zoom into the constant torque region. (Blue) Machine SOA Flux, (Orange) Estimated flux with SOA Observer. (Green) Machine FRC Flux, (Purple) Estimated flux with FRC Observer.

In Figure 33, the overshoot in the machine flux at the beginning is smaller in the FRC. Also, the flux production of the machine is better under the FRC observer. Least estimation error is therefore expected in this region for the FRC observer.



**Figure 34** Machine flux vs estimation Zoom into the model transition area. (Blue) Machine SOA Flux, (Orange) Estimated flux with SOA Observer. (Green) Machine FRC Flux, (Purple) Estimated flux with FRC Observer.

In the Transition area, a reduction of the flux is notable in the SOA observer, but this is no longer the case under FRC observer.

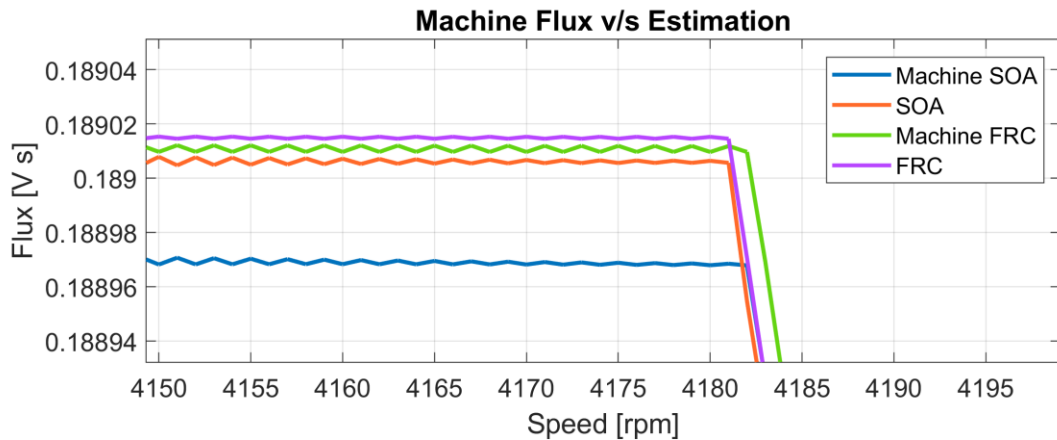


**Figure 35** Machine flux vs estimation Zoom Difference at current limits. (Blue) Machine SOA Flux, (Orange) Estimated flux with SOA Observer. (Green) Machine FRC Flux, (Purple) Estimated flux with FRC Observer.

At 4180 RPM the current limits of the machine are reached, here the estimation error is similar in both observers. An increasing error over speed begins to be parent in the SOA observer.

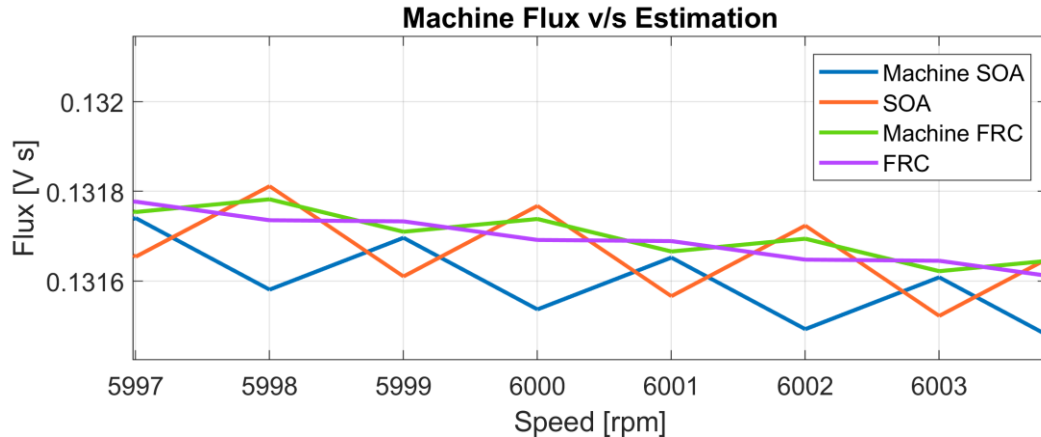


Figure 36 Machine flux vs estimation Zoom at 6000 RPM. (Blue) Machine SOA Flux, (Orange) Estimated flux with SOA Observer. (Green) Machine FRC Flux, (Purple) Estimated flux with FRC Observer.

At 6000 rpm the ripple in the flux for the SOA observer is bigger than the one on the FRC observer. The flux estimation error in this area is smaller as well.

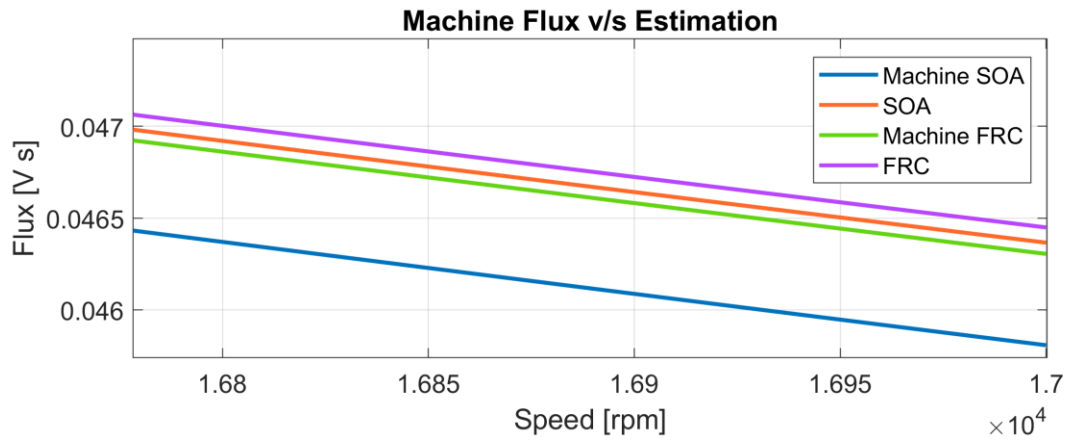
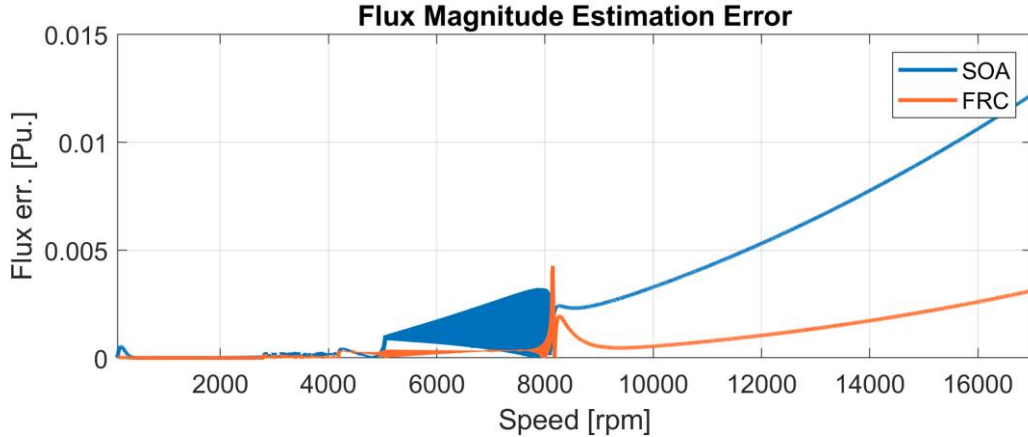
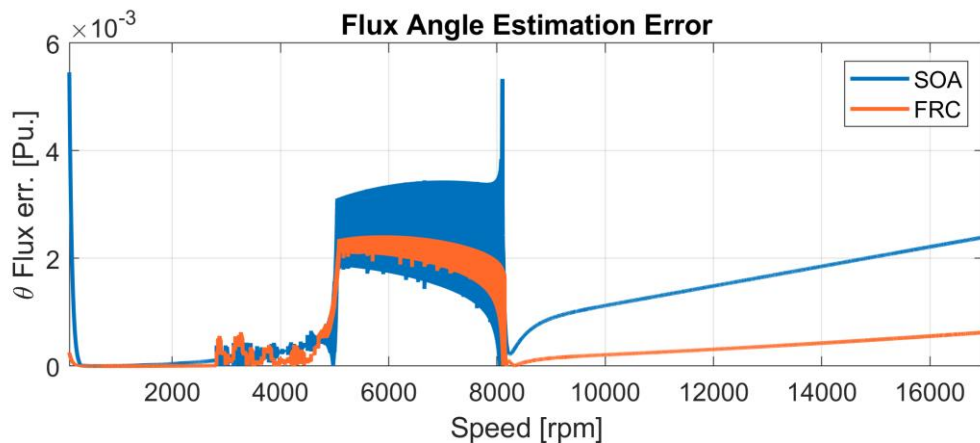


Figure 37 Machine flux vs estimation Zoom at high speed range 15 000 RPM to 17 000 RPM. (Blue) Machine SOA Flux, (Orange) Estimated flux with SOA Observer. (Green) Machine FRC Flux, (Purple) Estimated flux with FRC Observer.

At high speed, the model difference is notable, the FRC observer has a much smaller deviation compared with the SOA Observer.



**Figure 38** Flux Magnitude Estimation Error. (Blue) absolute flux magnitude error form the SOA Observer. (Orange) absolute flux magnitude error form the FRC Observer.



**Figure 39** Absolute Flux Angle Estimation Error. (Blue) absolute flux angle error form the SOA Observer. (Orange) absolute flux angle error form the FRC Observer.

From the Figure 38 it is possible to see that the error at high speed is smaller for the FRC Observer, it is also possible to see that the transition area magnitude is less distorted. From Figure 39 it is possible to see that the angle error in the current limit region is still present. Like the previous figure, the flux angle error is smaller in the FRC observer results.

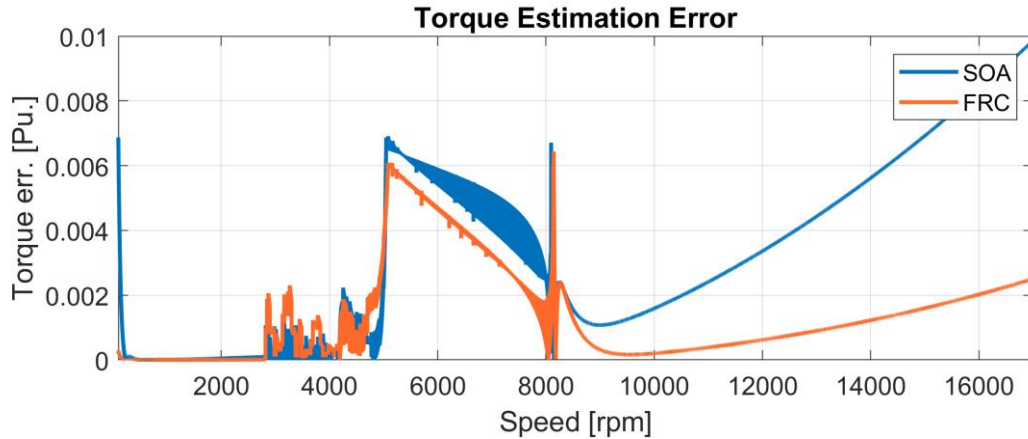


**Figure 40 Torque Estimation Error for SOA and FRC Observers.** (Blue) absolute torque error form the SOA Observer. (Orange) absolute torque error form the FRC Observer.

Both observers can estimate the torque with errors under 1% nevertheless, the FRC observer produces an error of 0.2% at 17000 rpm compared with the SOA observer.

### 3.1.3.1.1 Conclusions:

- At the constant torque region, the distortion of the FRC is smaller than the SOA model; nevertheless, noise is still present in both models.
- The transition of the FRC is less distorted than the SOA in magnitude.
- At the current limit, the models behave similar.
- At 6000 RPM, the SOA error increases while the FRC is kept constant.
- At 16 000 RPM the error of the SOA is another order of magnitude bigger than the FRC

### 3.1.4 Parameter Sensitivity Analysis

In the following section parameter sensitivity analysis at 12 000 RPM is performed. The inductances in the d-axis and q-axis are stressed as well as the Permanent Magnet Flux and the Stator Resistances. Bidirectional deviations of 10% are applied and studied.

Four Key Indicators are used in the analysis, the Absolute Flux Magnitude error, the Flux Angle error and the Torque Estimation error.

### 3.1.4.1 Sensitivity to a 10% deviation of $L_d$ at 12 000 RPM

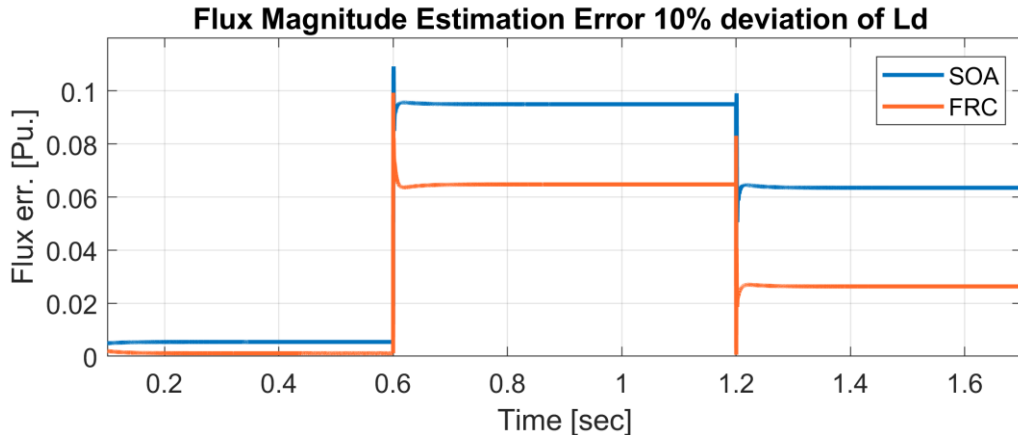


Figure 41 Flux Magnitude Deviation SOA and FRC observers under a 10% deviation of  $L_d$ . (Blue) absolute flux magnitude error form the SOA Observer. (Orange) absolute flux magnitude error form the FRC Observer.

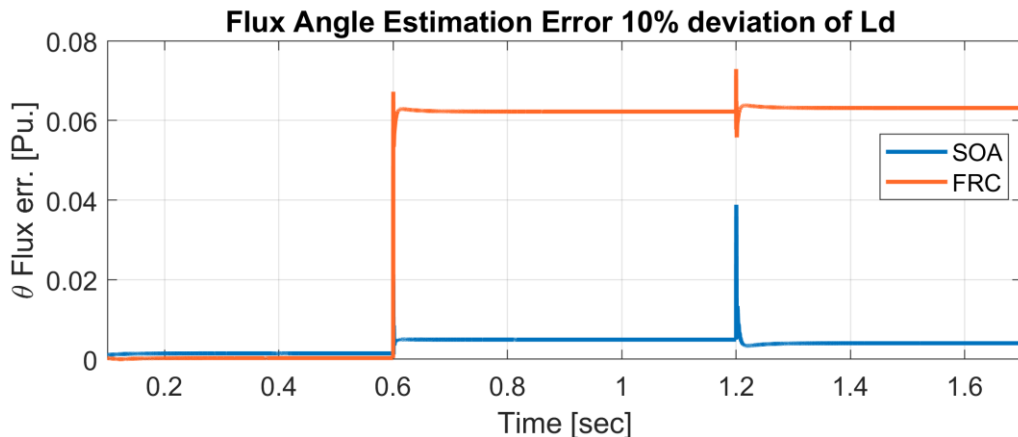


Figure 42 Flux Angle Deviation SOA and FRC observers under a 10% deviation of  $L_d$ . (Blue) absolute flux angle error form the SOA Observer. (Orange) absolute flux angle error form the FRC Observer.

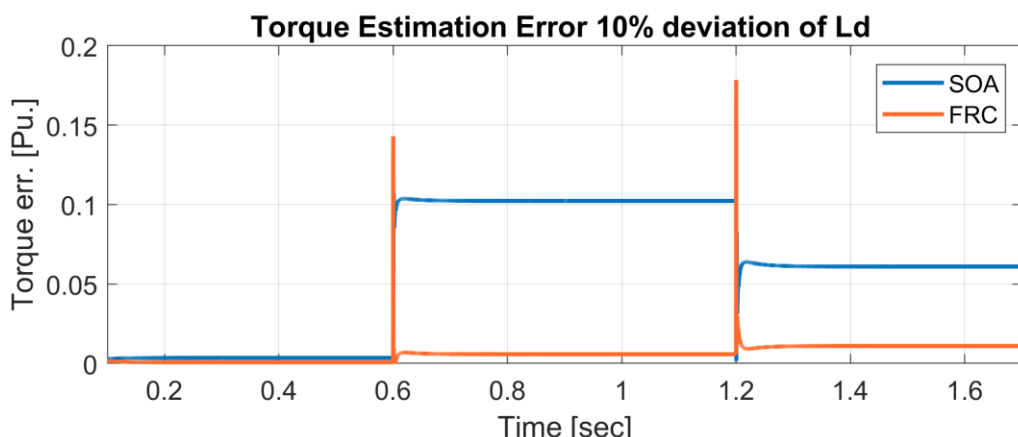


Figure 43 Torque Magnitude Deviation SOA and FRC observers under a 10% deviation of  $L_d$ . (Blue) absolute torque error form the SOA Observer. (Orange) absolute torque error form the FRC Observer.

If a 10% Ld deviation is applied to the model at maximum torque and 12000 RPM and the Steady State is analyzed.

### Conclusions:

- The magnitude error of the flux estimation of the FRC model is around 5% and the error of the SOA model is around 9%
- The torque magnitude error of the FRC is around 4% while the error of the SOA is around 10%
- However, the angle error of the SOA is around 2% but the Angle error of the FRC is around 11% off.

The FRC model estimation magnitudes are less sensitive to d axis inductance parameter deviation in magnitude but more sensitive in angle distortion.

#### 3.1.4.2 Sensitivity to a 10% deviation of Lq at 12 000 RPM

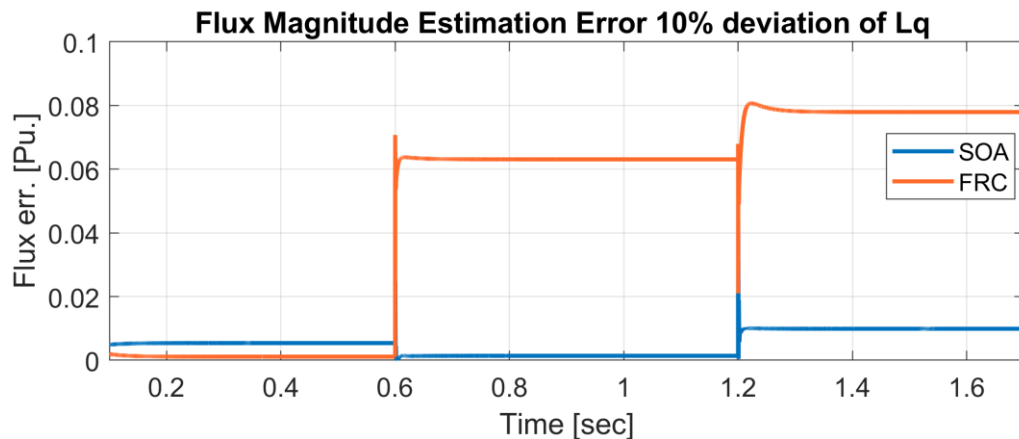
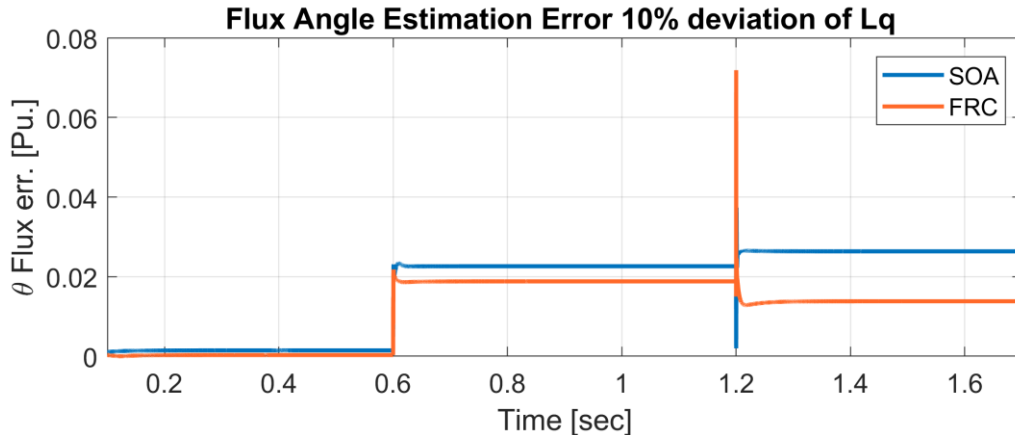
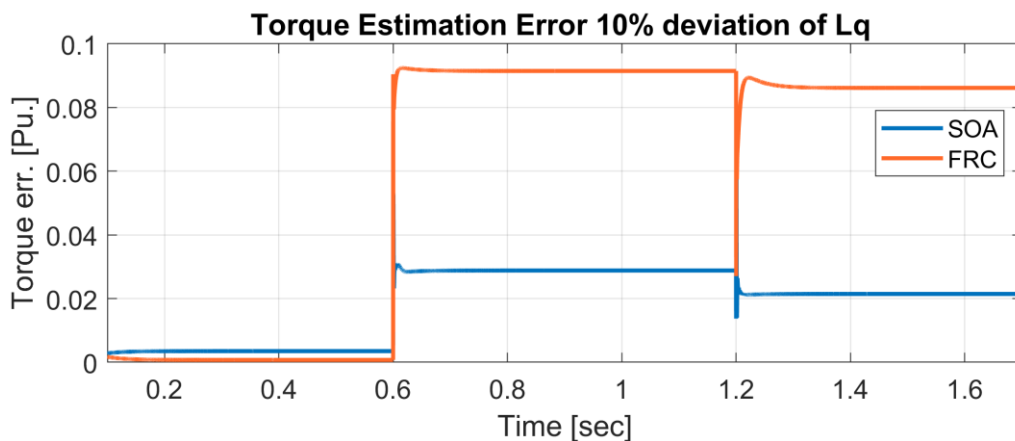


Figure 44 Flux Magnitude Deviation SOA and FRC observers under a 10% deviation of Lq. (Blue) absolute flux magnitude error form the SOA Observer. (Orange) absolute flux magnitude error form the FRC Observer.



**Figure 45** Flux Angle Deviation SOA and FRC observers under a 10% deviation of Lq. (Blue) absolute flux angle error form the SOA Observer. (Orange) absolute flux angle error form the FRC Observer.



**Figure 46** Torque deviation SOA and FRC observers under a 10% deviation of Lq. (Blue) absolute torque error form the SOA Observer. (Orange) absolute torque error form the FRC Observer.

If a 10% Lq deviation is applied to the model at maximum torque and 12000 RPM and the Steady State is analyzed.

### Conclusions:

- The flux magnitude error is around 1 % while the SOA does not have a notable variation.
- The angle error is smaller in the FRC, but the difference is around 1 % less.
- The torque magnitude error is of around 10% in the FRC while it is only of 3 % in the SOA

The results show an overall bigger resilience of the SOA observer respect to Lq parameter variation compared to the FRC.

### 3.1.4.3 Sensitivity to a 10% deviation of $\lambda_{pm}$ at 12 000 RPM

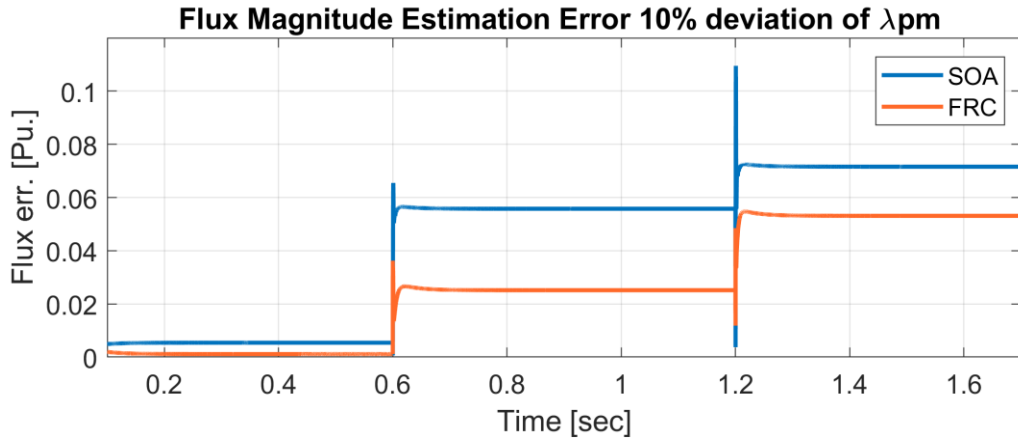


Figure 47 Flux Magnitude Deviation SOA and FRC observers under a 10% deviation of  $\lambda_{pm}$ . (Blue) absolute flux magnitude error form the SOA Observer. (Orange) absolute flux magnitude error form the FRC Observer.

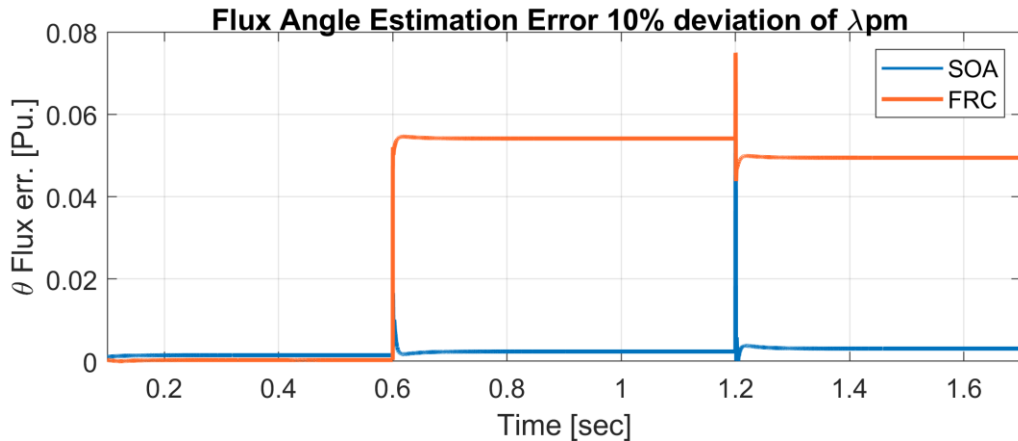


Figure 48 Flux Angle Deviation SOA and FRC observers under a 10% deviation of  $\lambda_{pm}$ . (Blue) absolute flux angle error form the SOA Observer. (Orange) absolute flux angle error form the FRC Observer.

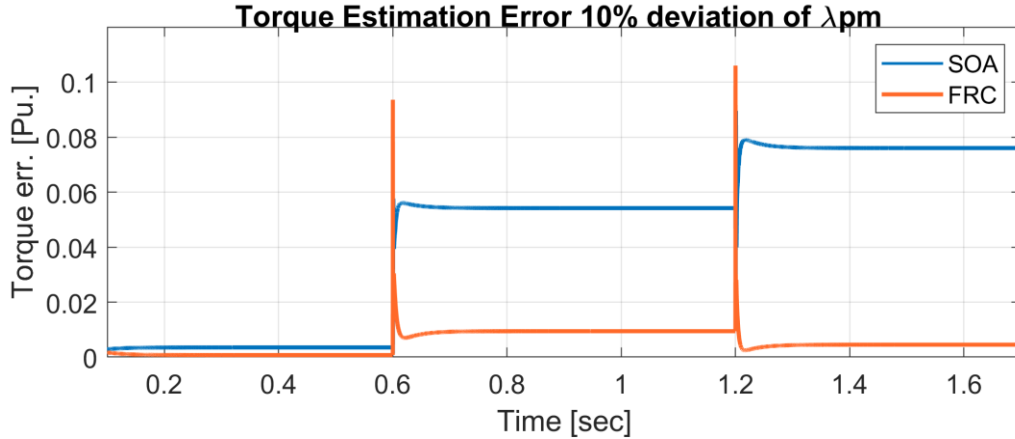


Figure 49 Torque Magnitude Deviation SOA and FRC observers under a 10% deviation of  $\lambda_{pm}$ . (Blue) absolute torque error form the SOA Observer. (Orange) absolute torque error form the FRC Observer.

In order to test the parameter sensitivity to  $\lambda_{pm}$  variations an increase of 10% is applied at 0.6 s and a decrease of 20% is applied at 1.2 seconds. See figure (d) above. The idea is to see the sensibility to over or under estimation of the parameter.

### Conclusions:

- The magnitude error is bigger in both scenarios in the State-of-the-Art Observer with a magnitude of up to 5% deviation compared with the 2% of the FRC observer.
- The angle error is bigger in the FRC with a magnitude close to 10%. The SOA observer shows an error of 1%
- The torque error of the overall estimation is smaller in the case of the FRC and the parameter sensitivity is symmetric, the deviation cause of adding or subtracting 10% of  $\lambda_{pm}$  is similar.

#### 3.1.4.4 Sensitivity to a 10% deviation of $R_s$ at 12 000 RPM

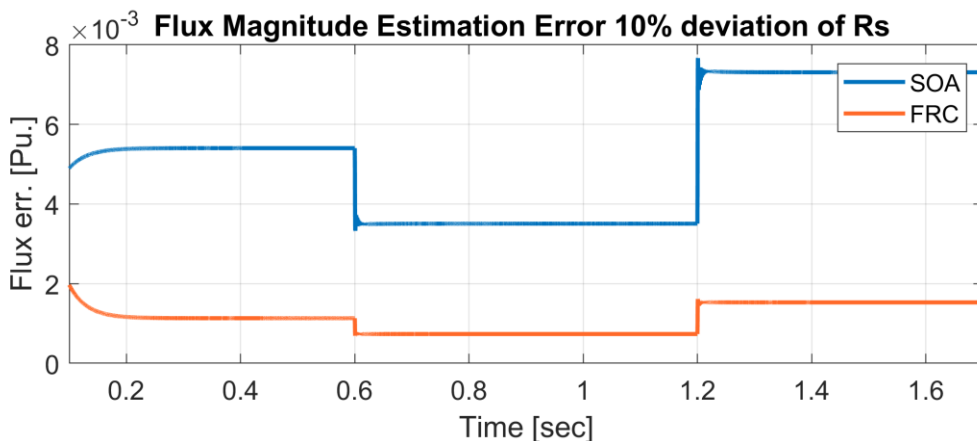


Figure 50 Flux Magnitude deviation SOA and FRC observers under a 10% deviation of  $R_s$ . (Blue) absolute flux magnitude error form the SOA Observer. (Orange) absolute flux magnitude error form the FRC Observer.

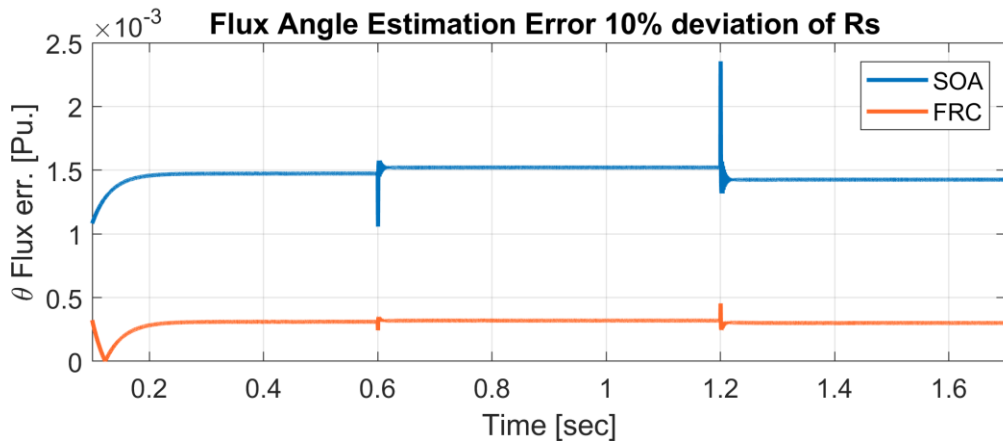


Figure 51 Flux Angle deviation SOA and FRC observers under a 10% deviation of  $R_s$ . (Blue) absolute flux angle error form the SOA Observer. (Orange) absolute flux angle error form the FRC Observer.

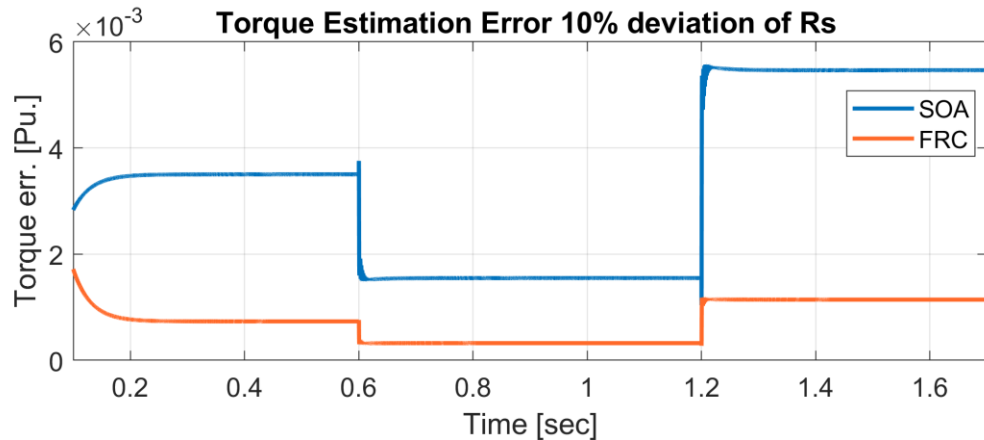


Figure 52 Torque Deviation SOA and FRC observers under a 10% deviation of  $R_s$ . (Blue) absolute torque error form the SOA Observer. (Orange) absolute torque error form the FRC Observer.

In this section, the results of a test of parameter sensitivity to  $R_s$  are presented. An increase of 10%  $R_s$  is applied at 0.6 s and a decrease of 20%  $R_s$  is applied at 1.2 seconds. See figure (d) above.

### Conclusions:

- The results show an overall improvement in this regard, the FRC has error is an order of magnitude smaller than the SOA.
- Estimation error for the flux under increase or decrease is symmetrical in both models

### 3.1.4.5 Conclusions:

A summary of the parameter sensitivity is presented in the following table:

**Table 2 Parameter Sensitivity Simulation Results Summary.** At the left side the SOA observer's response and at the right side the FRC Observer response. In each group the flux magnitude error, angle deviation and torque error under the variation of the par

Sensitivity test to Parameter Variation at 12000 [rpm]	SOA			FRC		
	$ \lambda $ err.	$\theta\lambda$ err.	$\Delta T_e$ err.	$ \lambda $ err.	$\theta\lambda$ err.	$\Delta T_e$ err.
+/- 10% Ld	9.0%	2.0%	10.0%	5.0%	11.0%	4.0%
+/- 10% Lq	0.1%	2.0%	3.0%	6.0%	2.0%	9.0%
+/- 10% $\lambda_{pm}$	5.5%	0.5%	6.0%	2.8%	5.2%	1.0%
+/- 10% Rs	0.0200%	0.0010%	0.0020%	0.0050%	0.0005%	0.0002%

- The FRC corrected observer has a higher dependency on the Current Model and therefore is more parameter sensitive than the SOA.
- If a parameter LUT is implemented in the system this problem might not be an issue since the most sensitive parameters like inductance and  $\lambda_{pm}$  are updated for each frequency and temperature.

## 3.1.5 Torque Step Response Benchmarking

### 3.1.5.1 Response at Low Speed 2000 RPM

In order to test the system response of the system the speed was fixed at 12000 rpm and the torque command was stepped at time 0.7 from 300 to 350 Nm and afterwards at 1.2 seconds, a negative step was applied, and the torque command was set to 250 Nm. The following figure provides a good overview of the experimental conditions:

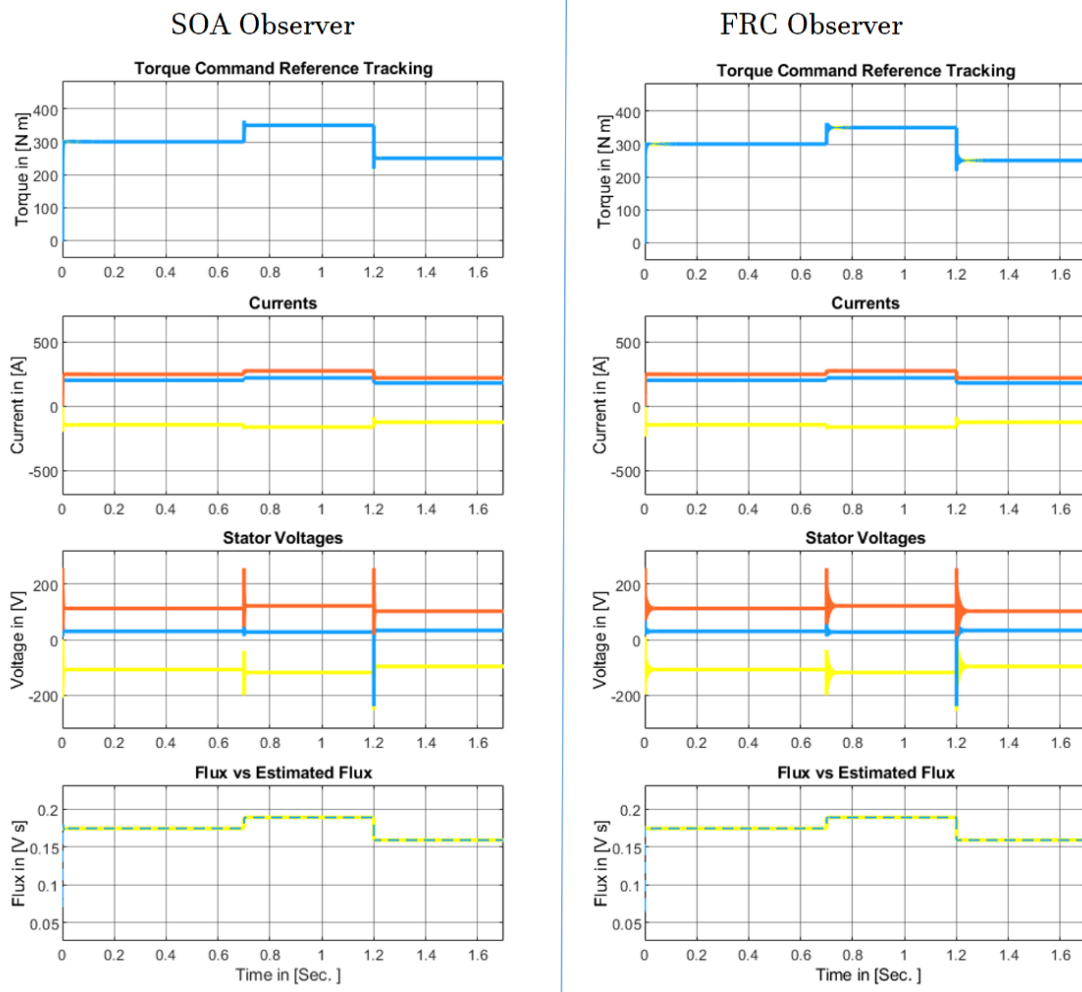


**Figure 53** Machine States with SOA (left) and FRC (right) Flux linkage Observers under Torque Test at low speeds. (Top) torque command in yellow and machine torque in blue. (Top middle)  $i_d$  in yellow,  $i_q$  in blue and  $i_{dq}$  in orange. (Bottom middle)  $U_d$  in yellow,  $U_q$  in blue and  $U_{dq}$  in orange, the last one is the module of the voltage signal. (Bottom) flux command in yellow and estimated flux in blue.

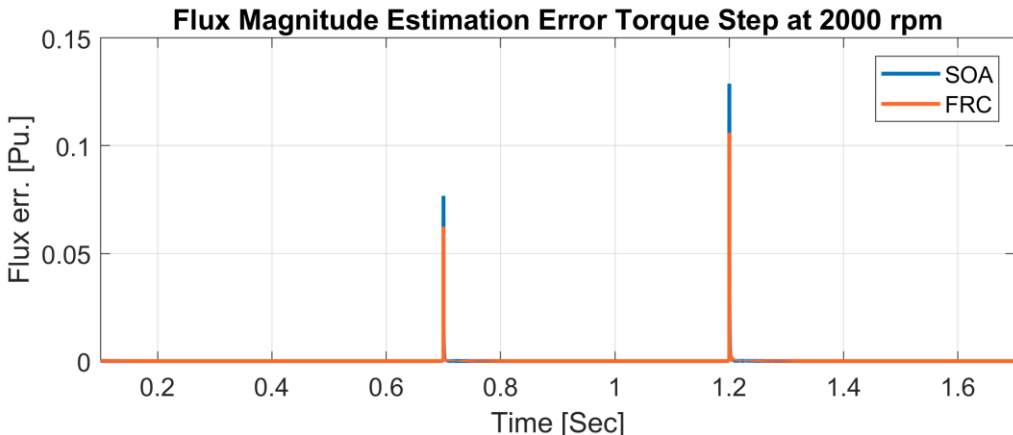


**Figure 54** Flux magnitude deviation, torque step response at 2000 rpm. (Blue) absolute flux magnitude error form the SOA Observer. (Orange) absolute flux magnitude error form the FRC Observer.

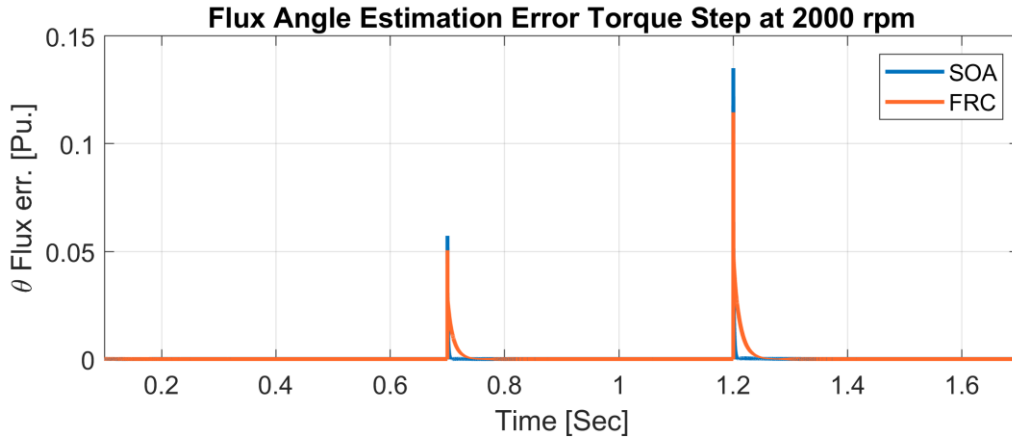


Figure 55 Flux angle deviation, torque step response at 2000 rpm. (Blue) absolute flux angle error form the SOA Observer. (Orange) absolute flux angle error form the FRC Observer.

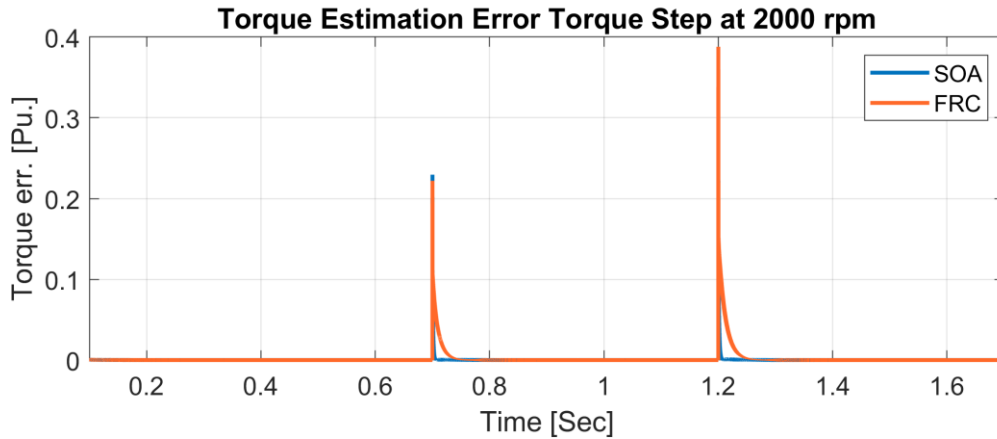


Figure 56 Torque deviation, torque step response at 2000 rpm. (Blue) absolute torque error form the SOA Observer. (Orange) absolute torque error form the FRC Observer.

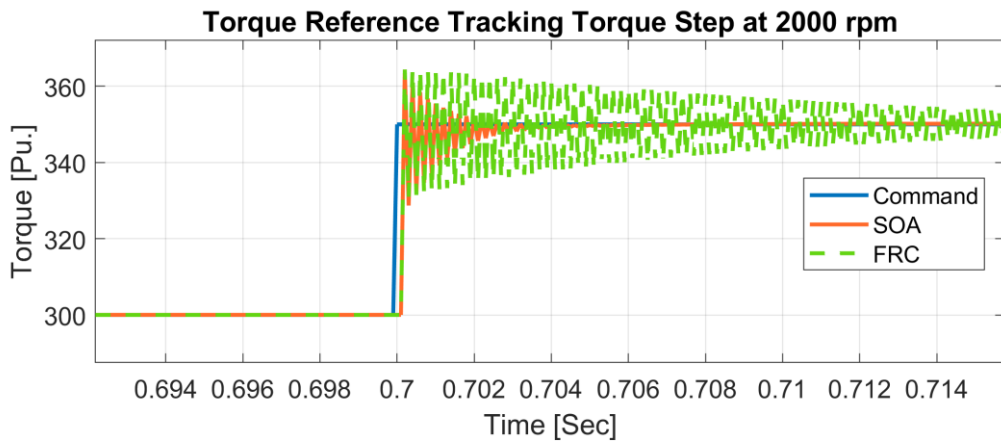


Figure 57 Reference tracking, torque step response at 2000 rpm. (Blue) Commanded Torque. (Orange) torque obtained by implementation of the SOA Observer. (Green) torque obtained by implementation of the FRC Observer.

Figure 57 shows the data analysis of the values obtained from simulation at  $t = 0.7$  Sec. Where a torque step is applied. The responses of both reduce the error quite significantly and are stable in Steady State.

### Conclusions:

- The magnitude error rejection capability of the FRC is higher than the one of the SOA.
- The angle error is corrected faster in the SOA, but the overshoot is bigger.
- The total torque error in both models is under 10% in less than three switching periods. Nevertheless, the total torque estimation error of the SOA has a Higher disturbance rejection capability.
- The torque reference oscillation at low speeds is higher than the one of the SOA.

#### 3.1.5.2 Response at high speed 12000 RPM

In order to test the system response of the system the speed was fixed at 12000 rpm and the torque command was stepped at time 0.7 from 100 to 150 Nm and afterwards at 1.2 seconds, a negative step was applied, and the torque command was set to 50 Nm.

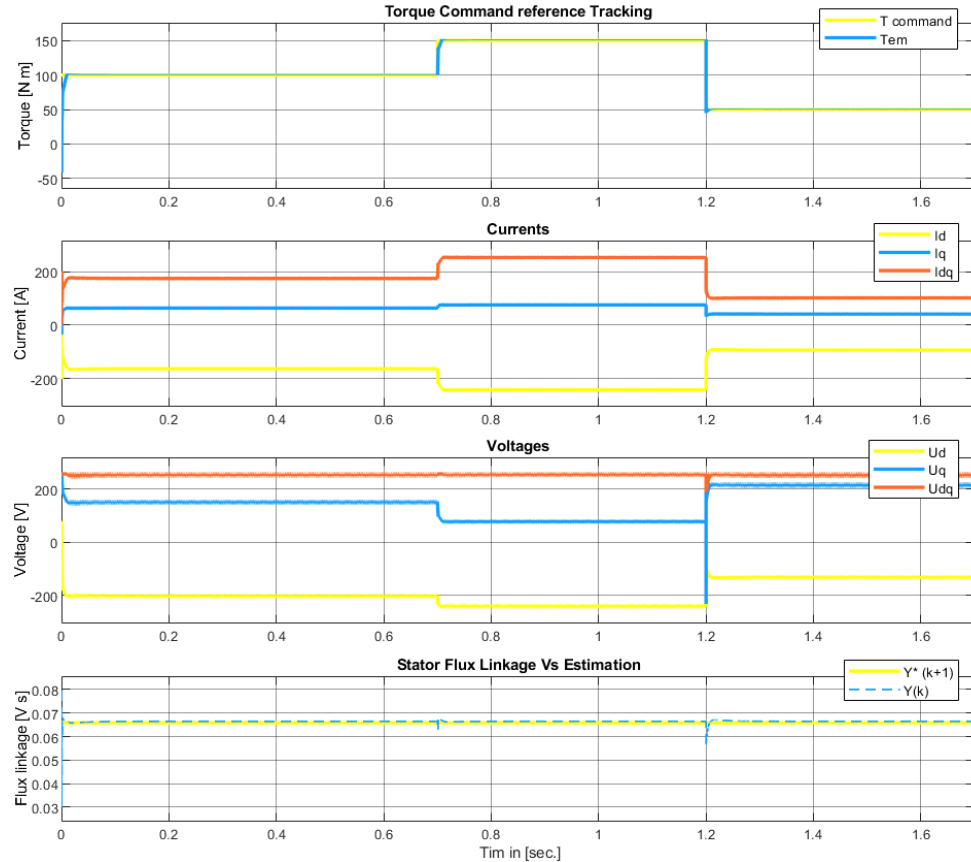


**Figure 58** Torque step test simulation at 12000 RPM for FRC Machine Status are displayed. (Top) torque command in yellow and machine torque in blue. (Top middle) id in yellow, iq in blue and idq in orange. (Bottom middle) Ud in yellow, Uq in blue and Udq in orange. (Bottom) flux command in yellow and estimated flux in blue.

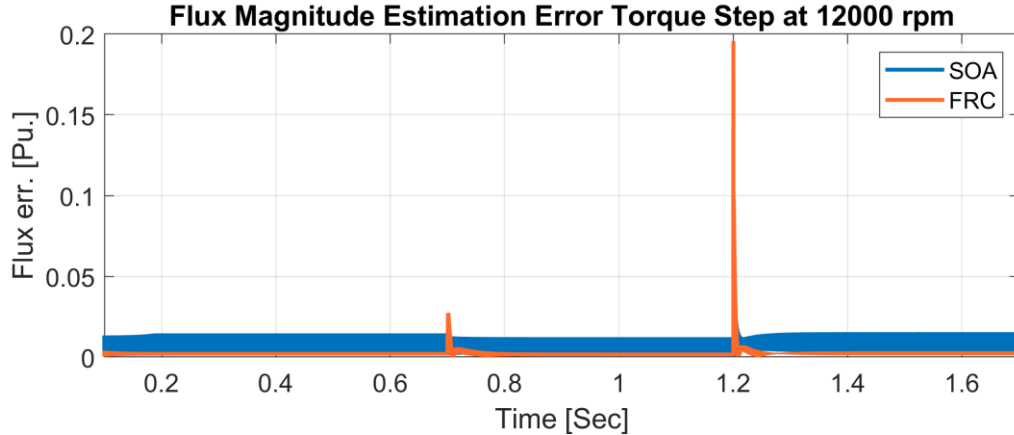


**Figure 59** Flux magnitude deviation, torque step response at 12000 rpm. (Blue) absolute flux magnitude error form the SOA Observer. (Orange) absolute flux magnitude error form the FRC Observer.

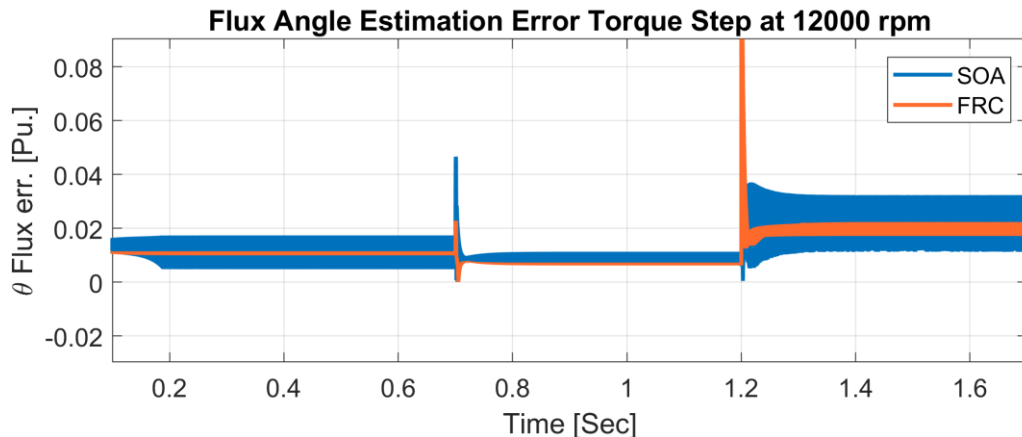


**Figure 60** Flux angle deviation, torque step response at 12000 rpm. (Blue) absolute flux angle error form the SOA Observer. (Orange) absolute flux angle error form the FRC Observer.

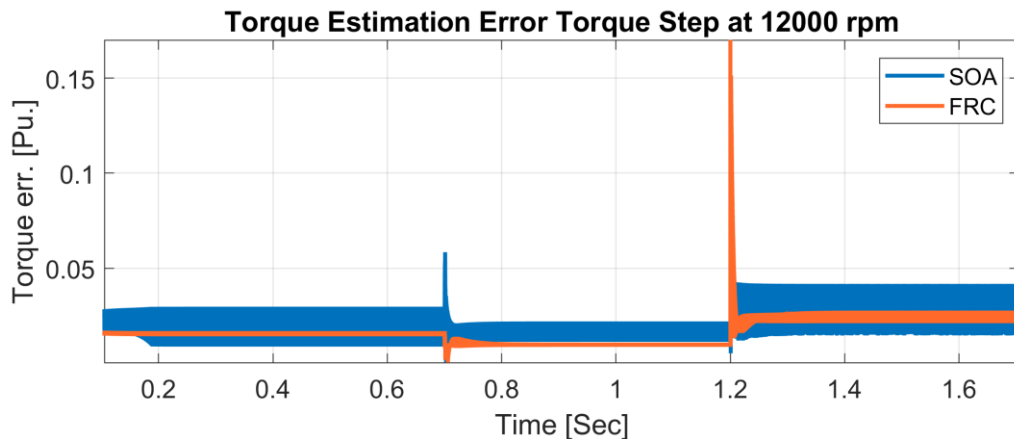


**Figure 61** Torque deviation, torque step response at 12000 rpm. (Blue) absolute torque error form the SOA Observer. (Orange) absolute torque error form the FRC Observer.

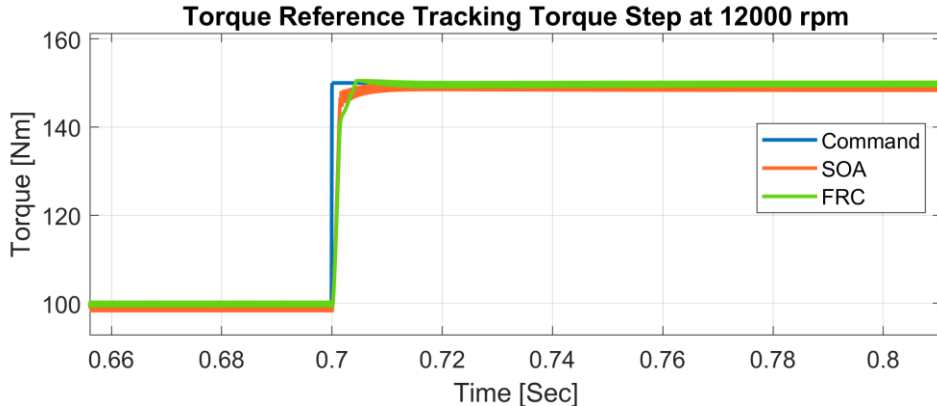


**Figure 62** SOA VS FRC Torque Step Response Reference tracking to 100, 150, and 50 N/m Benchmarking. (Blue) Commanded Torque. (Orange) torque obtained by implementation of the SOA Observer. (Green) torque obtained by implementation of the FRC Observer.

Figure 63 shows the data analysis of the values obtained from simulation at  $t = 0.7$  Sec. Where a torque step is applied. Both responses reduce the error quite significantly and are stable in Steady State.

- The results show a least distorted magnitude estimation for the case of the FRC; nevertheless, the average error is quite similar between the FRC and the SOA.
- The angle error is smaller in the FRC the increase of angle error due to the increase of speed is smaller in the FRC model.
- The Torque magnitude error is around 40% smaller in the FRC than in the SOA model.

It is important to notice that a decreased dependency respect to the speed of the drive is notable in this configuration.

### 3.1.6 Conclusions:

The Observer Characteristic Method was used to perform a frequency response correction for the IPMSM Flux linkage Observer. The implementation is proven possible in the frequency domain if the correct angles are considered.

From the implementation, note that under a speed ramp:

- At the constant torque region, the distortion of the FRC is smaller than the SOA model; nevertheless, noise is still present in both models.

- The transition of the FRC is less distorted than the SOA in magnitude.
- At the current limit, the models behave similarly.
- At 6000 RPM, the SOA error increases with speed while the FRC is kept constant.
- At 16 000 RPM the error of the SOA is another order of magnitude bigger than the FRC

The parameter sensitivity test was performed under closed loop conditions and compared with the SOA. Is possible to say that:

- The FRC corrected observer has a higher dependency on the Current Model and therefore is more parameter sensitive than the SOA.
- If a parameter LUT is implemented in the system this problem might not be an issue since the most sensitive parameters like inductance and  $\lambda_{pm}$  are updated for each frequency and temperature.

The system dynamics at low speeds show that:

- The magnitude error rejection capability of the FRC is higher than the one of the SOA.
- The angle error is corrected faster in the SOA, but the overshoot is bigger.

The system dynamics at high speeds show that:

- The results show a least distorted magnitude estimation for the case of the FRC the steady state error is 10 times smaller compared with the SOA.
- The angle error is smaller in the FRC the increase of angle error due to the increase of speed is smaller in the FRC model.
- The Torque magnitude error is around 40% smaller in the FRC than in the SOA model.

Respect to the computational effort:

- The computational effort is larger for the FRC method, if the implementation is desired it could be an option to prepare optimized Taylor series expansions for  $(x)$ ,  $abs(x)$ , and  $e^x$  to reduce the computational requirements.



# Chapter Four

## 4 Iron Losses and their effect on the flux linkage estimator.

Through the literature review, presented in Chapter 2, it has been concluded that there is no information about the iron losses impact on the Gopinath style flux observer nor a correction factor for the flux estimation in DB-DTFC.

This chapter is constructed as follows.

First, some additional literature ideas for the iron losses and iron loss models is exposed.

Second, based on the literature an iron loss model is proposed and implemented based on experimental data. The iron loss resistance is mapped along the operation range.

Third, a steady state model is used to show the different effects produced by the iron losses in the system.

Finally, a correction factor for the magnetic models of the flux observer is proposed and evaluated.

### 4.1 Models for the Iron Losses, definitions and benchmark.

#### 4.1.1 Introduction

In an IPMSM the rotor is made from different conductor materials. A magnetic field travels through the air gap of the machine into the rotor. This magnetic flux is not constant. When the machine rotates, an electric current is induced in the machine's rotor laminations and magnets as well as in the stator iron. These currents are called eddy currents.

At low speeds this current are insignificant and therefore it is quite accurate to assume them of negligible magnitude. Nevertheless, at high speeds, they become significant and can produce noticeable losses.

The eddy currents must flow through a piece of the machine rotor materials, who will have a certain conductivity depending on its particularities. Some of the machine power will be dissipated as joule losses in the iron and other materials. These losses are called Eddy losses.

On the other hand, this current will induce a magnetic field in the other parts of the machines. It is important for our discussion to understand that this field will produce losses in the machine as well. It will generate an undesired magnetic field in the machine, noise and winding torque in a none ideal direction. These losses are called Hysteresis Losses.

For our discussion, it is important to point out two things:

Both Eddy and Hysteresis Losses are produced by the eddy currents in the rotor of the machine.

The currents are proportional to the rate of change in the flux and therefore to the speed of the machine.

#### 4.1.2 Iron Loss Modeling

Different approaches exist in order to model the iron losses, it is important to notice that they can be separated into two main groups. Physical Models for finite element computation like the one of Figure 64 (F), and electrical equivalent circuits.

In order to understand the impact of the iron losses on the control the electrical models are used. A collection of the different approaches to model the steady state iron losses is shown in Figure 64.

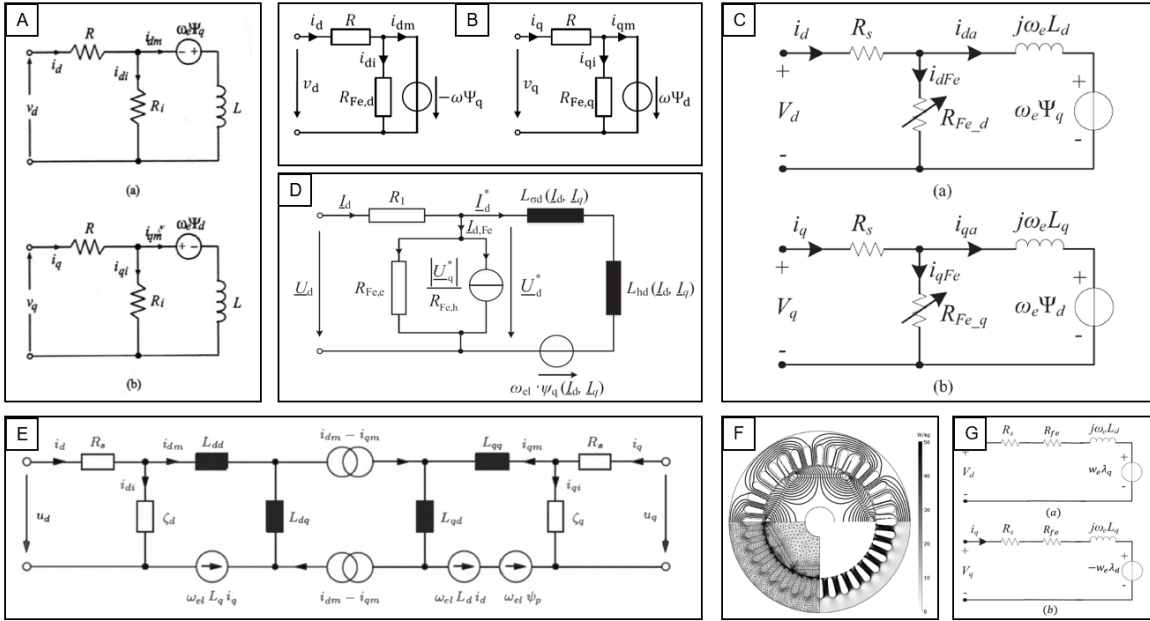


Figure 64 Collection of Iron Losses equivalent circuits proposed in the literature. (A) Parallel Iron loss resistance to magnetizing branch by [21], (B) First Harmonic circuit [22], (C) Variable asymmetrical iron loss resistances by [23], (D) Eddy Currents and Hysteresis Iron loss by [24], (E) Iron Loss Model Considering asymmetric iron loss resistances and cross saturation by [25], (F) Finite Elements Model by [26], (G) Series Resistance model.

The model of Figure 64 (A) presents the most classical approach. A model that includes a parallel iron loss resistance to the magnetization branch. This model is simple to compute and shows the most impacting fact about this model, that the magnetization current is not the same current as the one seen in the terminals of the machine.

In comparison, the model presented in Figure 64 (G) is an example of a circuit criticized in the literature by [27] as a model that only displays the additional power loss, but is not consistent with the open loop no load tests of a machine.

Figure 68 (B) displays a system that is only compliant for the first harmonic in steady state. Since in the Inductance of the machine is neglected. [28] states that only the first harmonic will influence the flux angle and therefore distinguishes the iron loss models between the effects produced under PWM and Sinusoidal supplies.

It is interesting to note that most of these authors propose that the iron losses resistance must be updated along the speed range. As in Figure 64 (B), (C) and (E) it might be sometimes suggested that the d and q axis resistances are not equal, but that the difference cannot be easily calculated experimentally. Nevertheless, the author of Figure 64 (D) suggests using the Finite Elements simulation data to produce a map for the Iron losses. He makes a difference between the eddy losses and the hysteresis losses. In the process he proves that the d axis and the q axis resistances obtained are equal for each torque speed point.

Finally, Figure 64 (E) proposes a model that includes the effect of crossed saturation in the machine. This model is further cited in the literature but difficult for practical implementation.

### Conclusions

- A parallel resistance to the Magnetizing branch represents best the steady state losses produced by the iron losses.
- The iron losses model must update the resistance value for the speed and ideally torque range to be most accurate.
- It is not necessary to model the d and q axis resistances as asymmetrical.
- Finite element simulation of the machine results as well as no load losses experimental data can be used to obtain a table of values for the iron losses resistance.

## 4.2 Iron Loss model Implementation.

From the conclusions of the previous sections it a circuit like the one on Figure 65 (C), is chosen. If the KVL and KCL are used to describe the circuit, a set of equations that describe this system in the rotor reference frame is obtained as:

$$V_{ds} = R_s i_d + R_{fed} i_{ed} \quad (98)$$

$$V_{ds} = R_s i_d + L_d \frac{di_{md}}{dt} - w_e \lambda_q \quad (99)$$

$$V_{qs} = R_s i_q + R_{feq} i_{eq} \quad (100)$$

$$V_{qs} = R_s i_q + L_q \frac{di_{mq}}{dt} + w_e \lambda_d \quad (101)$$

$$i_d = i_{md} + i_{fed} \quad (102)$$

$$i_q = i_{mq} + i_{feq} \quad (103)$$

$$\lambda_{ds} = L_d i_{md} + \lambda_{pm} \quad (104)$$

$$\lambda_{qs} = L_q i_{mq} \quad (105)$$

From this new set of equations, it is possible to build a Simulink model that includes the iron losses effects as described in figure (66). Finally, from the model outputs all the required states for the simulation can be obtained.

Now if by looking at the Simulink model of figure (66), the values of the resistances that simulate the Iron Losses are feed to the model from a constant value. A LUT, a function, or the value obtained from an estimator method could be used in replacement. Providing this model, a full range of operation and a higher accuracy.

Finally, if the model is supplied with a large resistance, an open circuit is simulated and the old model of the IPMSM is reached.

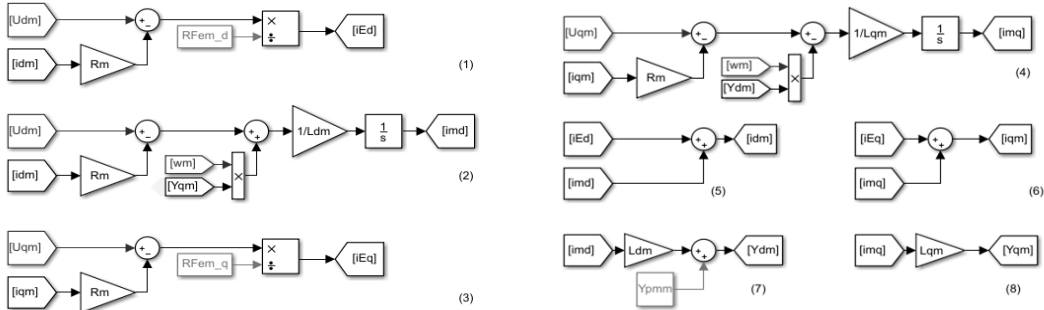


**Figure 66 Simulink model of the IPMSM considering Iron Losses. In these system equations, (98) to (105) are represented as (1) to (8) respectively in Simulink blocks.**

In order to model the machine with accuracy, the iron loss resistance can be implemented in a lookup table but first the iron loss resistance must be calculated.

Different methods exist to calculate the iron loss resistance. One of the most commonly used methods is to perform the no load power test for the machine. To do so the machine is driven in open circuit at different speeds with another machine of known operating conditions. From here, the power required to move the machine is calculated. The machine armature is previously tested without magnets and windings so that the power dissipated as friction is known. Finally, the dissipated power is calculated.

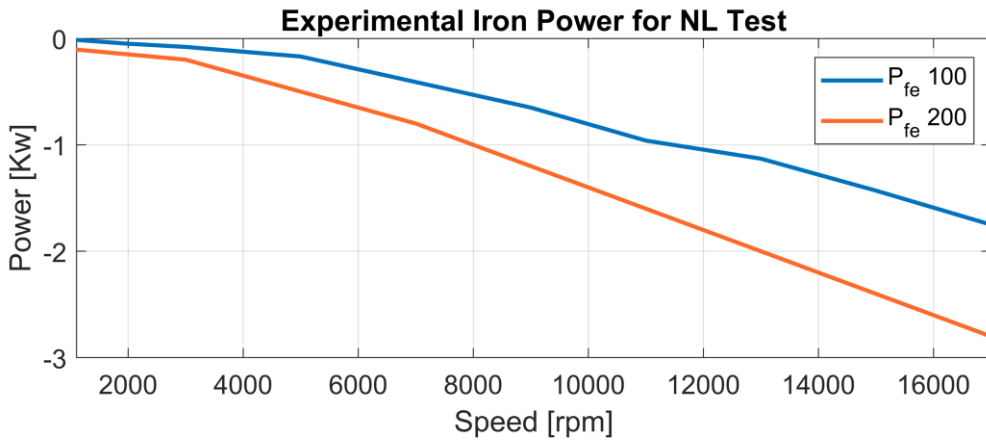


Figure 67 Experimental Iron Loss Power for 100- and 200-mm machines. (Blue) Iron loss power from the no load tests for 100 mm machine. (Orange) Iron loss power from the no load tests for 200 mm machine.

From the obtained power and by means of the following equation:

$$R_{fe} = \frac{3 We^2}{2 P_{fe}} \lambda_{pm}^2 \quad (106)$$

The iron loss resistance can be calculated.

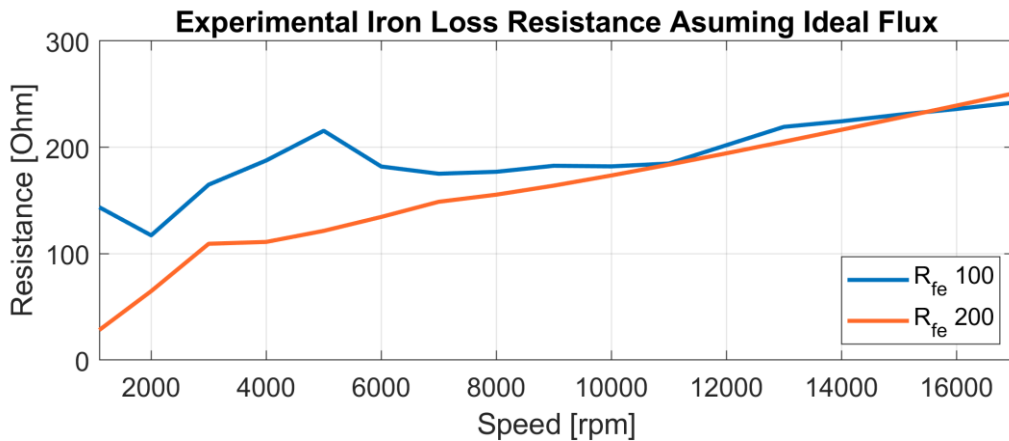


Figure 68 Iron Loss Resistance from Experimental NL losses for 100- and 200-mm machines. (Blue) Iron loss resistance from the no load tests for 100 mm machine. (Orange) Iron loss resistance from the no load tests for 200 mm machine.

Conclusions:

- Since at the zero speed no power is introduced in the machine the resistance can't be accurately calculated.

- For the no load condition, the no load condition the iron loss resistance increments with the speed for both machines.
- From the data, a LUT can be implemented in simulation in order to model the machine including iron losses.

[24] Proposes that this data can be used to obtain an approximation for all the operation torque and speed points. Although useful, if the machine iron loss power is available from the original designer. The efficiency map can be used to obtain an iron loss resistance map.

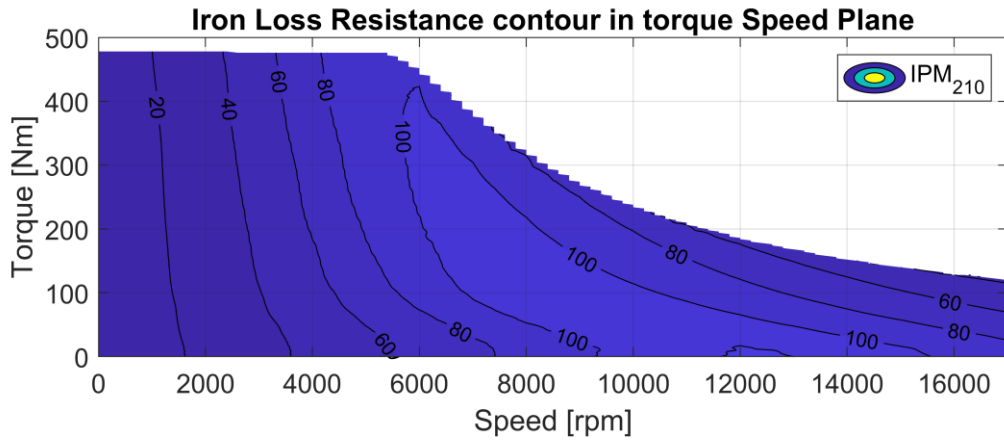


**Figure 69** Iron Loss Resistance map from FEM iron loss power data for IPM 210 600V Machine. (Contours) Iron loss resistance in Ohms for the 200 mm Machine.

### Conclusions

- The Machine Iron Loss Measurements are consistent and therefore the iron loss resistance can be properly approximated.
- The contours of the iron loss resistance show a clean iron loss resistance value for each operation point. The results are consistent with the results obtained from experimental data for No Load condition in the previous section.
- From the machine operation data, it is important to notice that: at max speed the current and flux of the machine is not kept constant along the different torque profile.  $I_d$  and  $I_q$  are controlled differently as in the assumed model.
- From the data, a 2-D LUT can be implemented in simulation in order to model the machine including iron losses.

## 4.3 Effect of Iron Losses in the drive control system.

### 4.3.1 Iron loss steady state model for IPMSM

In order to study the effects of the iron losses a steady state equivalent model of the system is used as:

$$V_{ds} = R_s i_d + R_{fed} i_{fed} \quad (107)$$

$$V_{ds} = R_s i_d - w_e \lambda_q \quad (108)$$

$$V_{qs} = R_s i_q + R_{feq} i_{feq} \quad (109)$$

$$V_{qs} = R_s i_q + w_e \lambda_d \quad (110)$$

$$i_d = i_{md} + i_{fed} \quad (111)$$

$$i_q = i_{mq} + i_{feq} \quad (112)$$

$$\lambda_{ds} = L_d i_{md} + \lambda_{pm} \quad (113)$$

$$\lambda_{qs} = L_q i_{mq} \quad (114)$$

From this model, one of the most important details can be noted if the fluxes are expressed as a function of the currents. The relationship described from the fluxes is:

$$\lambda_{ds} = L_d i_d + L_d \frac{w_e \lambda_q}{R_{fed}} + \lambda_{pm} \quad (115)$$

$$\lambda_{qs} = L_q i_q - L_q \frac{w_e \lambda_d}{R_{feq}} \quad (116)$$

These equations show that although if pure d axis current is introduced ( $i_q = 0$ ) in the system, at high speeds a q axis flux exists and therefore at high speed with pure d-axis current torque is produced.

Another important issue is that the torque equation is also modified as:

$$T_e = \frac{3}{2} p [\lambda_{ds} i_{qm} + \lambda_{qs} i_{dm}] \quad (117)$$

For the torque to be zero  $i_{qm}$  needs to be equal to zero, and therefore the iron loss current must be compensated. This will be further examined in the next section.

Finally, it is important to note that if the machine is rotating at a given speed in open circuit condition, a magnetizing current exists, since the flux produces a potential across the iron loss resistance.

### Conclusions:

- An intrinsic coupling effect exists in the system between the d-axis and q-axis, this coupling is proportional to the flux linkages of both axes, the speed, and depends on the equivalent iron loss resistance for the operation point.
- The flux control variable is not the stator current but the magnetizing portion of it, the control system has no direct access to it. Therefore, the magnetizing current can only be estimated.
- In a CVC application, the iron loss current will have to be compensated along the speed range in order to perfectly decouple the d and q axis.

#### 4.3.2 Effects of Iron loss model for IPMSM in SS.

##### 4.3.2.1 Effect on the currents:

In order to show graphically the solution, a command of  $i_q = 0$  and  $i_d = 10$  at  $w_m = 17.000$  rpm is studied. With the help of numerical analysis, the ss equations of the IPMSM model with iron loss resistor is solved. The resulting phasor diagrams for the current and flux are displayed.

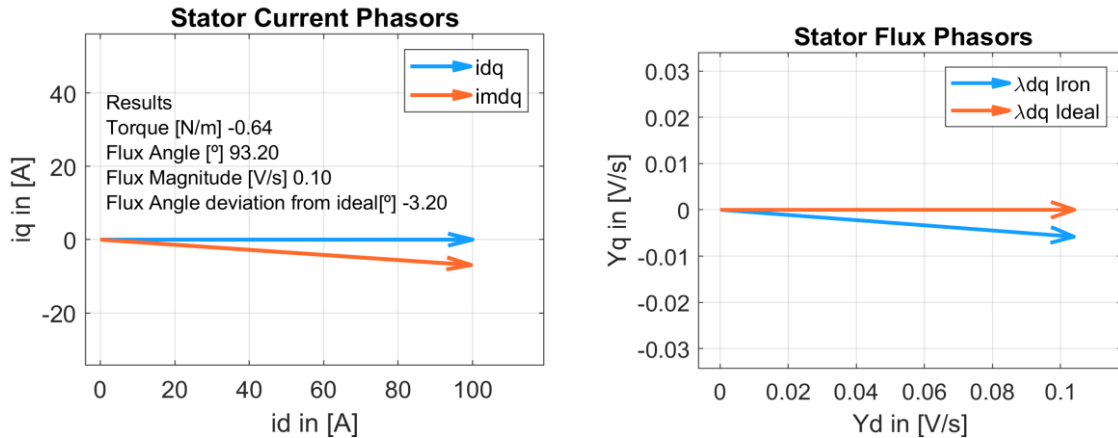


**Figure 70 Impact of Iron Losses in the machine with pure  $i_d$  current currents at high speed. (Left)** Impact of the iron losses resistance in the magnetizing current. Deviation results are displayed in the figure. **(Right)** Impact of the iron losses resistance in the machine flux.

### Conclusions:

As it is possible to see in the figure due to the coupling at high speeds, a  $3.2^\circ$  deviation is present on the stator flux. Since the flux produced induces, a magnetizing current a small torque of  $1.81\text{N/M}$  is produced.

It is important to understand that the iron loss deviate the angle only with the fundamental component of the magnetizing current. As explained by [28] , higher order harmonics coming from the inverter would not be DC quantities in the rotor reference frame and therefore would not produce an angle deviation in the control system.

#### 4.3.2.2 Positive v/s Negative d-axis current effect with no q-axis current:

Experimental conditions:  $speed = 17\,000\text{ rpm}$ ;  $id\_cases = [100, -100]$ ;  $iq\_cases = [0, 0]$ ;

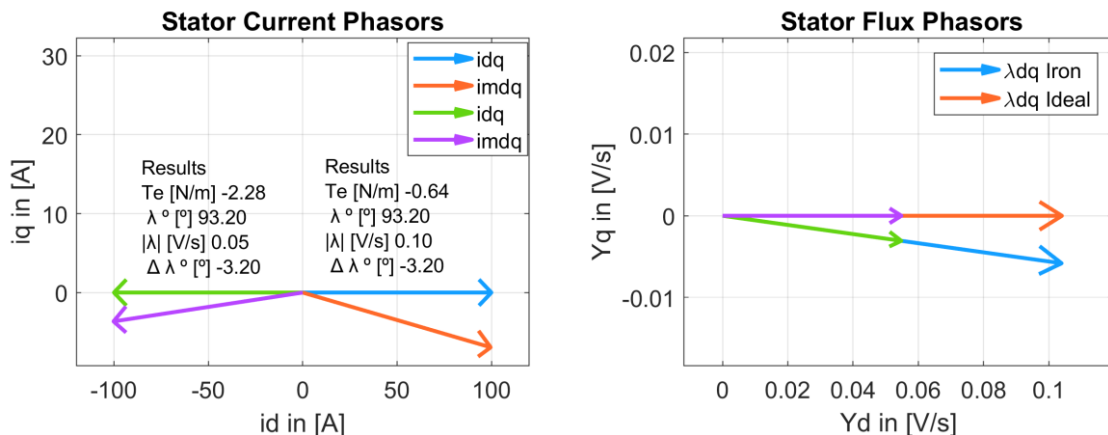


Figure 71 3 Phasor Diagram of Positive v/s Negative d-axis current with no q-axis current for  $id=+100\text{A}$   $iq=0$ . (Left) Impact of the iron losses resistance in the magnetizing current. Deviation results are displayed in the figure. (Right) Impact of the iron losses resistance in the machine flux.

Conclusions:

- The flux angle distortion is maintained although the current is inversed.
- The current distortion angle has opposite directions since the magnetizing current is proportional to the flux and the flux does not change directions. This is explained due to the presence of the permanent magnet flux.
- If the commanded current would be such to overcome the pm flux the current distortion would go in the other direction.
- A torque asymmetry is present between motoring and generating conditions since the iron losses effect increases the torque in generating condition.

**Table 3 Results of Positive v/s Negative d-axis current with no q-axis current for id=+-100A**

id	iq	imd	imq	ifed	ifeq	Vds	Vqs	Yd	Yq	Te	Flux_Angle	Flux_mag
100	0	99.612	-6.9389	0.38819	6.9389	32.165	555.11	0.10394	-0.0058148	-0.63902	93.202	0.1041
-100	0	-100.2	-3.6574	0.20461	3.6574	15.259	292.59	0.054785	-0.0030649	-2.2837	93.202	0.054871

#### 4.3.3 Increasing d-axis current effect with no q-axis current:

Experimental conditions:  $speed = 17\ 000\ rpm$ ;  $id\_cases = [10,50,100,200]$ ;  $iq = 0$ ;

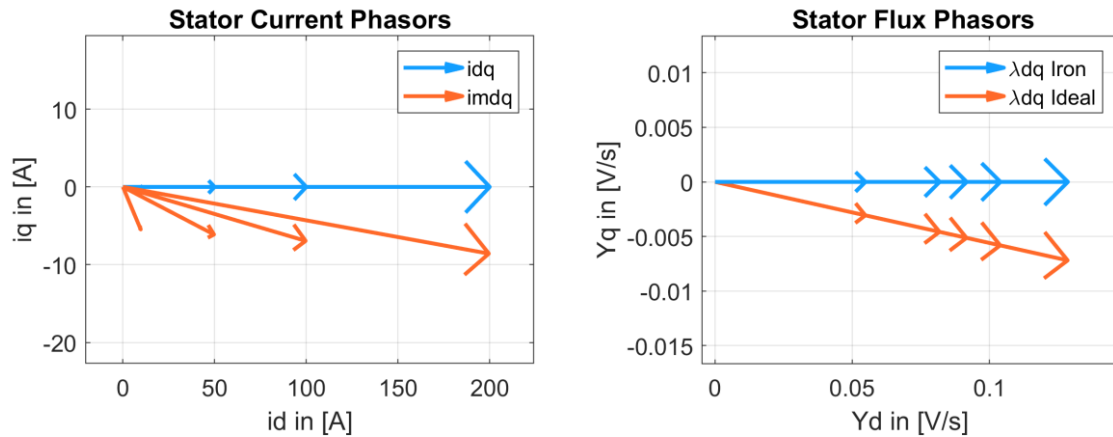


**Figure 72 Phasor Diagram of increasing d-axis current effect with no q-axis current. (Left) Impact of the iron losses resistance in the magnetizing current. (Right) Impact of the iron losses resistance in the machine flux.**

#### Conclusions

- From the results, the angle of the magnetizing current is inversely proportional to the  $i_d$  current.
- The angle of the flux linkage vector is not dependent on the magnitude of the d axis current.
- As  $i_d$  increases, the q axis component increases proportionally to the d axis flux component confirming the relationship of equation (116).
- It is interesting to note that the torque changes sign at  $i_d = 200$  [A], since the current can overcome the effect of the permanent magnet flux. From the results table down below it is also possible to see that with the d axis current, most of the losses due to iron losses occur on the q axis. Since the field induced is coupled and produces a voltage over the iron loss resistance.

**Table 4 Results of increasing d-axis current effect with no q-axis current**

id	iq	imd	imq	ifed	ifeq	Vds	Vqs	Yd	Yq	Te	Flux_Angle	Flux_mag
10	0	9.6944	-5.4622	0.30558	5.4622	24.557	436.98	0.08182	-0.0045773	-1.8114	93.202	0.081948
50	0	49.658	-6.1185	0.34229	6.1185	27.938	489.48	0.091651	-0.0051273	-1.3777	93.202	0.091794
100	0	99.612	-6.9389	0.38819	6.9389	32.165	555.11	0.10394	-0.0058148	-0.63902	93.202	0.1041
200	0	199.52	-8.5797	0.47998	8.5797	40.618	686.37	0.12852	-0.0071898	1.4934	93.202	0.12872

#### 4.3.4 Positive v/s Negative q-axis current effect with no d-axis current:

Experimental conditions:  $speed = 17\ 000\ rpm$ ;  $iq\_cases = [100, -100]$ ;  $id\_cases = [0, 0]$ ;

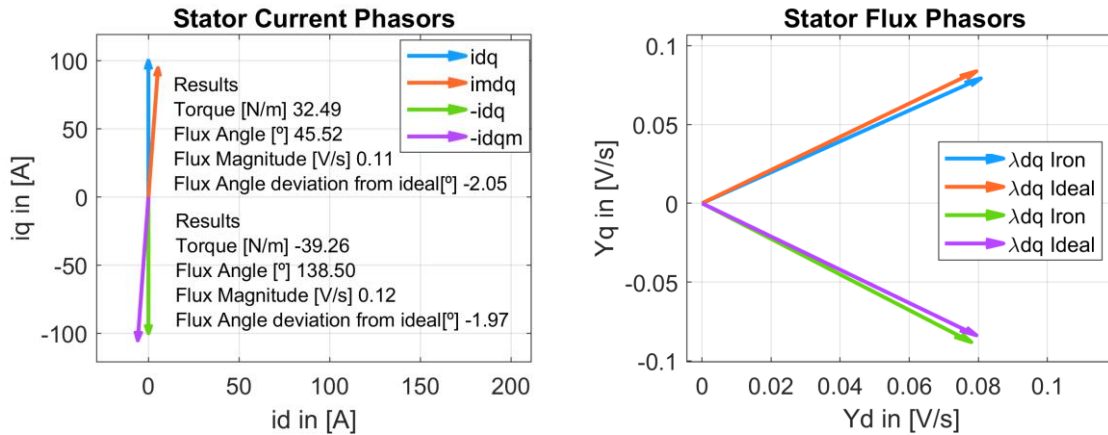


**Figure 73 3 Phasor Diagram of Positive v/s Negative q-axis current with no d-axis current for  $iq=+100A$   $id=0$  (Left)**  
**Impact of the iron losses resistance in the magnetizing current. Deviation results are displayed in the figure. (Right)**  
**Impact of the iron losses resistance in the machine flux.**

#### Conclusions

- The flux angle is lagging the expected field orientation by approximately 2 degrees.
- In motoring condition, the distortion produced by the iron losses increases the current while under generating condition it increases compared with the phase current.
- It is interesting to notice that while the iron losses suppose a problem while motoring since they reduce the torque, they increase the torque in the generating condition.
- This asymmetry on the torque should be assessed in further detail.

**Table 5 Results of Positive v/s Negative d-axis current with no d-axis current for  $iq=+100A$**

id	iq	imd	imq	ifed	ifeq	Vds	Vqs	Yd	Yq	Te	Flux_Angle	Flux_mag
0	100	5.2929	94.61	-5.2929	5.3899	-423.43	432.3	0.080737	0.079283	32.485	45.521	0.11316
0	-100	-5.8857	-105.21	5.8857	5.2063	470.85	415.4	0.077987	-0.088163	-39.256	138.5	0.11771

#### 4.3.5 Increasing q-axis current effect with no d-axis current:

Experimental conditions:  $speed = 17\,000\,rpm$ ;  $iq\_cases = [10, 50, 100, 200]$ ;  $id = 0$ ;

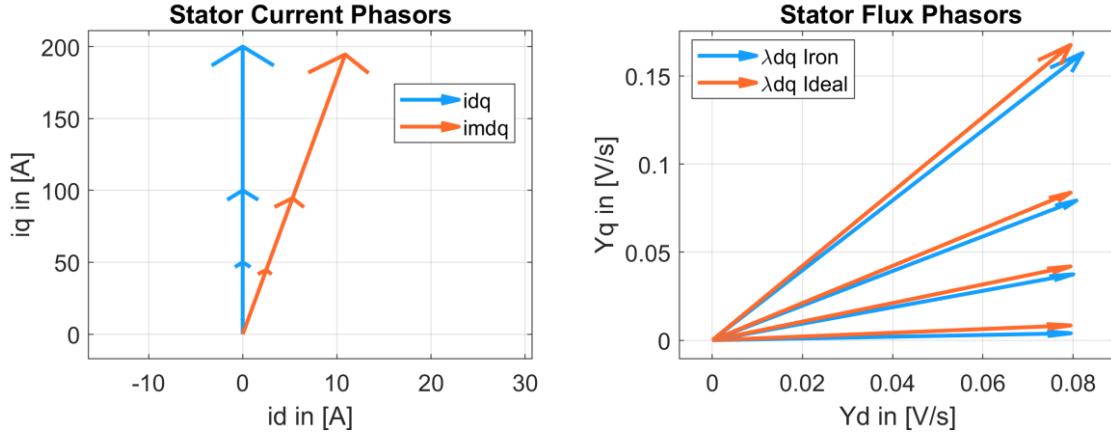


Figure 74 Phasor Diagram of increasing q-axis current effect with no d-axis current. (Left) Impact of the iron losses resistance in the magnetizing current. Deviation results are displayed in the figure. (Right) Impact of the iron losses resistance in the machine flux.

#### Conclusions

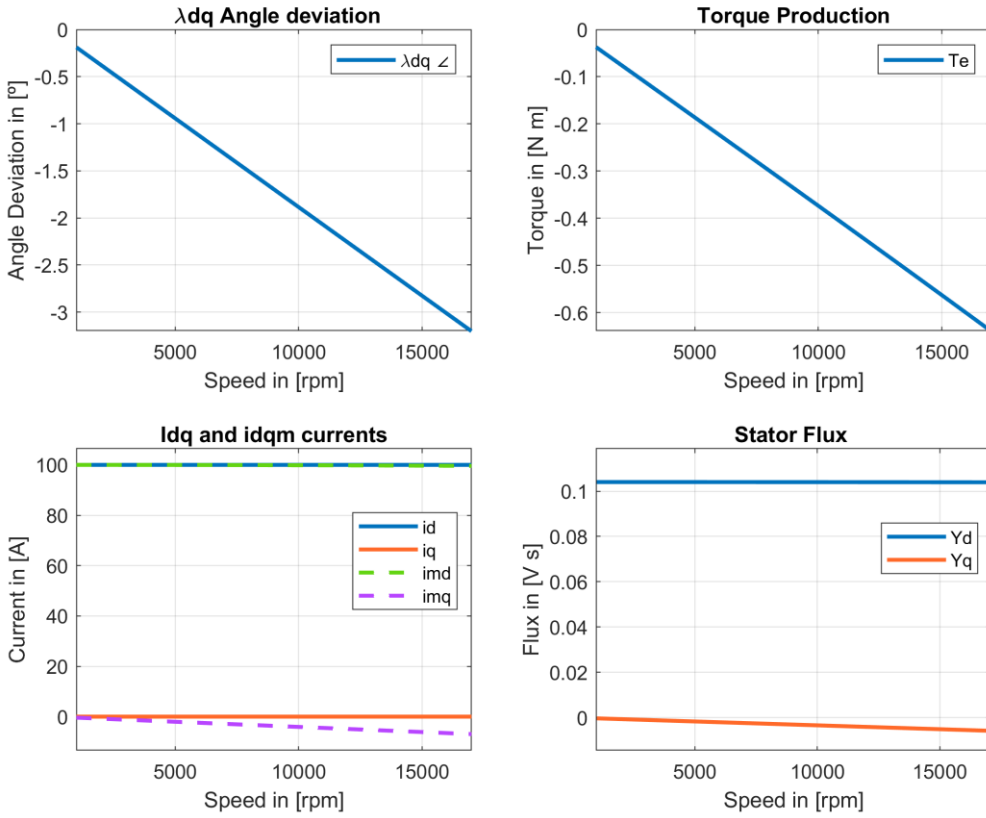
- From the figure, no ideal decoupling between torque and flux occurs. The flux changes when the d axis current is maintained.
- The flux vector lags the commanded flux linkage vector.

Table 6 Results of increasing d-axis current effect with no q-axis current

$id$	$iq$	$imd$	$imq$	$ifed$	$ifeq$	$Vds$	$Vqs$	$Yd$	$Yq$	$T_e$	$Flux\_Angle$	$Flux\_mag$
0	10	0.26253	4.6927	-0.26253	5.3073	-21.002	424.7	0.0795	0.0039325	1.6742	87.168	0.079597
0	50	2.4982	44.656	-2.4982	5.344	-199.86	428.08	0.08005	0.037422	15.665	64.945	0.088365
0	100	5.2929	94.61	-5.2929	5.3899	-423.43	432.3	0.080737	0.079283	32.485	45.521	0.11316
0	200	10.882	194.52	-10.882	5.4817	-870.57	440.76	0.082112	0.16301	63.893	26.736	0.18252

#### IPMSM Iron Losses Model Speed Ramp Test

In order to test the angle deviation at different speeds, a speed ramp is introduced as input, a pure 100A d axis current is introduced in the system. The iron loss resistance is constant and equal to 80 ohm (Simplification). The results are as following:



**Figure 75** Angle deviation, Torque and flux production under a speed ramp with 100 [A] pure d axis current. (Top Left) Flux angle distortion for pure d axis current. Deviation results are displayed in the figure. (Top Right) Undesired torque production. (Bottom Left) Idq current and magnetizing current. (Bottom Right) Impact of the iron losses resistance in the machine flux.

Conclusions:

- Flux and Torque Are no longer decoupled
- The results show an angle deviation proportional to the speed of the drive and an undesired torque production at high speed.
- These deviations might not be notable in other small drives or drives without field weakening.
- The angle distortion is dependent on the Iron loss resistance, a full model of the iron loss resistance would produce a more accurate result.

**Table 7 Speed Ramp output variables**

Speed_rpm	id	iq	imd	imq	ifed	ifeq	Vds	Vqs	Yd	Yq	Te	Flux_Angle	Flux_mag
1000	100	0	99.999	-0.40854	0.0013444	0.40854	1.2176	32.684	0.10403	-0.00034236	-0.037203	90.189	0.10404
2000	100	0	99.995	-0.81708	0.0053777	0.81708	1.5402	65.366	0.10403	-0.00068471	-0.074414	90.377	0.10404
3000	100	0	99.988	-1.2256	0.0121	1.2256	2.078	98.048	0.10403	-0.0010271	-0.11164	90.566	0.10404
4000	100	0	99.978	-1.6341	0.02151	1.6341	2.8308	130.73	0.10403	-0.0013694	-0.14889	90.754	0.10404
5000	100	0	99.966	-2.0426	0.033609	2.0426	3.7987	163.41	0.10403	-0.0017117	-0.18618	90.943	0.10404
6000	100	0	99.952	-2.451	0.048395	2.451	4.9816	196.08	0.10402	-0.0020539	-0.22335	91.131	0.10404
7000	100	0	99.934	-2.8594	0.065868	2.8594	6.3794	228.75	0.10402	-0.0023962	-0.26087	91.32	0.10405
8000	100	0	99.914	-3.2677	0.086027	3.2677	7.9922	261.42	0.10401	-0.0027383	-0.2983	91.508	0.10405
9000	100	0	99.891	-3.676	0.10887	3.676	9.8198	294.08	0.10401	-0.0030805	-0.33579	91.696	0.10405
10000	100	0	99.866	-4.0842	0.1344	4.0842	11.862	326.73	0.104	-0.0034225	-0.37336	91.885	0.10406
11000	100	0	99.837	-4.4923	0.16262	4.4923	14.119	359.38	0.104	-0.0037645	-0.41101	92.073	0.10406
12000	100	0	99.806	-4.9003	0.19351	4.9003	16.591	392.02	0.10399	-0.0041065	-0.44874	92.261	0.10407
13000	100	0	99.773	-5.3082	0.22709	5.3082	19.277	424.66	0.10398	-0.0044483	-0.48657	92.45	0.10407
14000	100	0	99.737	-5.7161	0.26335	5.7161	22.178	457.29	0.10397	-0.0047901	-0.52451	92.638	0.10408
15000	100	0	99.698	-6.1238	0.30228	6.1238	25.293	489.9	0.10396	-0.0051317	-0.56255	92.826	0.10409
16000	100	0	99.656	-6.5314	0.3439	6.5314	28.622	522.51	0.10395	-0.0054733	-0.60072	93.014	0.10409
17000	100	0	99.612	-6.9389	0.38819	6.9389	32.165	555.11	0.10394	-0.0058148	-0.63902	93.202	0.1041

#### 4.3.6 Effect of Iron losses on the voltage vector

Under a speed ramp, the voltage is examined when no current flows

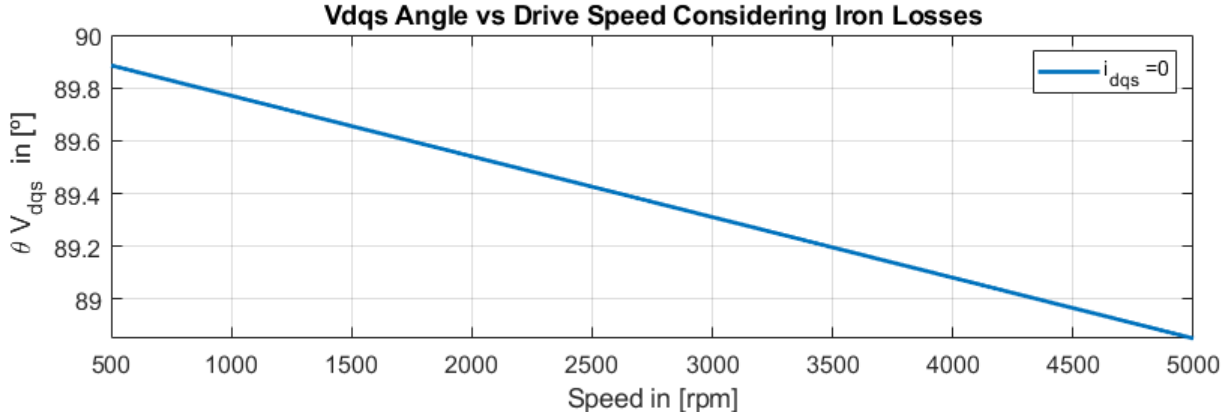


**Figure 76** Vdqs Angle at zero Idqs vs speed range for id=0. (Blue) voltage vector angle obtained with Idqs=0 at different speeds.

From Figure 77, the iron losses introduce an angle deviation in the voltage. In performance drives automatic angle tuning routines use such a measurement to align the system angle. An error is introduced in the algorithm by the iron losses.

Now the same experiment is repeated but the pure d axis current is injected. It is important to understand the following, if an ideal model is considered; the current the angle deviation is increased, but why?

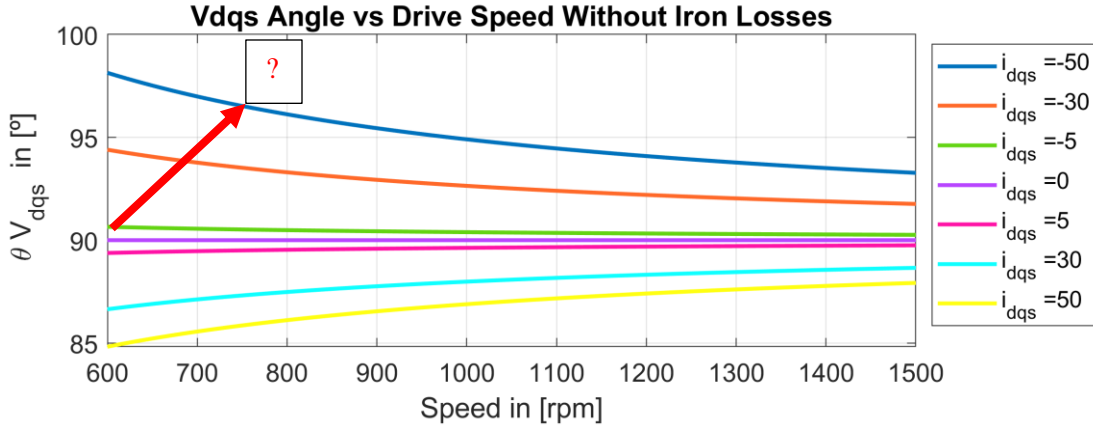


Figure 78 Voltage vector angle of the ideal Model of the IPMSM in SS. (All colors) voltage vector angle obtained with different  $i_{dqs}$  inputs at different speeds.

Considering the IPMSM SS Voltage equations in the rotor reference frame as:

$$V_{ds} = R_s I_d - w_e \lambda_q \quad (118)$$

$$V_{qs} = R_s I_q + w_e \lambda_d \quad (119)$$

Under a current of  $I_d=-30$  and  $I_q=0$ ; At low speeds the voltage is purely in the d axis ad it is proportional to the current since  $w_e = 0$ ; therefore, the voltage angle is 180 degrees. Then as the speed increases, a bigger portion of the voltage is placed into the flux, now  $Vq$  starts increasing and  $Vd$  starts decreasing since the flux is proportional to the speed and the q axis joule losses are none existent. Finally, when the resistive losses are insignificant the flux appears aligned with the q-axis.

If a higher current is commanded, a higher resistive loss is presented and therefore more speed is required in order to neglect the effect of the voltage drop in the stator winding. The angle is therefore aligned at higher speeds with the q-axis.

Next in the iron loss model where,

$$\lambda_q = L_q I_{qm} \quad (120)$$

$$\lambda_d = \lambda_{pm} + L_d I_d \quad (121)$$

The ss equations it is simple to prove that the voltage equations can be expressed as a function of  $i_d$  and  $i_q$  as:

$$V_{ds} = \frac{1}{A} (R_{fe}^2 R_s i_d + L_q R_{fe} Y_{pm} w_e^2 - L_q R_{fe}^2 i_q w_e + L_d L_q R_{fe} i_d w_e^2 + L_d L_q R_s i_d w_e^2) \quad (122)$$

$$V_{qs} = \frac{1}{A} (R_{fe}^2 R_s i_q + R_{fe}^2 Y_{pm} w_e + L_d R_{fe}^2 i_d w_e + L_d L_q R_{fe} i_q w_e^2 + L_d L_q R_s i_q w_e^2) \quad (123)$$

Where for simplicity:

$$A = R_{fe}^2 + L_d L_q w_e^2 \quad (124)$$

Under the conditions,  $i_{q0}=0$  and at low speeds, once again the  $V_{qs}$  voltage is none existent. Therefore, the voltage is aligned at  $180^\circ$  with an amplitude of:

$$V_{ds} = \frac{R_{fe}^2 R_s i_d}{R_{fe}^2 + L_d L_q w_e^2} \quad (125)$$

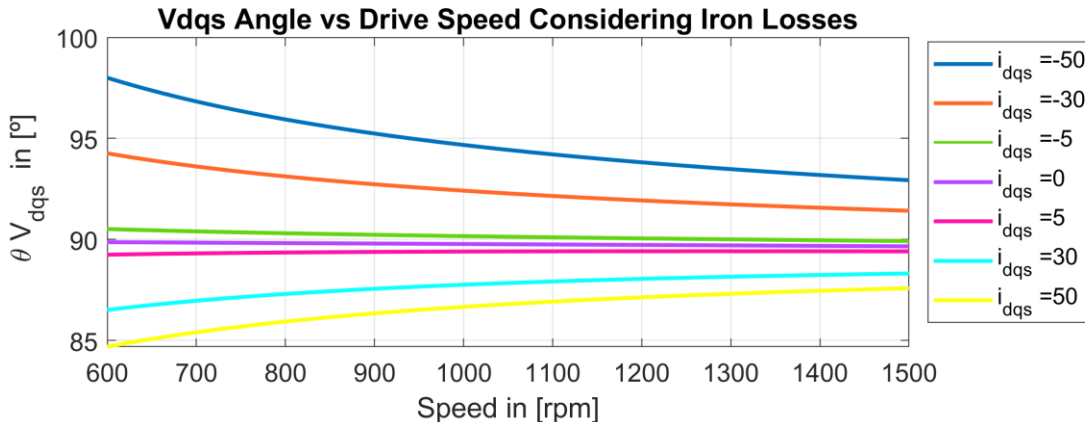


Figure 79 Voltage vector Angle Vs Speed using the SS model of the IPM Considering Iron Losses. (All colors) voltage vector angle obtained with different  $i_{dqs}$  inputs at different speeds.

As seen from the figure above, the SS model of has also a big d component at low speeds due to the stator resistance, nevertheless since the pure effect of the iron losses resistance wants to be illustrated, a figure is prepared with a small stator resistance  $R_s X = 0.01 R_s$ ;

Finally get to see the real effect of the iron losses on the voltage vector:

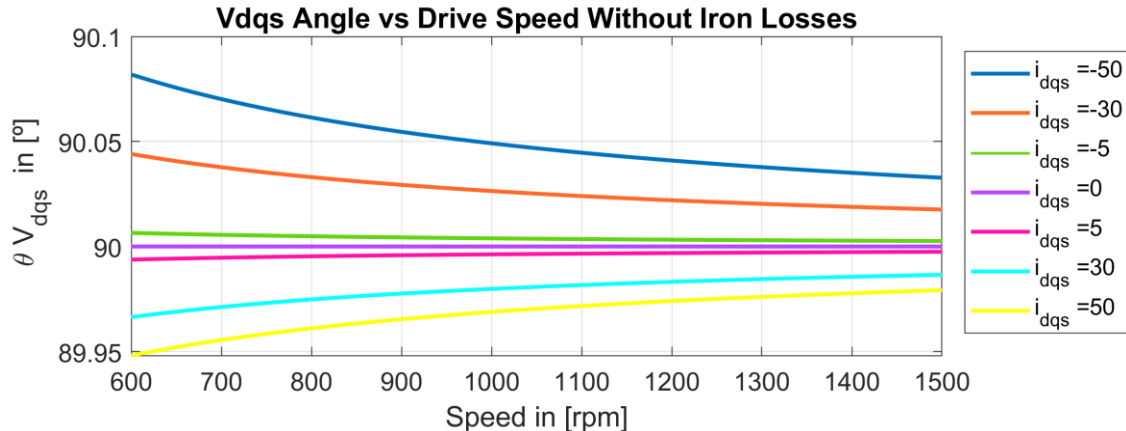


Figure 80 Reduced Stator Resistance Voltage Vector angle vs speed in steady state without Iron Losses. (All colors) voltage vector angle obtained with different  $i_{dqs}$  inputs at different speeds.

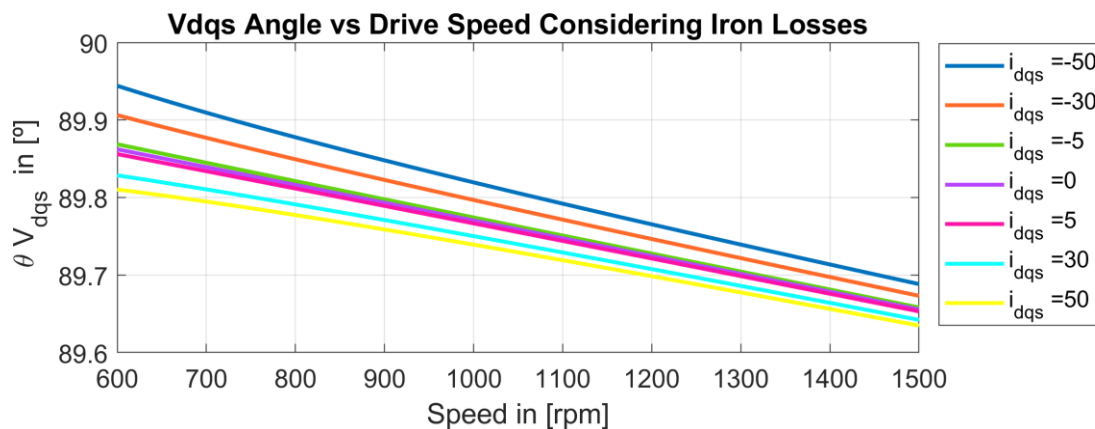


Figure 81 Reduced Stator Resistance Voltage Vector angle vs speed in steady state considering Iron Losses. (All colors) voltage vector angle obtained with different  $i_{dqs}$  inputs at different speeds.

From the figures 80 and 81 above, in an IPMSM when no q-axis current flows an asymptotic behavior is expected where the asymptote is located at 90 degrees. This is due to the inductive behavior of the load. If iron losses are introduced in the model, it becomes notable that the asymptote is no longer a fixed quantity but a tilted line that is dependent on the iron losses.

### Conclusions

- The Voltage distortion in the d axis direction is caused due to the voltage drop occurred in the stator windings.
- The voltage drop is proportional to the current due to the resistive behavior
- An expression exist that characterizes the iron losses model voltage in SS.
- With a reduced stator resistance, it is possible to isolate the effect of the iron losses.
- The iron loss resistance produces the introduction of an angle in the asymptote of the voltage when the q-axis current is zero.
- Voltage angle for no current condition shows that self-alignment routines are affected by the iron losses.
- The voltage distortion found seems to be small in the selected speed range for no current

- When there is current, a point where the distortion is equal to zero. This can be used for the angle tuning routine.

*Special Considerations.*

*When modeling the steady state model of the IPMSM it is important to look at the convention for the d-q axis in order to define the fluxes in the correct direction. Other ways the analysis of the angle will not be consistent. For this project, the real axis is aligned with the d-axis and the imaginary axis is aligned with the q-axis.*

#### 4.3.7 Zero torque production current compensation

From the SS model at 17000, 10000 and 2000 rpm, the required Idqs current is calculated so that the torque production is zero. The condition is to make  $i_{mq} = 0$  so that no torque is produced. The results are displayed as following:

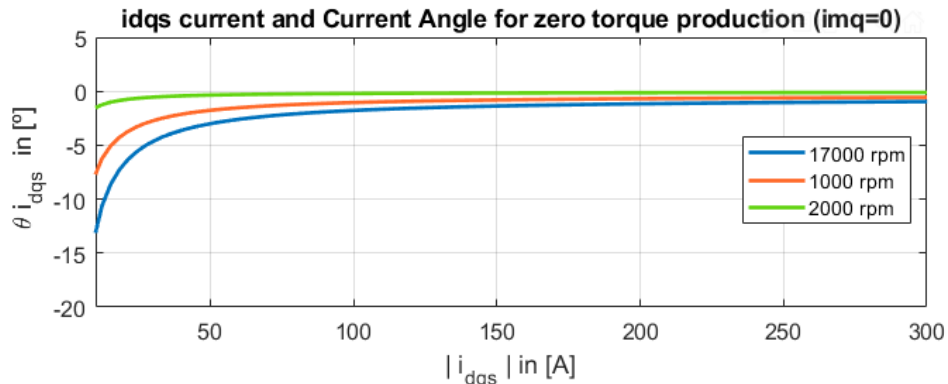
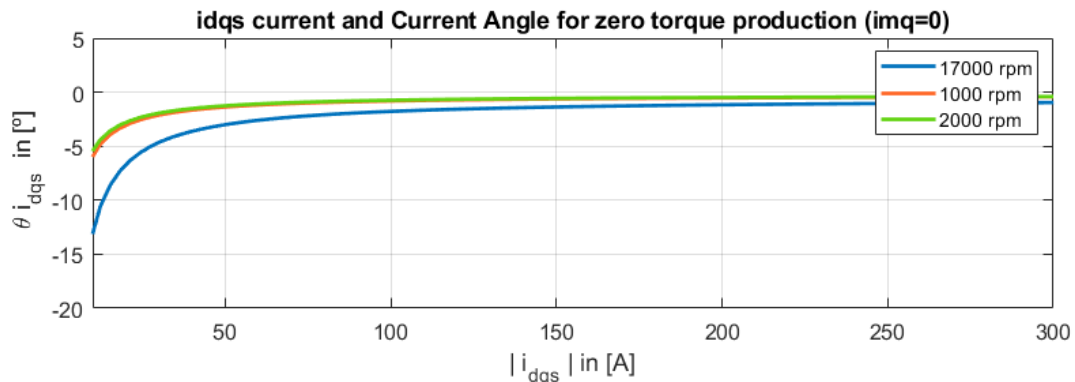


Figure 82 Results for  $R_{fe}=240$ -ohm machine parameters at 17 000 rpm. (Blue) Idqs angle for different magnitudes at 17000 rpm. (Orange) Idqs angle for different magnitudes at 10000 rpm. (Green) Idqs angle for different magnitudes at 2000 rpm.

If only the iron loss resistance values are updated for each speed condition, the results become:



**Figure 83 Results for  $R_{fe}=[240,319,70]$  ohm machine parameters at 17 000 rpm. (Blue)  $Id_{qs}$  angle for different magnitudes at 17000 rpm. (Orange)  $Id_{qs}$  angle for different magnitudes at 10000 rpm. (Green)  $Id_{qs}$  angle for different magnitudes at 2000 rpm.**

## Conclusions

- As the current increases, the current angle deviation becomes smaller.
- The distortion is speed dependent and depends on the current.
- Figure 82 contains results for constant value for  $R_{fe}$  is used, and figure 83 for an updated iron loss resistance as function of the speed. In a more exact model, the error at low speeds is bigger than if a constant value is considered.

## 4.4 Improving the Gopinath style observer to be resilient to iron losses.

In a DBDTFC drive, the iron losses do not only affect the low speed range since, the current observer is based on the magnetic model of the machine. DB-DTFC also uses the information of the magnetics model to estimate the torque. All the three observers are affected by the Iron Losses.

In order to correct, the distortion introduced by the Iron loss, the current model was corrected so that from the experimental data and a Lookup table, the magnetizing components of the currents can be calculated. This correction was afterwards applied to the flux observer and the torque calculation. The block diagram of the following figure shows the implementation:

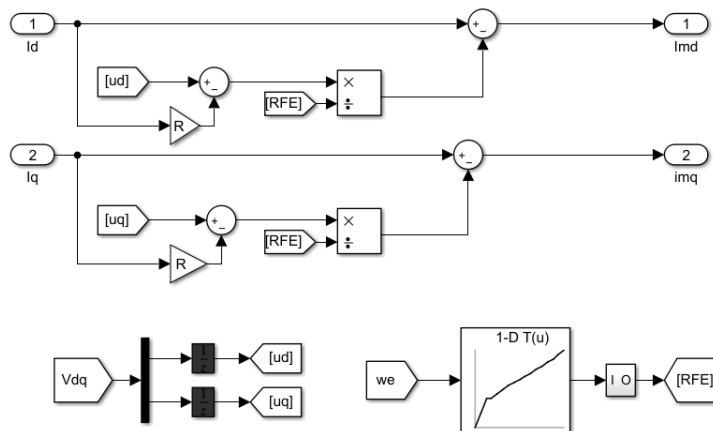


**Figure 84 Magnetizing current estimation scheme, transfers the information of  $id$  and  $iq$  from the machine measured quantities into the magnetizing components. The LUT implements the NL tests iron loss resistance for a 200mm Long Machine**

The iron losses impact on the flux observer is restricted to the low speed range when operated in open loop but since a full order observer is used for the DB-DTFC, the iron losses affect the high speed as well. Since the current estimation has an inherent error at high speed due to the iron losses.

In order to benchmark the machine operation differences, 4 simulation files were prepared. One with the State-of-the-Art observers or SOA, another with the Frequency Response Corrected Observer with Soul Correction Factor implemented or FRC. Finally, their equivalents with the magnetic models replaced for the flux linkage, current and torque observer's SOA IR and FRC IR.

The flux observer's performance was measured in terms of the accuracy of the flux estimation from the machine model, the flux angle difference and the torque estimation difference. All of this calculated under a speed ramp of 0 to 17.000 rpm.

All three indicators are displayed in the following figures.

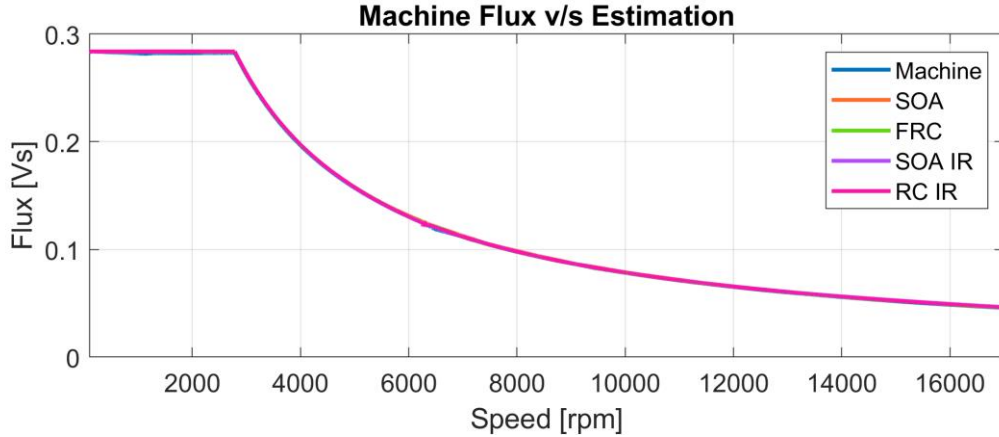


**Figure 85** Machine Flux v/s Estimation along the speed ramp for all 4 observers. (Blue) machine flux, (Orange and green) Estimated flux with SOA and FRC observers respectively. (Purple and Magenta) Estimated flux with SOA and FRC with 1D Iron Losses LUT observers respectively.

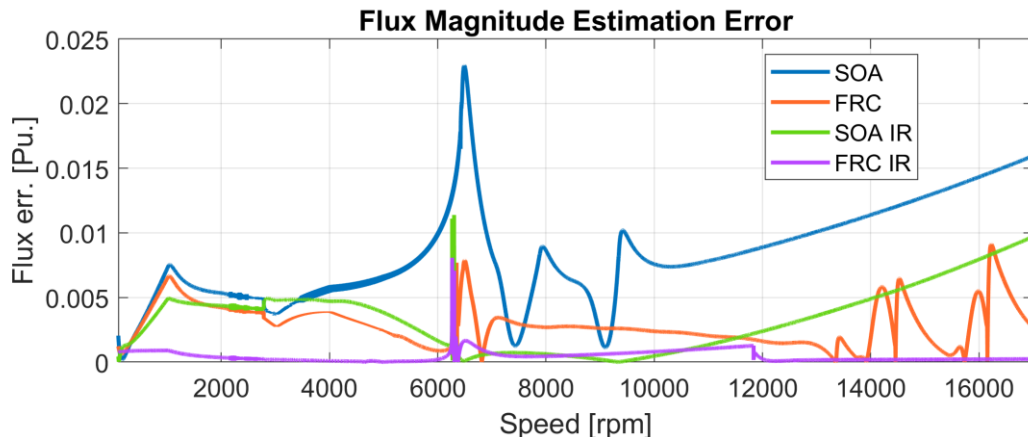


**Figure 86** Absolute Flux Magnitude estimation error. (Blue) flux magnitude estimation error with SOA obs. (Orange) flux magnitude estimation error with FRC obs. (Green) flux magnitude estimation error with SOA obs. with iron loss LUT. (Purple) flux magnitude estimation error with FRC obs. with iron loss LUT.

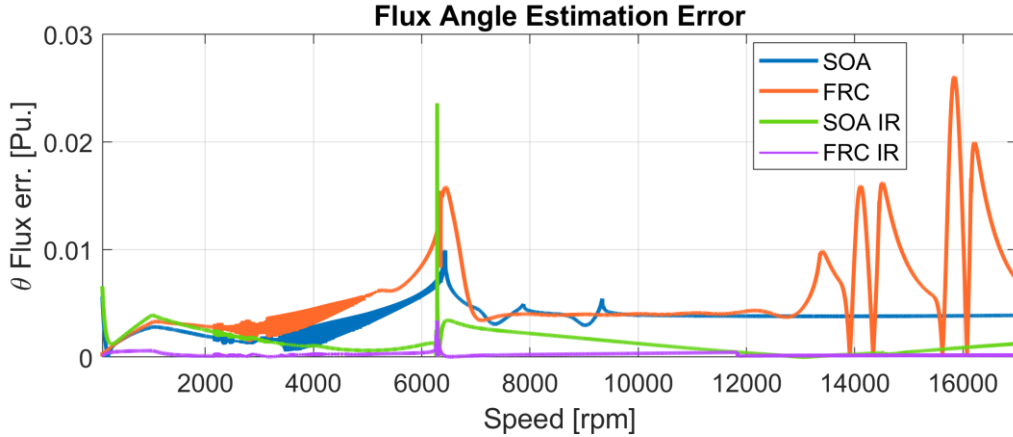


Figure 87 Flux Angle Estimation Error. (Blue) flux angle estimation error with SOA obs. (Orange) flux angle estimation error with FRC obs. (Green) flux angle estimation error with SOA obs. with iron loss LUT. (Purple) flux angle estimation error with FRC obs. with iron loss LUT.

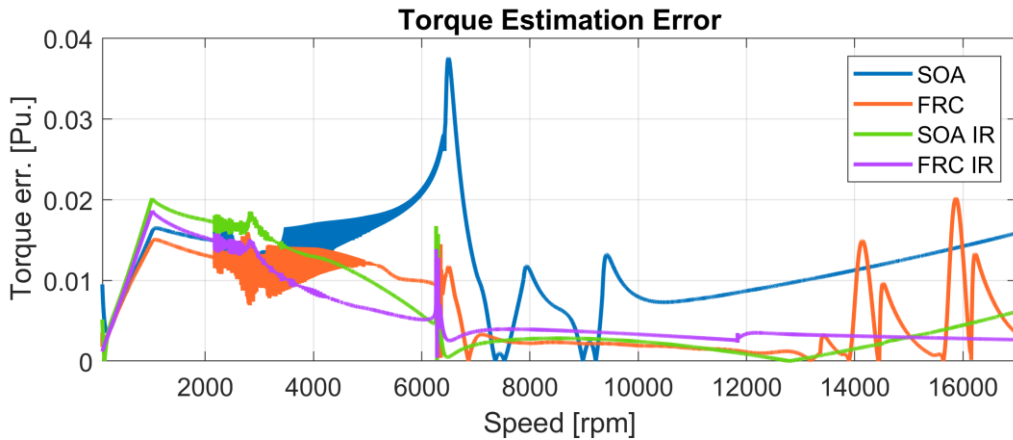


Figure 88 Absolute Torque Estimation Error. (Blue) Torque estimation error with SOA obs. (Orange) Torque estimation error with FRC obs. (Green) Torque estimation error with SOA obs. with iron loss LUT. (Purple) Torque estimation error with FRC obs. with iron loss LUT.

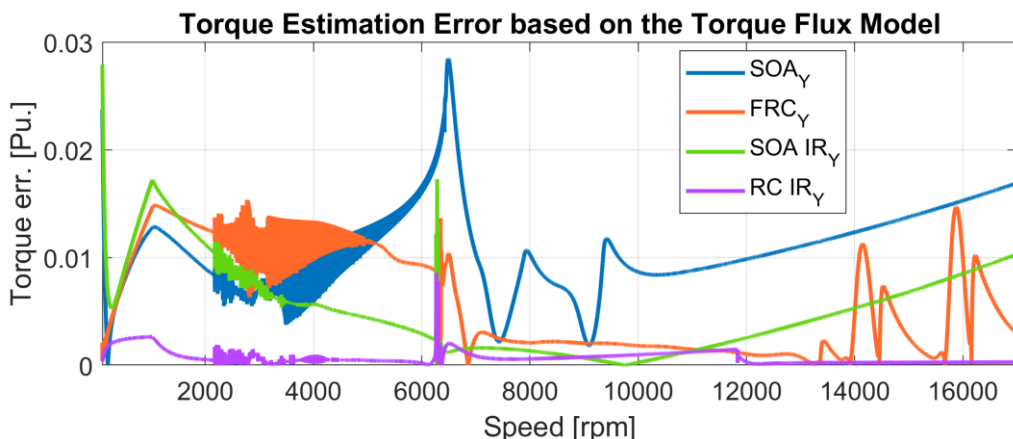


Figure 89 Torque Estimation Error Based on the flux, Shows the abs(Torque-Torque Est.) where the torque estimation is calculated based only on the  $\lambda_d$  and  $\lambda_q$  quantities, without the current. (Blue) Torque estimation error with SOA obs. (Orange) Torque estimation error with FRC obs. (Green) Torque estimation error with SOA Obs. with iron loss LUT. (Purple) Torque estimation error with FRC Obs. with iron loss LUT.

Note that if only the fluxes are considered in order to calculate the torque, the iron losses impact not only the low but the high-speed estimation quality.

## Conclusions

- Both the SOA and FRC observers improve its accuracy at high and low speed with the iron loss model implemented.
- The high-speed inaccuracy of the SOA and FRC observers are caused due to the current observer magnetics model. Since the SOA FO is resilient to parameter variation at high speed.
- The torque estimation for the DB-DTFC control law is also more accurate under with the Iron Loss Magnetics model implementation.
- The limitations of this method are based on the accuracy of the calculated iron loss resistance. A 2D LUT can be implemented in order obtain a more accurate value for the iron loss resistance as a function of the torque.
- If the current observer magnetics model is not updated, the enhancement in the flux observer due to the iron losses model is not notable.

#### 4.4.1 Conclusions:

In this chapter an Iron Loss model for the IPMSM was developed and its influence in the control system were studied,

The Iron Loss models used by the literature were reviewed and from where it is possible to say that:

- A parallel resistance to the Magnetizing branch represents best the steady state losses produced by the iron losses. Where the iron losses model must update the resistance value for the speed and ideally torque range to be most accurate.
- It is not necessary to model the d and q axis resistances as asymmetrical.
- Finite element simulation of the machine results as well as no load losses experimental data can be used to obtain a table of values for the iron losses resistance.

The Iron losses Resistance was obtained.

- The iron loss resistance was calculated with the no-load test. The data is presented in Figure 68. For the no load condition, the iron loss resistance increments with the speed for both machines.
- From the obtained data, a LUT can be implemented in simulation in order to model the machine including iron losses.
- From the FEM data available for the machine, the iron losses resistances were mapped and presented in figure 69. The Machine Iron Loss Measurements are consistent and therefore the iron loss resistance can be properly approximated.
- The contours of the iron loss resistance show a clean iron loss resistance value for each operation point. The results are consistent with the results obtained from experimental data for No Load condition in the previous section.
- From the machine operation data, it is important to notice that: at max speed the current and flux of the machine is not kept constant along the different torque profile.  $I_d$  and  $I_q$  are controlled differently as in the assumed model.
- From the data, a 2-D LUT can be implemented in simulation in order to model the machine including iron losses.

The effects of including such a resistance in the model were modeled. From this model the conclusions show:

- An intrinsic coupling effect exists in the system between the d-axis and q-axis, this coupling is proportional to the flux linkages of both axes, the speed, and depends on the equivalent iron loss resistance for the operation point. The results show an angle deviation proportional to the speed of the drive and an undesired torque production at high speed. These deviations might not be notable in other small drives or drives without field weakening.

- The angle distortion is dependent on the Iron loss resistance, a full model of the iron loss resistance would produce a more accurate result.
- If an iron loss model is considered, the flux control variables are the magnetizing component of the current. The control system has no direct access to it. Therefore, the magnetizing current can only be estimated.
- In a CVC application, the iron loss current will have to be compensated along the speed range in order to perfectly decouple the d and q axis.
- It is important to understand that the iron loss deviate the angle only with the fundamental component of the magnetizing current. As explained by [28] , higher order harmonics coming from the inverter would not be DC quantities in the rotor reference frame and therefore would not produce an angle deviation in the control system.
- A torque asymmetry is present between motoring and generating conditions since the iron losses effect increases the torque in generating condition.
- The iron losses introduce an angle deviation in the voltage. In performance drives automatic angle tuning routines use such a measurement to align the system angle. An error is introduced in the algorithm by the iron losses. The iron loss resistance produces the introduction of an angle in the asymptote of the voltage when the q-axis current is zero.

An iron losses model can be introduced in the current model of the flux linkage observer. This proposal was simulated and the results show that:

- Both the SOA and FRC observers improve its accuracy at high and low speed with the iron loss model implemented.
- The high-speed inaccuracy of the SOA and FRC observers are caused by the torque equation and the current observer's magnetics model. Since the SOA FO is resilient to parameter variation at high speed.
- The torque estimation for the DB-DTFC control law is also more accurate under with the Iron Loss Magnetics model implementation.
- The limitations of this method are based on the accuracy of the calculated iron loss resistance. A 2D LUT can be implemented in order obtain a more accurate value for the iron loss resistance as a function of the torque.
- If the current observer magnetics model is not updated, the enhancement in the flux observer due to the iron losses model is not notable.



# Chapter Five

## 5 Open Loop Tests and Implementation

This chapter presents the results of the open loop tests for the different model corrections discussed in the previous section. The results are displayed and discussed based on the estimated torque, since it is the measurable variable from the test bench.

### 5.1 Observers implementation

First and in order to check the solution, the machine is run under the speed torque profile presented in the following figure:

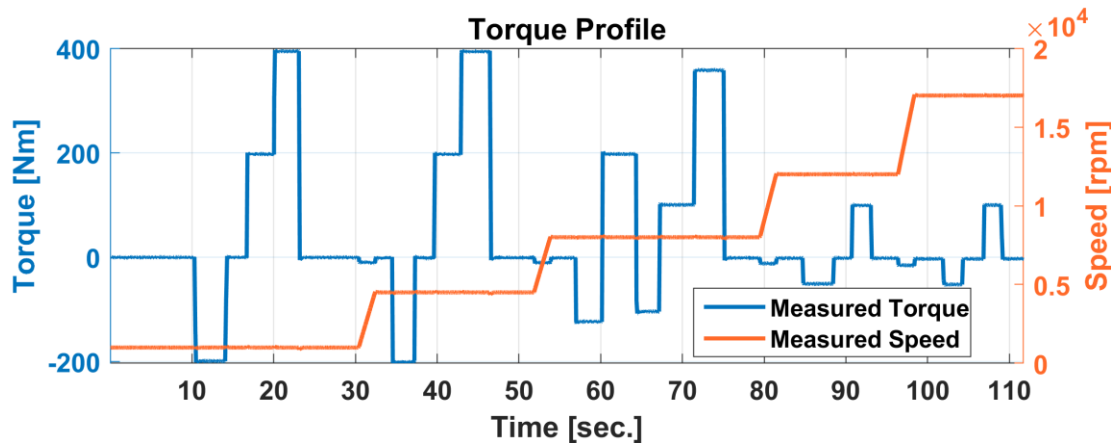


Figure 90 Measured Speed and Torque for Long machine. (Top) Commanded Speed. (Bottom) Commanded Torque.

First the current implementation is checked. This implementation is named the Audi observer, the results are displayed in the next figure and compared with the SOA for benchmarking.

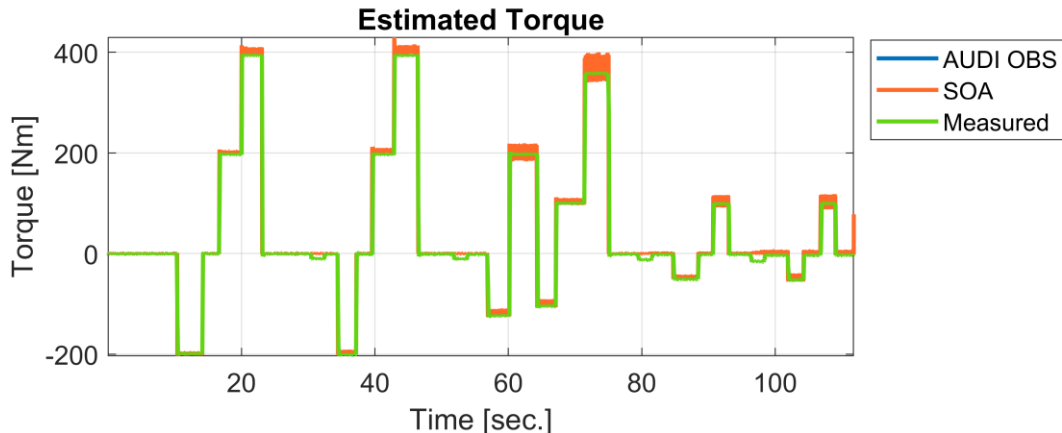
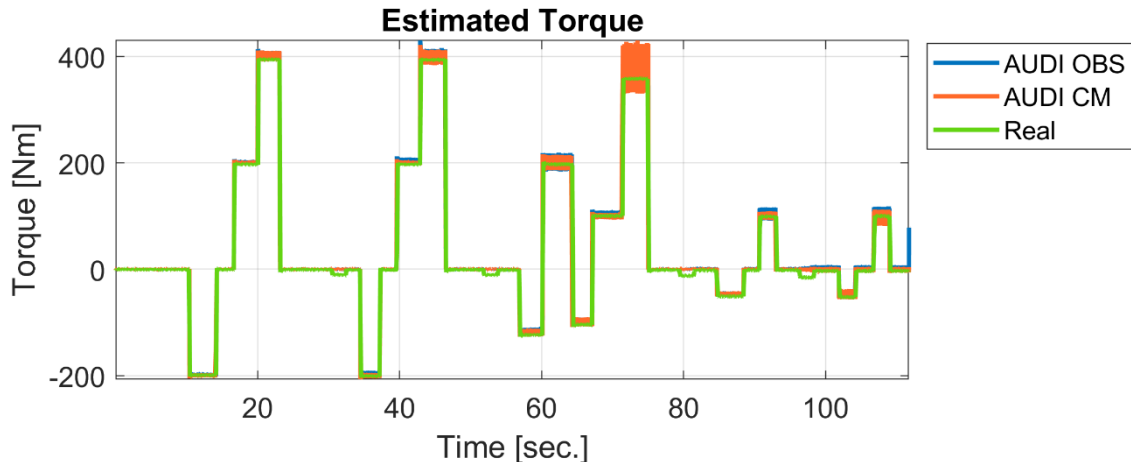


Figure 91 Comparison between SOA and AUDI Observer. (Blue) Estimated torque with the Audi observer. (Dot orange) Estimated torque with the SOA observer. (Green) Measured torque with torque sensor.



**Figure 92 Difference between Gopinath-Obs and CM-Obs.** (Blue) Estimated torque with the Audi observer. (Dot orange) Estimated torque with the Audi observer CM-Obs. (Green) Measured torque with torque sensor.

The differences between the Gopinath-style observer and a CM based Observer are displayed numerically in the following table:

**Table 8 Average differences between CM and VM.** Table values are presented in [%] respect to the Current Model and the angle difference is displayed on the right after the “|” in degrees.

Torque \ Speed	1000 [rpm]	5000 [rpm]	8000 [rpm]	12000 [rpm]	17000 [rpm]
400 [Nm]	-0.66% -0.21°	-1% 0.2°			
357 [Nm]			-3.0% 0.32°		
200 [Nm]	-0.78% -0.16°	-1.7% 0.58°	-1.4% 0.73°		
100 [Nm]			-2.8% 0.66°	-4.4% 0.15°	-7.8% -1.86°
- 50 [Nm]				-2.8% -4.4°	-5% -5.0°
- 100 [Nm]			2.5% -2.4°		
- 200 [Nm]	0.31%  0.38°	2.42% -0.13°			

### Conclusions:

- The implemented Audi observer has SS error and tends to Overshoot the measured torque value.
- The SOA Observer response matches the one of the AUDI controllers
- The Audi controller uses Alpha Beta Voltage Measurements that are compensated for the phase lag produced by the discretization of the plant and have a voltage dead time compensation factor included.

- The CM observer has still problems at high speeds, these problems show asymmetry between motoring and generating conditions. This symmetry in the torque can be caused partially by the iron losses as exposed in the previous section.
- The CM presents more ripple at 8000 rpm.
- The Gopinath-style orbs estimates up to 8% more than the CM at high speeds.
- The angle distortion sign changes at high speeds.
- The magnitude difference between motoring and generating condition at low speeds is asymmetric, while it becomes more symmetric for medium speeds.

After matching the SOA and the Audi observer, the further developed work was implemented and compared. For the improvements proposed on section two:

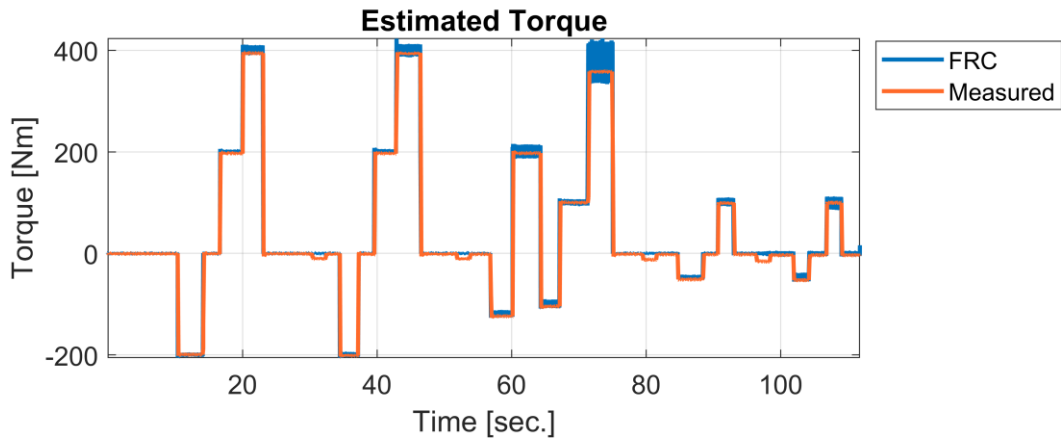


**Figure 93 Open Loop response to the speed/ torque profile from the FRC Observer. (Blue) Estimated torque with the FRC observer. (Orange) Measured torque with torque sensor.**

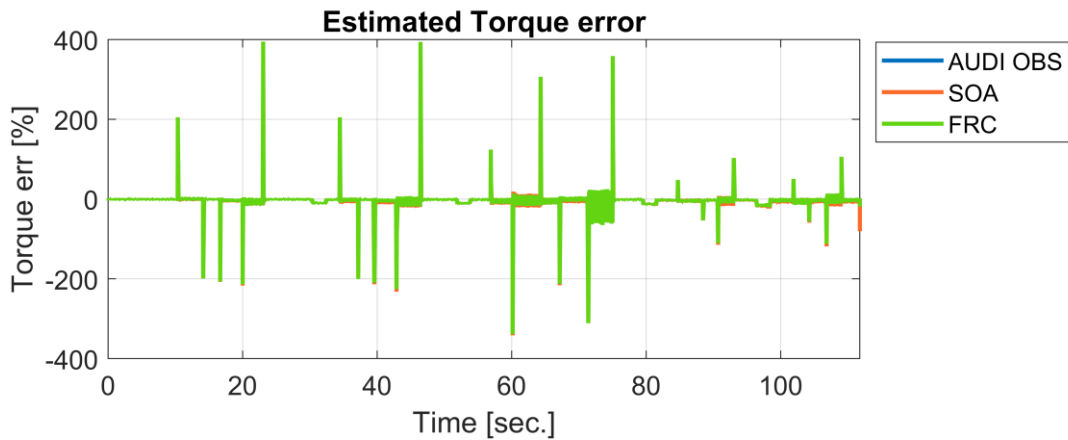


**Figure 94 Torque Error Benchmarking for AUDI, SOA, FRC Observers. (Blue) Estimated torque error with the Audi observer. (Orange) Estimated torque error with the SOA observer. (Green) Estimated torque error with the FRC observer.**

Conclusions:

- The FRC seems to track the commanded torque with the best accuracy.
- All 3 systems show high levels of ripple in SS.
- The FRC presents some transient Overshoot at low speeds.
- Respect to the Ripple, the models were computed with Current Model Observers only, the ripple does not disappear as noticeable in Figure 94. This fact might indicate that the ripple is not coming from the voltage model only.
- The angle shows ripple and distortion, as well as a frequency difference compared with the calculated angle.
- The error figure reveals again that the SOA and AUDI observer have a steady state error and that the deviation increases with speed.

Then the iron loss model presented in section four was included. The results are presented in the following figures:

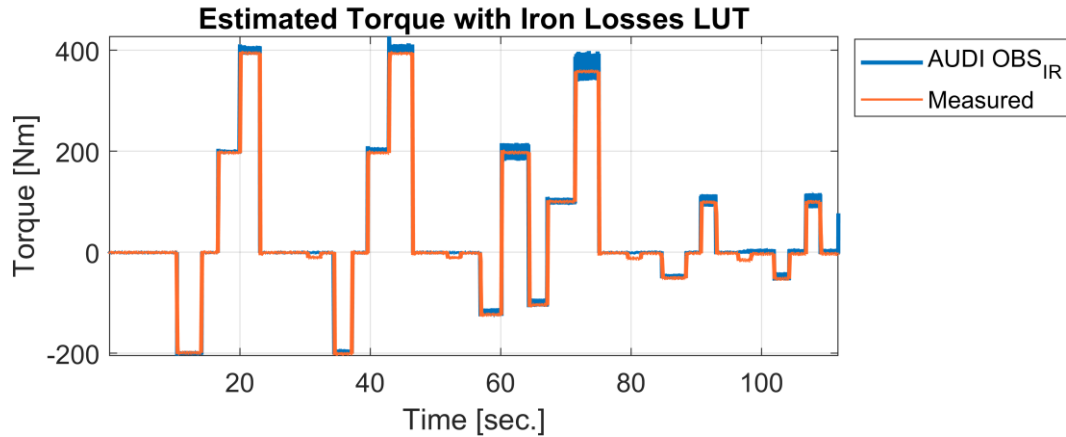


Figure 95 Open Loop response to the speed/ torque profile from the AUDI/SOA Observer with Iron Loss LUT. (Blue) Estimated torque with the Audi observer with Iron losses 1D LUT. (Orange) Measured torque with torque sensor.

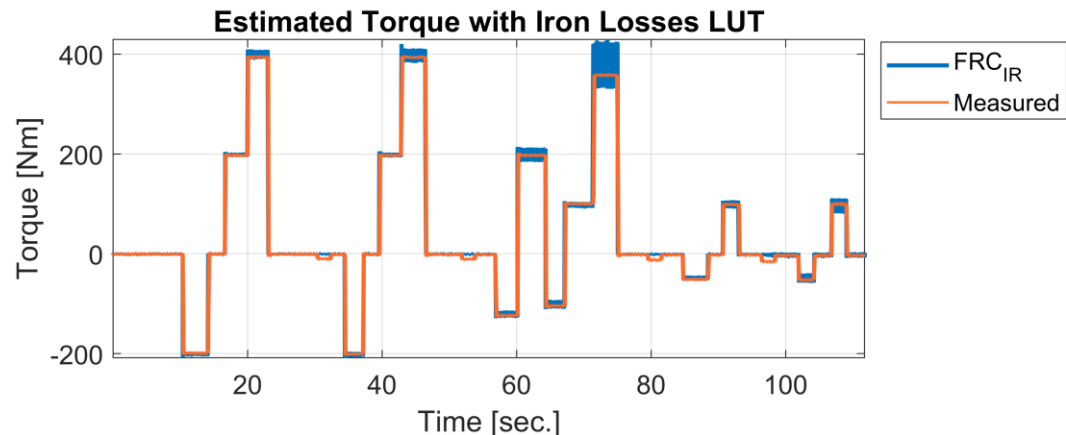


Figure 96 Open Loop response to the speed/ torque profile from the FRC Observer with Iron Loss LUT. (Blue) Estimated torque with the Audi observer with Iron losses 1D LUT. (Orange) Measured torque with torque sensor.

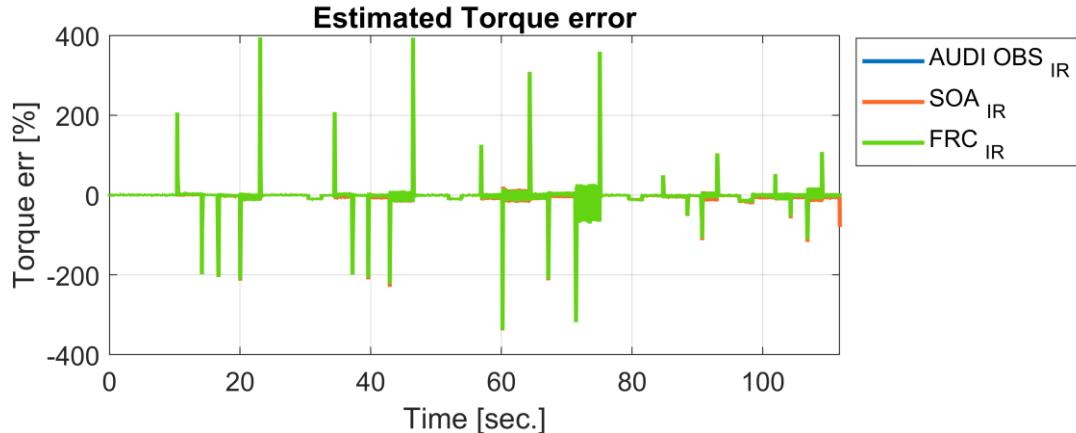


Figure 97 Open Loop Observers benchmarking considering Iron Losses 1D LUT. (Blue) Estimated torque error with the Audi observer. (Orange) Estimated torque error with the SOA observer. (Green) Estimated torque error with the FRC observer.

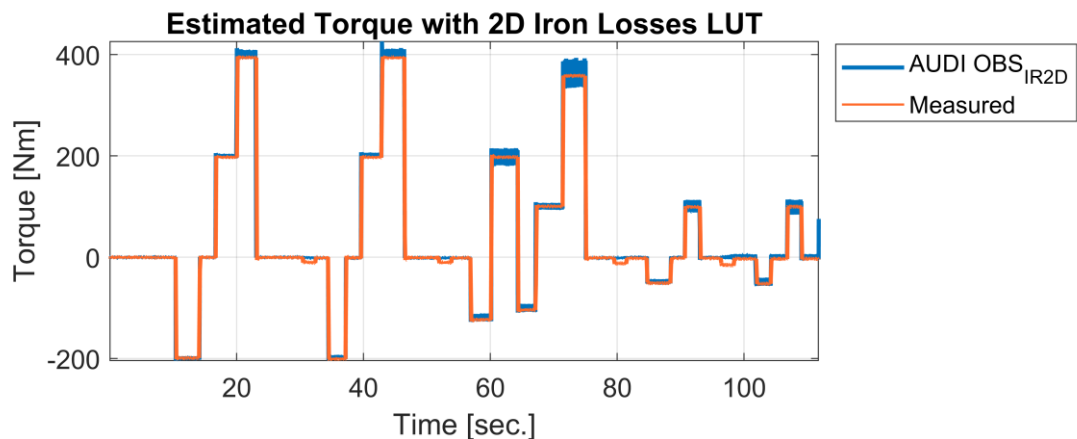


Figure 98 Open Loop response to the speed/ torque profile from the AUDI/ SOA Observer with 2D Iron Loss LUT. (Blue) Estimated torque with the Audi observer with Iron losses 2D LUT. (Orange) Measured torque with torque sensor.

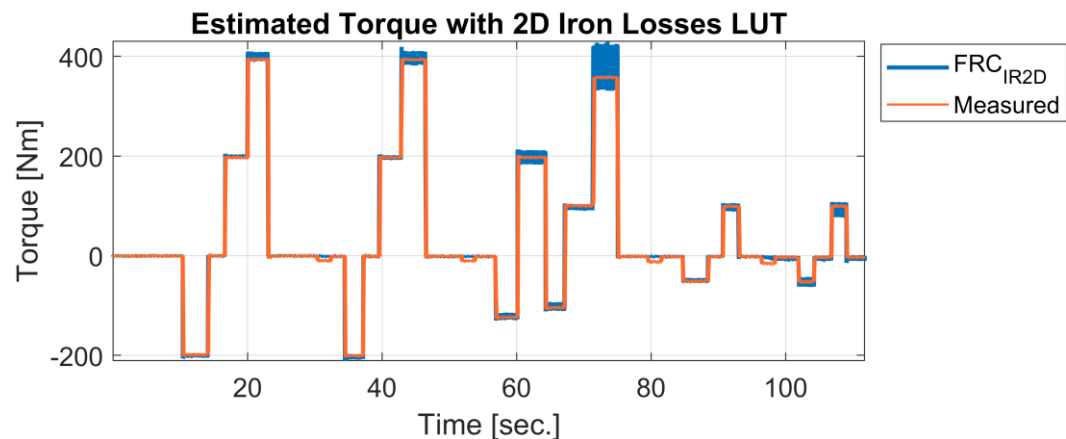


Figure 99 Open Loop response to the speed/ torque profile from the FRC with 2D Iron Loss LUT. (Blue) Estimated torque with the FRC observer with Iron losses 2D LUT. (Orange) Measured torque with torque sensor.

**Table 9** Average torque estimation error with AUDI with 2D LUT and FRC with 2D LUT. Table values are presented in [%] respect to the commanded value. The AUDI observer results are displayed on the left and the FRC results are displayed on the right

Torque \ Speed	1000 [rpm]		5000 [rpm]		8000 [rpm]		12000 [rpm]		17000 [rpm]	
400 [Nm]	-0.4% -0.1%		-1.2% -0.3%							
357 [Nm]					-3.5% -5.4%					
200 [Nm]	-0.5% 0.1%		-1.8% 0.0%		-1.3% 0.1%					
100 [Nm]					-2.6% 0.2%		-3.0% 1.7%		-3.9% 4.3%	
- 50 [Nm]							7.3% 4.0%		7.5% -2.8%	
- 100 [Nm]					1.4% -0.3%					
- 200 [Nm]	0.7% 0.0%		2.7% 0.1%							

**Table 10** Average torque estimation error Considering Iron Losses Model in Torque Equation AUDI with 2D LUT and FRC with 2D LUT. Table values are presented in [%] respect to the commanded value. The AUDI observer results are displayed on the left and the FRC results are displayed on the right.

Torque \ Speed	1000 [rpm]		5000 [rpm]		8000 [rpm]		12000 [rpm]		17000 [rpm]	
400 [Nm]	0.0% 0.4%		-0.5% 0.5%							
357 [Nm]					-1.3% -3.3%					
200 [Nm]	0.2% 0.7%		-0.4% 1.3%		0.0% 1.4%					
100 [Nm]					-0.3% 2.4%		-0.9% 3.6%		-1.3% 6.7%	
- 50 [Nm]							4.0% 0.6%		3.9% -6.4%	
- 100 [Nm]					-0.8% -2.6%					
- 200 [Nm]	0.2% -0.5%		1.3% -1.3%							

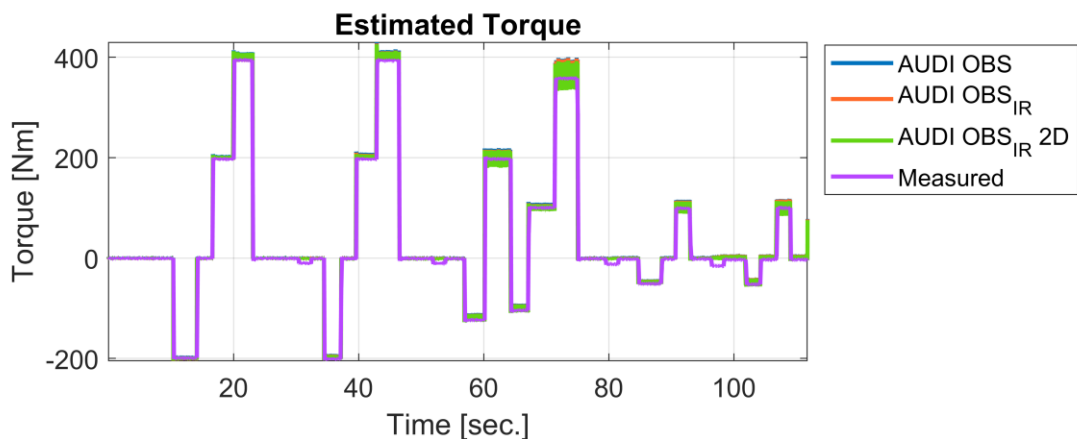


**Figure 100** Open Loop response to the speed/ torque profile from the AUDI/SOA Observer with / Without Iron Loss LUT. (Blue) Estimated torque with original Audi obs. (Orange). Estimated torque with the Audi observer with Iron losses 1D LUT. (Green) Estimated torque with the Audi observer with Iron losses 2D LUT. (Purple) Measured torque with torque sensor.

Models Benchmarking:

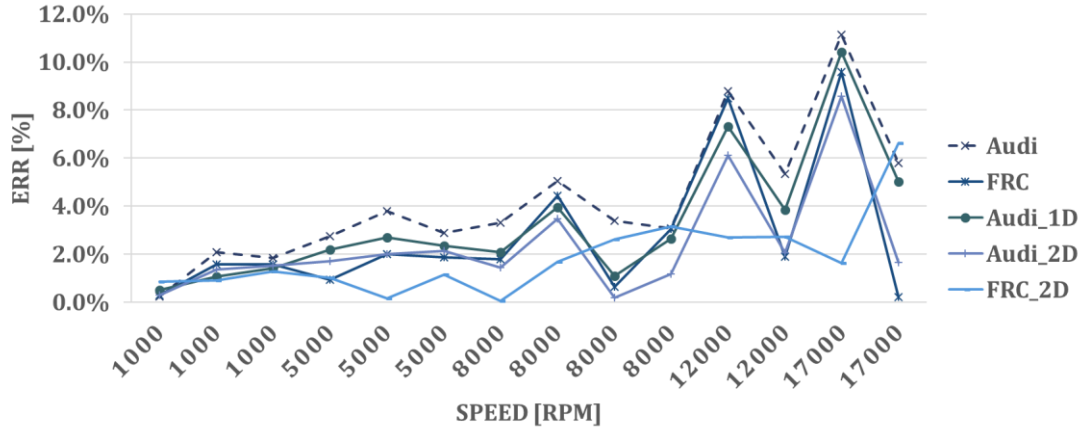


**Figure 101** Average Error Per speed / Torque sector. In this figure the different models are compared respect to the sensed torque for each operation point of the OL test profile. The SOA observer labeled AUDI is shown in dashed lines.

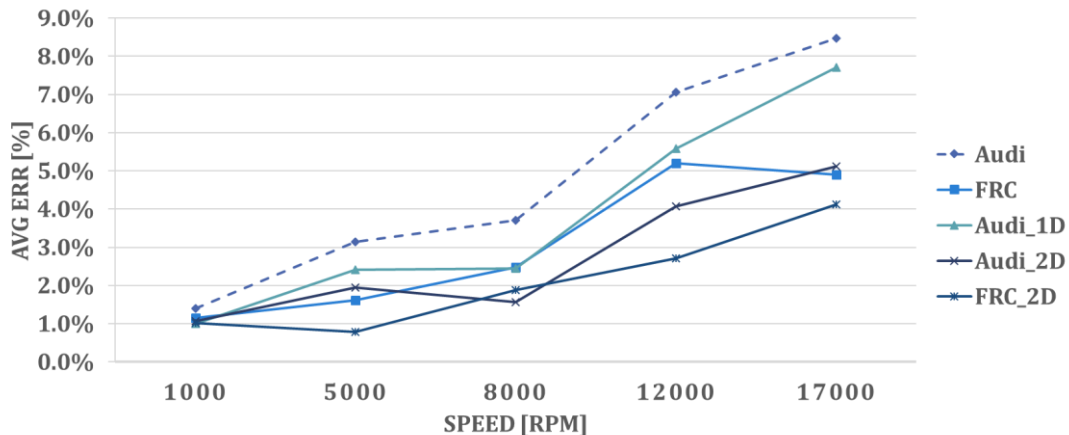


**Figure 102** Average Error Per speed sector. In this figure the different models are compared respect to the sensed torque for each speed operation point of the OL test profile. The SOA observer labeled AUDI is shown in dashed lines.

Conclusions:

- The FRC observer produces a smaller average torque estimation error for most of the quantities when considering the Idqs currents in the torque equation.
- The error is much diminished for both models, making the Audi observer more accurate than the FRC observer, when the magnetizing currents from the iron losses model are substituted in the torque equation.
- If all the values of Table 9 are averaged as absolute values, we can see that the total overall error is of around 2.4% for the Audi observer with 2D LUT and of 1.9% for the FRC observer.
- The error reduction is enhanced with the accuracy of the LUT.
- The 2D LUT implementation reduces the estimation error in the Audi observer in SS.

- The effect of miss considering the iron losses is small, nevertheless the results show a big impact. This is since iron losses affect the system 3 times. (First) in the current model of the flux linkage observer. (Second) in the current model of the Luenberger Current observer. (Third) on the torque estimation equation.
- The FRC observer produces a good Torque estimation accuracy.

## 5.2 Conclusions

- The SOA observer matches the Audi Observer Response in the open loop tests.
- The Gopinath-style orbs estimates up to 8% more than the CM at high speeds.
- Both the SOA and FRC observers improve its accuracy at high and low speed with the iron loss model implemented.
- The FRC with a 2DLUT observer produces a smaller average torque estimation error for most of the quantities when considering the Idqs currents in the torque equation.
- The error is much diminished for both models the, making the Audi 2DLUT observer more accurate than the FRC 2DLUT observer, when the magnetizing currents from the iron losses model are substituted in the torque equation.
- If all the values of Table 10 are averaged as absolute values, we can see that the total overall error is of around 0.2% for the Audi observer with 2D LUT and of 0.4% for the FRC observer.
- The error reduction is enhanced with the accuracy of the LUT.
- The 2D LUT implementation reduces the estimation error in the Audi observer in SS.
- The effect of miss considering the iron losses is small, nevertheless the results show a big impact. This is since iron losses affect the system 3 times. (First) in the current model of the flux linkage observer. (Second) in the current model of the Luenberger Current observer. (Third) on the torque estimation equation.
- The FRC observer produces a good Torque estimation accuracy.

# Chapter Six

## 6 Conclusions and Outlook

This chapter presents the main conclusions reached out of the work and puts the light on the main covered issues and the present work situation. Finally, an outlook is proposed for the future work.

### 4.1. Conclusions

In this work, the literature for the Gopinath-style flux linkage observer was used to identify improvement opportunities for the current flux linkage observer in a DBDTFC drive. The aim was set in the enhancement of the transition between the CM and the VM as well as studding the impact of the Iron Losses on the machine.

First, the Observer Characteristic Method was used to perform a frequency response correction for the IPMSM Flux linkage Observer.

- The implementation is proven possible in the frequency domain if the correct angles are considered.
- The distortion of a FRC observer is smaller in the transition zone as well as in the high speed region.
- At 16 000 RPM the error of the SOA is another order of magnitude bigger than the FRC

The parameter sensitivity test was performed under closed loop simulation conditions and compared with the SOA.

- The FRC corrected observer has a higher dependency on the Current Model and therefore is more parameter sensitive than the SOA. A parameter LUT can solve partially this issue.
- The system dynamics at low speeds show that the magnitude error rejection capability of the FRC is higher than the one of the SOA.
- The angle error is corrected faster in the SOA, but the overshoot is bigger in the FRC.
- The system dynamics at high speeds show that the angle error is smaller in the FRC. The speed dependency of these error is smaller as well.
- The computational effort is larger for the FRC method an open opportunity exists here to enhance this solution.

In the next chapter an Iron Loss model for the IPMSM was developed and its influence in the control system were studied.

- A parallel resistance to the Magnetizing branch represents best the steady state losses produced by the iron losses. Where the iron losses model must update the resistance value for the speed and ideally torque range to be most accurate.

- It is not necessary to model the d and q axis resistances as asymmetrical.
- Finite element simulation of the machine results as well as no load losses experimental data can be used to obtain a table of values for the iron losses resistance.
- The iron loss resistance has been calculated with the no-load test, the iron loss resistance increments with the speed for both machines under this scenario.
- From the obtained data, a LUT can be implemented in simulation in order to model the machine including iron losses.
- From the FEM data available for the machine, the iron losses resistances were mapped and presented. The results are consistent with the results obtained from experimental data for No Load condition in the previous section.
- From the data, a 2-D LUT can be implemented in simulation in order to model the machine including iron losses.

The effects of including such a resistance in the model were modeled, the conclusions show:

- An intrinsic coupling effect exists in the system between the d-axis and q-axis, this coupling is proportional to the flux linkages of both axes, the speed, and depends on the equivalent iron loss resistance for the operation point. The results show an angle deviation proportional to the speed of the drive and an undesired torque production at high speed. These deviations might not be notable in other small drives or drives without field weakening.
- The angle distortion is dependent on the Iron loss resistance and therefore to its accurate calculation.
- If an iron loss model is considered, the flux control variables are the magnetizing component of the current. The control system has no direct access to it. Therefore, the magnetizing current can only be estimated.
- In a CVC application, the iron loss current will have to be compensated along the speed range in order to perfectly decouple the d and q axis.
- It is important to understand that the iron loss deviate the angle only with the fundamental component of the magnetizing current. Higher order harmonics coming from the inverter would not be DC quantities in the rotor reference frame and therefore would not produce an angle deviation in the control system.
- A torque asymmetry is present between motoring and generating conditions since the iron losses effect increases the torque in generating condition. This is a key identification tool to check the necessity of an iron loss compensation in the system.
- The iron losses introduce an angle deviation in the voltage. In performance drives automatic angle tuning routines use such a measurement to align the system angle. An error is introduced in the algorithm by the iron losses. The iron loss resistance produces the introduction of an angle in the asymptote of the voltage when the q-axis current is zero.

An iron losses model can be introduced in the current model of the flux linkage observer. This proposal was simulated, and the results show that:

- Both the SOA and FRC observers improve its accuracy at high and low speed with the iron loss model implemented.
- The high-speed inaccuracy of the SOA and FRC observers are caused by the torque equation and the current observer's magnetics model. Since the SOA FO is resilient to parameter variation at high speed.
- The torque estimation for the DB-DTFC control law is also more accurate under with the Iron Loss Magnetics model implementation.
- The limitations of this method are based on the accuracy of the calculated iron loss resistance. A 2D LUT can be implemented in order obtain a more accurate value for the iron loss resistance as a function of the torque.
- If the current observer magnetics model is not updated, the enhancement in the flux observer due to the iron losses model is less notable.

Finally, the Open Loop tests were carried on for the proposed observers. These tests show that:

- The SOA observer matches the Audi Observer Response in the open loop tests.
- The Gopinath-style orbs estimates up to 8% more than the CM at high speeds.
- Both the SOA and FRC observers improve its accuracy at high and low speed with the iron loss model implemented.
- The FRC with a 2DLUT observer produces a smaller average torque estimation error for most of the quantities when considering the Idqs currents in the torque equation.
- The error is much diminished for both models the, making the Audi 2DLUT observer more accurate than the FRC 2DLUT observer, when the magnetizing currents from the iron losses model are substituted in the torque equation.
- Averaged as absolute values for the errors show that the total overall error is of around 2.4% for the Audi observer with 2D LUT and of 1.9% for the FRC observer.
- The error reduction is dependent on the accuracy of the LUT.
- The 2D LUT implementation reduces the estimation error in the Audi observer in SS.
- The effect of miss considering the iron losses is small, nevertheless the results show a big impact. This is since iron losses affect the system 3 times. (First) in the current model of the flux linkage observer. (Second) in the current model of the Luenberger Current observer. (Third) on the torque estimation equation.
- The FRC observer produces a good Torque estimation accuracy alternative at the cost of an increased parameter sensitivity.

## 4.2.Future Work

Specific to the topic of enhancing the performance of the flux-Observer, many issues show motivations for study and implementation, among these issues are the following:

- The extrapolation of an accurate 2D LUT for the iron losses resistance from a NL Iron losses resistance curve.

- The implementation of the Disturbance Input Decoupling method to be used to eliminate the parameter deviation of the flux linkage observer. This could include a novel iron losses model in the Current Observer.
- Since an Iron Loss Model is available, the torque could be estimated based on the power equation. This new quantity could be used to calculate the flux and therefore a new kind of flux observer could be built.
- Adaptive tuning could be used for the flux observer as proposed by .
- An observer training algorithm could be used. A neural network-based estimation for the machine parameters could be made based on an accurate simulation.
- Optimization could be used to match the flux with the torque, by modifying the parameters used in the flux observer to enhance the tuning and compensating the system for a perfect torque estimation.
- The voltage drop from the semiconductor devices could be included in order to enhance the voltage.

## References

- [1] "J. S. Lee, C. Choi, J. Seok and R. D. Lorenz, "Deadbeat-Direct Torque and Flux Control of Interior Permanent Magnet Synchronous Machines With Discrete Time Stator Current and Stator Flux Linkage Observer," in IEEE Transactions on Industry Applications,," pp. vol. 47, no. 4, pp. 1749-1758, July-Aug. 2011, doi: 10.1109/TIA.2011.2154293..
- [2] "J. S. Lee and R. D. Lorenz, "Robustness Analysis of Deadbeat-Direct Torque and Flux Control for IPMSM Drives," in IEEE Transactions on Industrial Electronics, vol. 63, no. 5, pp. 2775-2784, May 2016.".
- [3] "M. Cao and H. Migita, "A High Efficiency Control of IPMSM with Online Parameter Estimation," 2018 21st International Conference on Electrical Machines and Systems (ICEMS), Jeju, 2018, pp. 1421-1424.".
- [4] "Sul, Seung-Ki. Control of electric machine drive systems. Vol. 88. John Wiley Sons ,2011".
- [5] "Guo, Qingbo, et al. "Maximum efficiency per torque control of permanent-magnet synchronous machines." Applied Sciences 6.12 (2016): 425.".
- [6] F. Briz, "Dynamic Control of AC Machines - Control of PMSM," 2018.
- [7] "Lei, Gang, J. Zhu and Y Guo. Multidisciplinary design optimization methods for electrical machines and drive systems. Heidelberger: Springer, 2016".
- [8] "Lee, Jae Suk, et al. "Deadbeat-direct torque and flux control of interior permanent magnet synchronous machines with discrete time stator current and stator flux linkage observer.",," in *IEEE Transactions on Industry Applications* , (2016): 2775-2784.
- [9] "Y. Wang, H. Flieh, S. Lee and R. D. Lorenz, "Implementation issues and performance evaluation of deadbeat-direct torque and flux control drives," 2015 IEEE International Electric Machines & Drives Conference (IEMDC), Coeur d'Alene, ID, 2015, pp. 953-959.".
- [10] H. E. Khatib, "Flux Observer-Based Deadbeat-Direct Torque and Flux Control for Interior Permanent Magnet Synchronous Machines in Automotive Traction Applications," in *Executed at the Chair of Electrical Drive Systems and Power Electronics, Technische Universität München*, München, 2019.

- [11] W. Xu and R. D. Lorenz, "Reduced Parameter Sensitivity Stator Flux Linkage Observer in Deadbeat-Direct Torque and Flux Control for IPMSMs," in IEEE Transactions on Industry Applications, vol. 50, no. 4, pp. 2626-2636, July-Aug. 2014..
- [12] "A. Yoo and S. Sul, "Design of Flux Observer Robust to Parameter Variation of Interior Permanent Magnet Synchronous Motor," 2008 IEEE Industry Applications Society Annual Meeting, Edmonton, AB, 2008, pp. 1-7.".
- [13] "S. Choi, S. Baek and J. S. Lee, "Torque Error Compensation Algorithm for IPMSM Drives Using a Gopinath Style Stator Flux Linkage Observer," 2019 International Symposium on Electrical and Electronics Engineering (ISEE), Ho Chi Minh, Vietnam, 2019, pp. 314-".
- [14] "M. Hinkkanen, T. Tuovinen, L. Harnefors and J. Luomi, "A Combined Position and Stator-Resistance Observer for Salient PMSM Drives: Design and Stability Analysis," in IEEE Transactions on Power Electronics, vol. 27, no. 2, pp. 601-609, Feb. 2012.".
- [15] "M. Hinkkanen and J. Luomi, "Modified integrator for voltage model flux estimation of induction motors," in IEEE Transactions on Industrial Electronics, vol. 50, no. 4, pp. 818-820, Aug. 2003.".
- [16] "J. Luukko, M. Niemela and J. Pyrhonen, "Estimation of the flux linkage in a direct-torque-controlled drive," in IEEE Transactions on Industrial Electronics, vol. 50, no. 2, pp. 283-287, April 2003.".
- [17] "N. R. N. Idris and A. H. M. Yatim, "An improved stator flux estimation in steady-state operation for direct torque control of induction machines," in IEEE Transactions on Industry Applications, vol. 38, no. 1, pp. 110-116, Jan.-Feb. 2002.".
- [18] "Jang-Hwan Kim, Jong-Woo Choi and Seung-Ki Sul, "Novel rotor-flux observer using observer characteristic function in complex vector space for field-oriented induction motor drives," in IEEE Transactions on Industry Applications, vol. 38, no. 5, pp. 1334-13".
- [19] "H. Kim, S. Sul, H. Yoo and J. Oh, "Distortion-Minimizing Flux Observer for IPMSM Based on Frequency-Adaptive Observers," in IEEE Transactions on Power Electronics, vol. 35, no. 2, pp. 2077-2087, Feb. 2020.".
- [20] "A. E. N. Gaspar, Y. Xu and R. D. Lorenz, "A Simpler Gopinath-Style Flux Observer without a Constant Speed Assumption for Low and High Sampling-to-Fundamental Frequency Ratios for Induction Machines," 2019 IEEE Energy Conversion Congress and Exposition (EC".

- [21] "L. Xu, X. Xu, T. A. Lipo and D. W. Novotny, "Vector control of a synchronous reluctance motor including saturation and iron loss," in IEEE Transactions on Industry Applications, vol. 27, no. 5, pp. 977-985, Sept.-Oct. 1991, doi: 10.1109/28.90356.".
- [22] "J. Richter, A. Dollinger and M. Doppelbauer, "Iron loss and parameter measurement of permanent magnet synchronous machines," 2014 International Conference on Electrical Machines (ICEM), Berlin, 2014, pp. 1635-1641, doi: 10.1109/ICELMACH.2014.6960401.".
- [23] "X. Chen, J. Wang, B. Sen, P. Lazari and T. Sun, "A High-Fidelity and Computationally Efficient Model for Interior Permanent-Magnet Machines Considering the Magnetic Saturation, Spatial Harmonics, and Iron Loss Effect," in IEEE Transactions on Industrial Electronics, vol. 62, no. 7, pp. 4044-4055, July 2015, doi: 10.1109/TIE.2014.2388200..
- [24] "P. Dück and B. Ponick, "A novel iron-loss-model for permanent magnet synchronous machines in traction applications," in 2016 International Conference on Electrical Systems for Aircraft, Railway, Ship Propulsion and Road Vehicles & International Transportation Electrification Conference (ESARS-ITEC), Toulouse, 2016, pp. 1-6, doi: 10.1109/ESARS-ITEC.2016.7841432..
- [25] "S. L. Kellner, M. Seilmeier and B. Piepenbreier, "Impact of iron losses on parameter identification of permanent magnet synchronous machines," 2011 1st International Electric Drives Production Conference, Nuremberg, 2011, pp. 11-16, doi: 10.1109/EDPC.2011".
- [26] "D. M. Ionel, M. Popescu, M. I. McGilp, T. J. E. Miller, S. J. Dellinger and R. J. Heideman, "Computation of Core Losses in Electrical Machines Using Improved Models for Laminated Steel," in IEEE Transactions on Industry Applications, in vol. 43, no. 6, pp. 1554-1564, Nov.-dec. 2007, doi: 10.1109/TIA.2007.908159..
- [27] "E. Levi, "Impact of iron loss on behavior of vector controlled induction machines," in IEEE Transactions on Industry Applications, vol. 31, no. 6, pp. 1287-1296, Nov.-Dec. 1995.".
- [28] "E. Levi, M. Sokola, A. Boglietti and M. Pastorelli, "Iron loss in rotor-flux-oriented induction machines: identification, assessment of detuning, and compensation," in IEEE Transactions on Power Electronics, vol. 11, no. 5, pp. 698-709, Sept. 1996.".
- [29] "B. Gallert, G. Choi, K. Lee, X. Jing and Y. Son, "Maximum efficiency control strategy of PM traction machine drives in GM hybrid and electric vehicles," 2017 IEEE Energy Conversion Congress and Exposition (ECCE), Cincinnati, OH, 2017, pp. 566-571.".

- [30] "L. Xu, X. Xu, T. A. Lipo and D. W. Novotny, "Vector control of a synchronous reluctance motor including saturation and iron loss," in IEEE Transactions on Industry Applications, vol. 27, no. 5, pp. 977-985, Sept.-Oct. 1991.".

# APPENDIX

## Frequency Response Correction Factor Demonstration

For that, the Laplace operators are replaced  $s$  by  $j W$  so that from equation (52) the following expression is obtained:

$$A = \frac{(j w)^2}{(j w)^2 + K_p * (j w) + K_i} \quad (126)$$

Now the idea is to split the imaginary and the real response since the imaginary part corresponds to the phase and the real part to the magnitude.

In order to do so, it is necessary to multiply by the denominators complex conjugate obtaining:

$$A = \frac{(-1) * w^2}{K_i - w^2 + (j w K_p)} * \frac{K_i - w^2 - (j w K_p)}{K_i - w^2 - (j w K_p)} \quad (127)$$

Operating a real term multiplied by a complex number is obtained:

$$A = \frac{(-1) * w^2}{(K_i - w^2)^2 - w^2 K_p^2} * \frac{(K_i - w^2) - (j w K_p)}{1} \quad (128)$$

Through Euler's formula, it is easy to prove that:

$$-1 = \cos(\pi) + j \sin(\pi) = e^{j(\pi)} \quad (129)$$

In order to simplify the system, the complex numbers are expressed in terms of:

$$a = (K_i - w^2) \quad (130)$$

$$b = w K_p \quad (131)$$

By substitution of these terms in the equation, A is expressed in the following form:

$$A = \frac{w^2}{(K_i - w^2)^2 - w^2 K_p^2} * \frac{a - j b}{1} * e^{j\pi} \quad (132)$$

Since  $a - j b$  is a complex number term can be presented as:

$$a - j b = Abs(a - j b) * e^{j\varphi} \quad (133)$$

Where:

$$\varphi = \operatorname{Arg} (a - jb) \quad (134)$$

Since  $K_p$  and  $K_i$  are positive real numbers,  $a > 0$  and therefore, the argument of the complex number becomes:

$$\operatorname{Arg} (a - jb) = \operatorname{atan} \left( \frac{-b}{a} \right) = -\operatorname{atan} \left( \frac{b}{a} \right) \quad (135)$$

Now by substitution A becomes:

$$A = \frac{w^2}{(K_i - w^2)^2 - w^2 K_p^2} * e^{j\pi} * \sqrt{a^2 + b^2} * e^{j - \operatorname{atan} \left( \frac{b}{a} \right)} \quad (136)$$

The numerator of the left term is expressed as a multiplication of two equal quantities so that the following expression is formed:

$$A = \frac{w^2}{\sqrt{(K_i - w^2)^2 - w^2 K_p^2}} * \frac{\sqrt{a^2 + b^2}}{\sqrt{a^2 + b^2}} * e^{j(\pi - \operatorname{atan} \left( \frac{b}{a} \right))} \quad (137)$$

And by simplifying arriving to:

$$A = \frac{w^2}{\sqrt{(K_i - w^2)^2 - w^2 K_p^2}} * e^{j(\pi - \operatorname{atan} \left( \frac{b}{a} \right))} \quad (138)$$

Or subsequently

$$A = \frac{w^2}{\sqrt{(K_i - w^2)^2 - w^2 K_p^2}} * e^{j\alpha} \quad (139)$$

Where:

$$\alpha = \pi - \operatorname{atan} \left( \frac{b}{a} \right) \quad (140)$$